BRNO UNIVERSITY OF TECHNOLOGY

FACULTY OF ELECTRICAL ENGINEERING AND COMMUNICATION

DEPARTMENT OF RADIO ELECTRONICS

3D PRINTED MICROWAVE STRUCTURES

3D TIŠTĚNÉ MIKROVLNNÉ STRUKTURY

DOCTORAL THESIS
DIZERTAČNÍ PRÁCE

AUTHOR   Ing. Jaroslav Zechmeister
AUTOR PRÁCE

SUPERVISOR   doc. Ing. Jaroslav Láčík, Ph.D.
ŠKOLITEL

BRNO 2025

Abstract

This dissertation focuses on the development of methods for the design and optimization of pixelated microwave structures. A novel optimization algorithm, Binary Ink Stamp Optimization (BISO), was proposed and demonstrated strong performance on benchmark problems as well as in practical antenna and filter designs. A design strategy for SIW horn antennas employing pixelated dielectric loads was introduced and validated through the design of three antennas. An automated procedure for waveguide filter design based on pixelation was developed and applied to two X-band filters. All prototypes were fabricated using 3D printing. The TR method was used to characterize the electromagnetic properties of the 3D-printed materials used for the design of the aforementioned structures.

Keywords

pixelated microwave structures, SIW horn antennas, waveguide filters, evolutionary algorithms, binary optimization, 3D printing

Abstrakt

Tato disertační práce se zaměřuje na vývoj metod pro návrh a optimalizaci pixelových mikrovlnných struktur. Byl navržen nový optimalizační algoritmus nazvaný Binary Ink Stamp Optimization (BISO), který prokázal své vlastnosti jak na testovacích úlohách, tak i v praktických návrzích antén a filtrů. Byla představena návrhová procedura pro SIW trychtýřové antény využívající pixelové dielektrické zátěže a ověřena na návrhu tří antén. Byla představena automatizovaná procedura pro návrh vlnovodových filtrů založených na pixelaci, která byl aplikována na návrh dvou filtrů pro pásmo X. Všechny prototypy byly vyrobeny pomocí 3D tisku. Pro charakterizaci elektromagnetických vlastností 3D tištěných materiálů použitých pro návrh výše zmíněných struktur byla využita TR metoda.

Klíčová slova

pixelové mikrovlnné struktury, SIW trychtýřové antény, vlnovodné filtry, evoluční algoritmy, binární optimalizace, 3D tisk

Declaration

I declare that I have written my doctoral thesis on the theme of "3D Printed Microwave Structures" independently, under the guidance of the doctoral thesis supervisor and using the technical literature and other sources of information which are all quoted in the thesis and detailed in the list of literature at the end of the thesis.

As the author of the doctoral thesis I furthermore declare that, as regards the creation of this doctoral thesis, I have not infringed any copyright. In particular, I have not unlawfully encroached on anyone's personal and/or ownership rights and I am fully aware of the consequences in the case of breaking Regulation §11 and the following of the Copyright Act No 121/2000 Sb., and of the rights related to intellectual property right and changes in some Acts (Intellectual Property Act) and formulated in later regulations, inclusive of the possible consequences resulting from the provisions of Criminal Act No 40/2009 Sb., Section 2, Head VI, Part 4.

Brno, ...
                                                                                      Author's signature

Acknowledgements

Contents

Introduction

The field of 3D printing technology is currently experiencing significant growth. Previously, 3D printing found applications mainly in the industrial and academic sectors, primarily due to the cost of acquiring 3D printers. The advantage of 3D printing is undoubtedly the ability to manufacture almost any computer-generated model. In the development teams of technology companies, 3D printing is primarily used in the prototyping process, significantly shortening it.

3D printing finds applications across a spectrum of industrial and scientific sectors, including aerospace, automotive, healthcare, and even the fashion industry. Its applications lie mainly in the aforementioned development process, as well as in simplifying the production of complex-shaped components.

As the development of 3D printing itself progresses, the variety of usable materials also increases. The most widespread is printing with thermoplastics, such as Acrylonitrile Butadiene Styrene (ABS) or Polylactic Acid (PLA), but metals, ceramics, sand, and glass can also be used for printing. Different printing processes are naturally used for various materials. For example, for printing with thermoplastics, the Fused Deposition Modeling (FDM) technology is employed, which involves layering melted plastic pushed through a nozzle. Other technologies use processes such as heat sintering, ultraviolet radiation curing, chemical catalyzed curing, electron beams, or adhesive.

The principle of 3D printing implies that, unlike traditional manufacturing processes such as machining, it is an additive process. Material is layered using one of the mentioned approaches to achieve the desired structure. The most widespread 3D printing technology is undoubtedly the aforementioned FDM. A relatively broad range of thermoplastics can be used for printing. Printing materials are available in the form of a string wound on a spool. This string is fed into a heated nozzle, where the material is melted and extruded at positions specified by the print program. In this way, individual layers are printed, from which the entire model is subsequently formed. Stereolithography (SLA) serves for high-resolution product printing. In this technology, the curing of a photopolymer resin using ultraviolet radiation is employed for printing. The printing material is in liquid form.

In recent years, 3D printing has also found its application in the field of microwave technologies leading to a significant increase in publications focusing on 3D-printed microwave structures. These publications explore various aspects of 3D printing and its impact on the parameters of printed microwave structures. This includes deviations in material permittivity when using different printing profiles, changes in the electromagnetic properties of 3D-printed material over time, printing resolution, surface roughness of 3D-printed structures, and more. Due to the vari-

ations in electromagnetic parameters of materials from different manufacturers and even among different colors of the same material from one manufacturer, it is necessary to perform a custom characterization of the electromagnetic properties of 3D-printed materials. The establishment of suitable measurement methods is particularly challenging for composite 3D-printed materials. It has become standard to utilize 3D printing to manufacture prototypes of published microwave structures to expedite the production process. With advancements in 3D printing technologies, its utilization in higher frequency bands is becoming feasible. For example, 3D-printed microwave structures operating in the submillimeter wave band have been published. Currently, there are also available 3D printing technologies combining multiple materials, including combinations of dielectric and metallic materials. This allows for the printing of complete structures, such as antennas with PCB boards, at once. These aforementioned facts suggest that 3D printing in the field of microwave structures is firmly established, and its future utilization is poised for growth due to the opportunities it offers compared to conventional manufacturing methods.

As mentioned earlier, 3D printing enables the production of unconventional structures, making it practically possible to print any 3D object created using computer-aided design. For the design of unconventional structures, unconventional methods must also be sought. Pixelization is one of these methods. In principle, it involves dividing the area dedicated to the final structure into small elements (pixels) and adjusting the properties of these elements to achieve the desired characteristics of such a structure. The simplest case is binary pixelization, where pixels can be in one of two states. For example, it may involve the presence of material where a pixel is either filled with material or not. A further stage is multi-state pixelization, where there are multiple discrete states. An example could be a perforated structure where each pixel is described by an area with a hole whose diameter can have one of several predefined values. The final stage is continuous pixelization, where pixels can take on a value within a predefined continuous interval. However, this method of pixelization is the most demanding in terms of design and physical realization of such a structure. Generally, the biggest challenge for an effective method of designing pixelated structures is the number of possible combinations of pixels. Describing an area with a larger number of pixels increases the number of possible realizations exponentially, and these possibilities need to be explored, which can be computationally intensive. With the rapid growth in performance of common PCs or workstations, the design of such structures becomes feasible.

1 State of the Art

This chapter reviews the state of the art in the four main fields addressed in this thesis: the use of pixelated structures in microwave applications, Substrate Integrated Waveguide (SIW) antennas, waveguide filter design, and 3D-printed material characterization. For 3D-printed microwave structures, unconventional solutions such as pixelization offer new possibilities, and the first part of this chapter discusses the application of pixelated structures in microwave technology as well as methods for their optimization. SIW horn antennas are valued for their ease of manufacturing and integration with planar circuits, though they typically suffer from high side and back lobes and unequal radiation patterns in principal planes; therefore, recent methods to improve these parameters are reviewed, along with state-of-the-art 3D-printed structures based on SIW technology. In the field of microwave waveguide filters, automation and machine learning approaches are becoming increasingly important for design efficiency, and recent advancements in these areas are explored, with an emphasis on how flexible manufacturing approaches such as 3D printing support unconventional designs. For both fields, pixelization may lead to unconventional solutions that could address the aforementioned limitations. Finally, for effective microwave structure design, knowing the electromagnetic parameters is crucial, so state-of-the-art methods for characterizing 3D-printed materials and their properties are summarized.

1.1 Pixelated Microwave Structures

A pixelated structure can be thought of as one that is created by dividing the space dedicated to the implementation of the structure into elements (which may or may not be the same size) whose properties are independently controlled to achieve the desired response. The simplest case is binary pixel structures where pixels can be in two states. An example of a binary pixelated structure in the field of microwave applications is a planar Printed Circuit Board (PCB) structure where the elements may be in two states—either with or without copper (as shown in Fig. 1.1). When each element is described by more than one bit, the structure becomes multi-state. An example of a microwave multi-state pixelated structure is the pixelated dielectric resonator antenna presented in [3], shown in Fig. 1.2. Each pixel may have a height in the range of 2 mm to 30 mm.

For example, in microwave antenna design, pixel structures have demonstrated their versatility primarily in planar form. Works published in [4]–[6] showcase the use of pixel structures in designing multiband and narrowband monopole planar antennas. The proposed antennas exhibit high Bandwidth (BW) at dimensions

comparable to conventionally designed antennas and maintain good gain stability over the entire operating BW. Another application of planar pixel structures is illustrated in [7] where they are utilized for antenna miniaturization. The proposed loop antenna, operating at 900 MHz, showed a remarkable 60% reduction in dimensions. In [1], a planar pixelated structure is employed to reduce the mutual coupling between two microstrip antennas. After applying the resonant structure, mutual coupling between the antennas was significantly reduced. This serves as an example of the significant advantages of pixelization approaches where properties can be improved without adding any components or increasing dimensions, solely by applying pixelation to the space between the antennas. The work presented in [8] focuses on a pixelated planar antenna tailored for Internet of Things (IoT) applications. Instead of the common square geometry, cross-shaped pixels are used, providing advantages due to potential singularities at the cell corners. A microwave waveguide filter based on pixelated planar inserts is presented in [9]. The optimization process involves selectively turning pixels on (copper) and off (no copper) on the dielectric
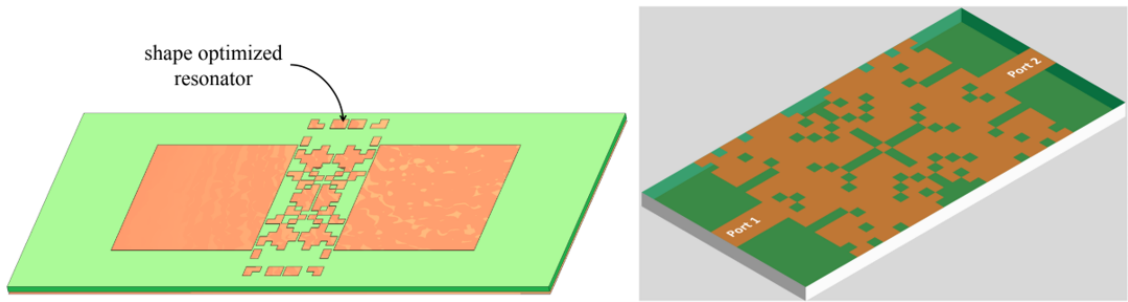

Fig. 1.1: Example of binary pixelated microwave structures in planar form. Adopted from [1] and [2].
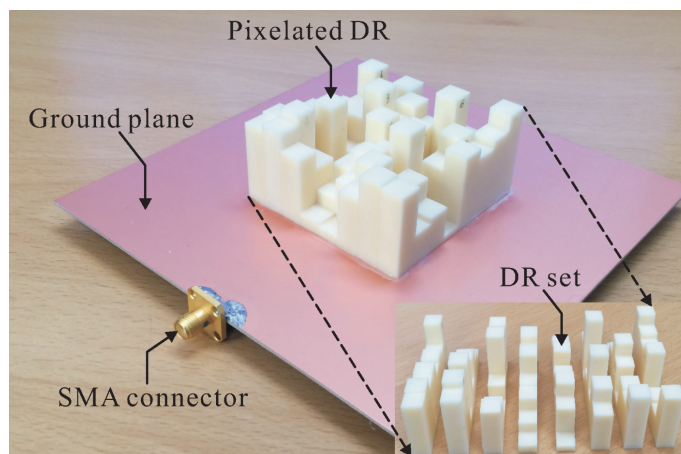

Fig. 1.2: Wideband circularly polarized dielectric resonator antenna composed of 8x8 dielectric square bars. Adopted from [3].

sheet resulting in three identical pixelated structures that provide the desired filter response. In the field of sensing applications, [10] presents a pixelated angular displacement sensor. This sensor is realized as a planar complementary split-ring resonator with an inner pixelated structure achieving a significant enhancement of the sensor sensitivity.

Pixelated structures in non-planar forms were employed in [3] and [11]. The work in [3] introduces a wideband circularly polarized pixelated Dielectric Resonator Antenna (DRA), composed of 8x8 dielectric square bars (Fig. 1.2). The lengths of these bars are optimized to achieve desired performance characteristics. A similar strategy is applied in [11] for designing a linearly polarized DRA where the pixelated structure is organized in a 13x13 grid. Both studies emphasize that the pixelated structure enhances antenna performance, such as BW or gain while maintaining the dimensions of conventional DRAs.

Many state-of-the-art works deal with optimization procedures for these structures. The optimization of pixel structures involves a key aspect. A flowchart of a typical optimization process for pixelated microwave structures is shown in Fig. 1.3. In [12]–[14], the impact of individual components in the global optimization process on the design of pixel antennas is thoroughly examined. The examined components were the chosen optimization method, the selected criterion function, and the parameters set for the Genetic Algorithm (GA). For the design of a phase-gradient metasurface lens in [15], the GA is employed to optimize pixelated unit cells as well. The lens matrix comprises seven cells each optimized for different transmission phases. The work in [16] introduces the utilization of a Multi-Objective Binary Particle Swarm Optimization (MOBPSO) algorithm, a modification of Binary Particle Swarm Optimization (BPSO) based on Pareto dominance. This algorithm is employed to optimize a dual-band planar antenna, and the authors emphasize its ability to deliver satisfactory antenna performance with weak dependency on the initial antenna geometry. In [2], a pixelated RF planar filter is presented. In this study, a search algorithm named Direct Binary Search (DBS) was utilized for the optimization of the pixelated structure. The principle of this algorithm involves flipping a predefined number of pixels. After each flip, the pixelated structure undergoes evaluation by the fitness function. If improvement is detected, the flipped pixels are retained; conversely, if the fitness function worsens, the change is discarded.

In the realm of pixelated structure design, the integration of Artificial Intelligence (AI) has also been explored. In [17], a planar pixelated dual-band antenna is designed using Convolutional Neural Network (CNN) regression. It is noteworthy that the training data for the CNN is based on a pixelated design derived from another article with limited allowable changes, specifically in the filling of empty pixels. The total number of geometries included in the training dataset was 5016.

In [18], a CNN is employed for designing a pixelated matching network for a power amplifier. The authors mention that the CNN was trained on approximately 70,000 randomly generated geometries, a process that can be time-consuming especially when a full-wave simulation is needed for geometry evaluation.

Recent work shows that pixelation can enhance the performance of microwave structures. Pixelization is versatile and can be applied in various forms, from planar to 3D structures. It often results in an unexpected shape, especially for structures in limited or unexplored environments. Recent studies have demonstrated that satisfactory designs can be achieved with low dependence on the initial structure, allowing for the design of these structures without predefined templates. When combined with 3D printing, this approach offers tremendous design variability. The main goal of pixelization is to find a structure with the desired performance. As the
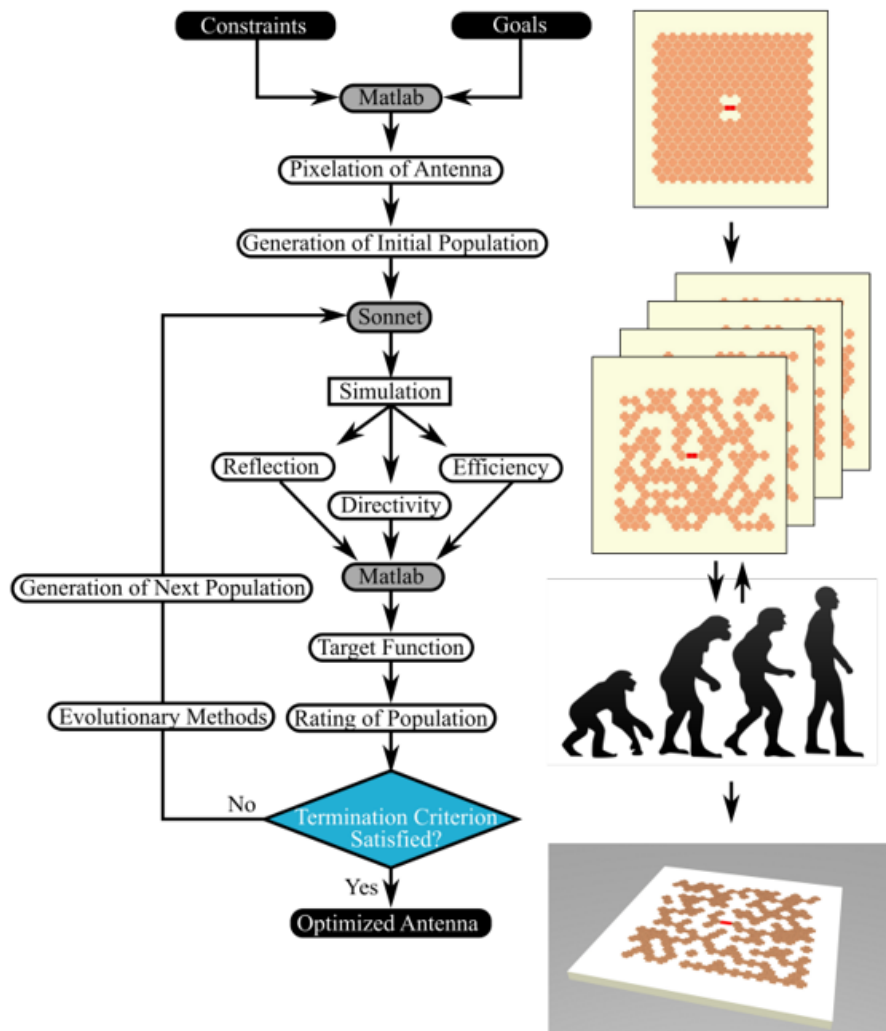

Fig. 1.3: Typical flowchart of an evolutionary optimization process of pixelated structures. Adopted from [8].

number of pixels increases, the number of possible structures grows exponentially, necessitating an efficient optimization process. The most widely used algorithm in this field is the GA which employs selection, crossover, and mutation procedures during the optimization process. While this algorithm treats all bits with equal importance, this can be inefficient for real pixel structures where some bits may significantly affect the structure's response more than others. Therefore, it would be advantageous to develop an optimization process that considers the importance of each bit during optimization. The mentioned DBS algorithm may be inefficient for pixelated structures with a large number of pixels. This process is similar to the Greedy algorithm which is effective at finding the global minimum, but requires a large number of fitness function evaluations. This can be very time-consuming, especially when full-wave simulation is necessary to evaluate the structure, making its suitability for pixelization questionable. On the other hand, approaches using CNN promise a fast optimization process, but the network needs to be trained, which also requires a large number of evaluated combinations. For optimization, some binary heuristic algorithms seem most appropriate.

1.2 Substrate Integrated Waveguide Horn Antennas

Substrate Integrated Waveguide SIW technology is an advanced technique that combines the benefits of rectangular waveguides and planar transmission line structures. SIW structures are created by embedding metallic via holes in a dielectric substrate to form a waveguide. These via holes connect the top and bottom metallic layers, effectively guiding the electromagnetic waves through the substrate in a manner similar to conventional waveguides but within a planar form factor, as shown in Fig. 1.4. This integration allows for the compact and low-cost realization of high-frequency
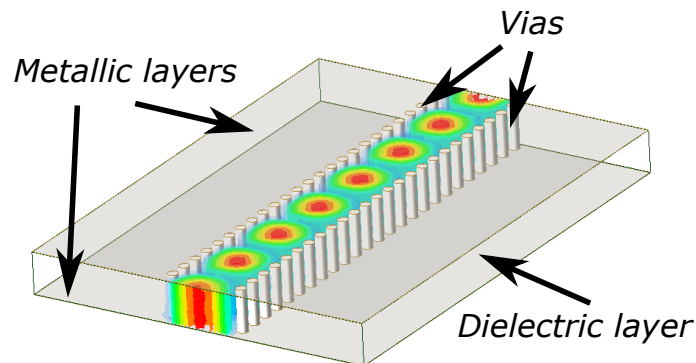

Fig. 1.4: Demonstration of Substrate Integrated Waveguide and its electric field distribution.

components and systems. SIW technology offers several advantages including ease of integration with other planar circuits and the potential for high performance with reduced size and weight. Moreover, SIW structures exhibit low loss and good shielding properties which are crucial for high-frequency applications.

Horn antennas are widely used in wireless applications due to their simple structure, high gain, efficiency, and wide BW. However, conventional waveguide-based horn antennas suffer from large volume, heavy weight, and high fabrication costs. Promising alternatives are SIW horn antennas. They are electrically similar to conventional horn antennas based on rectangular waveguides, easily integrable with planar circuits, and can be fabricated using a low-cost printed circuit board process. Unfortunately, SIW horn antennas have a narrow BW, high levels of side and back radiation lobes, and primarily unequal radiation patterns in the E- and H-planes (Fig. 1.5).

To enhance the performance of SIW horn antennas, various techniques can be exploited. Higher gain and narrower beamwidth can be achieved by adding a dielectric load in front of the antenna aperture [19]. By adjusting the shape of the dielectric load or perforating it [20] (Fig. 1.6), a higher gain can be achieved. Printed metal periodic transitions on top and bottom of the load are also a feasible approach to gain enhancement of SIW horn antennas [21]. Periodic transitions for antenna performance enhancement are also used in [22] (Fig. 1.7). In [23], a combination of microstrip transitions in front of the antenna aperture and metalized blind via holes provide enhancements of antenna gain while reducing its longitudinal dimension. Although all these approaches improve the radiation properties of SIW horn antennas, such structures still provide unequal beamwidths in E- and H-planes. SIW horn antennas with equal beamwidths in E- and H-planes were presented in [24] and [25]. Unfortunately, these structures are multi-layered devaluing the main benefits of one-layer SIW horn antennas, such as easy manufacturing and a low profile (Fig. 1.8).
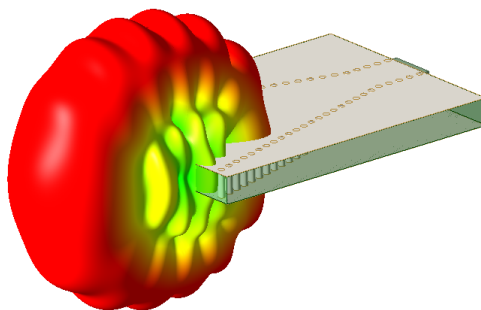

Fig. 1.5: Typical radiation pattern of SIW horn antenna.

Several works employ 3D printing for the manufacturing of structures based on SIW. In [26], SIW components manufactured using 3D printing technology are demonstrated for the first time. The letter presents a SIW cavity resonator and interconnect with four E-plane bends, both manufactured using 3D printing technology. In [27], 3D-printed SIW filters with different infill factors are presented. By changing the infill factor, the effective dielectric constant of the material may be modified, even locally. In [28], the minimization of the insertion loss of the 3D-printed SIW is investigated by using a non-uniform honeycomb-shaped substrate. A microwave microfluidic sensor based on a SIW cavity manufactured using 3D printing technology is presented in [29]. Another 3D-printed microfluidic sensor based on a SIW structure with a cavity is presented in [30]. The uniqueness of this work lies in using a novel 3D print process that enables dielectric and conductive materials to be printed simultaneously. In [31], a 3D-printed SIW horn antenna with applied hard and soft walls to improve its directivity and front-to-back ratio is presented.
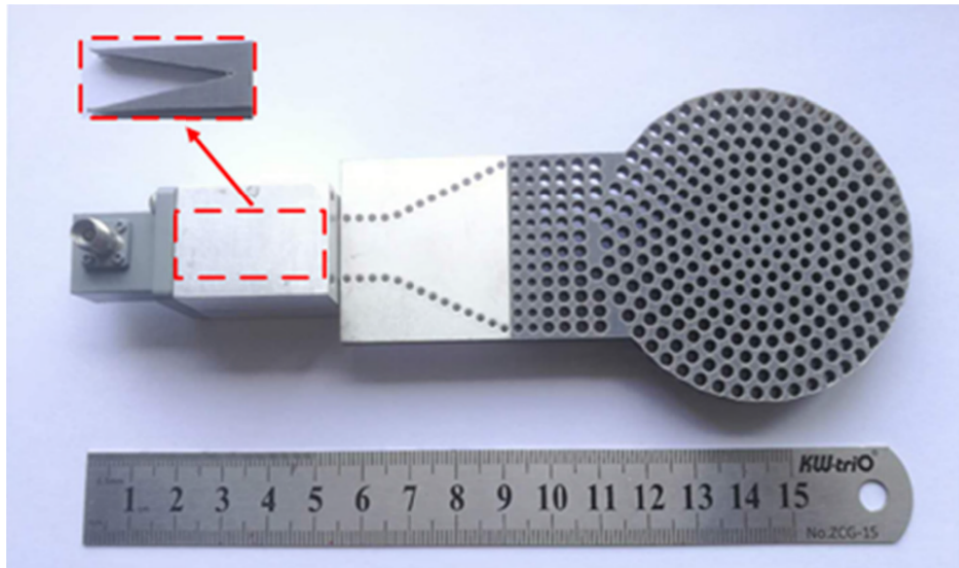

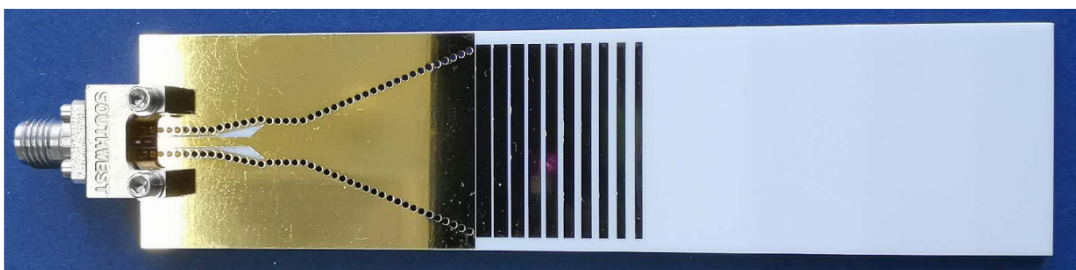Fig. 1.6: SIW horn antenna with perforated dielectric load. Adopted from [20]

Fig. 1.7: SIW horn antenna loaded with tapered multistrip transition and dielectric slab. Adopted from [22].
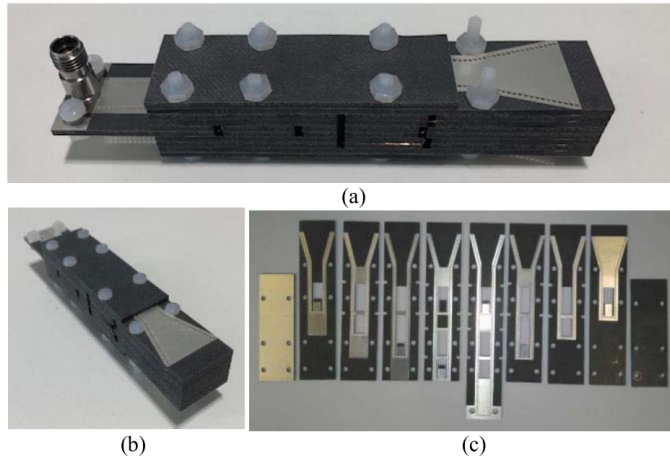
Fig. 1.8: Photographs of the fabricated and assembled SIW horn antenna with equal beamwidths in E- and H-planes. (a) Side view. (b) Perspective view. (c) Each element before assemblage. Adopted from [24].

The authors mention that this antenna design is unable to be manufactured by conventional machining methods. The authors used FDM 3D printing technology, and the antenna was manufactured using very commonly used material PLA.

SIW horn antennas are a promising technology for future communication systems since they can serve as directional antennas in planar form. Their performance may be enhanced by using a proper dielectric load in front of the antenna aperture. This leads us to the possible exploitation of 3D printing for these loads since the technology can manufacture very complex dielectric structures. In the realm of 3D-printed SIW horn antennas, investigations seem to be at the beginning, leaving much space to explore the possibilities. Moreover, the 3D printing industry is still advancing, and new technologies will open new possibilities. For example, today we are already encountering technologies that can produce entire PCBs using 3D printing [32] (Fig. 1.9), enabling the manufacture of PCBs integrated with SIW horn antennas at once.

1.3 Microwave Waveguide Filters

Microwave filters are crucial for modern communication devices controlling the frequency response of the system by providing transmission in the passband and attenuation in the stopband [33]. One class of microwave filters is waveguide filters. The conventional design process consists of several steps [34]: choosing a suitable approximation for the filter specifications, synthesizing an equivalent circuit model, finding its physical realization in the waveguide, and optimizing the filter to meet desired

responses. All these steps require specific experience from the designer (Fig. 1.10).

In recent years, there has been a significant increase in papers dealing with artificial intelligence approaches for microwave filter design [34], aiming for some level of automation. In [35], the design procedure directly optimizes the shape of the waveguide filter using the shape deformation technique. In Fig. 1.11, the optimization error per iteration and the starting and the deformed structure are shown. However, predefined parameters for optimization, determining the number of cavities inside the filter, are required. In [36] and [37], topology optimization is used for metallic microwave insert filters requiring the designer to define the number of poles in some way.

Since artificial intelligence approaches may lead to unconventional and complex structures, conventional manufacturing processes may be unsuitable. However, additive manufacturing seems suitable for rapidly fabricating such structures. In [38], Selective Laser Melting (SLM) metal 3D printing is employed to create a waveguide filter based on cavity resonators. Similarly, in [35], SLM 3D printing is utilized for the aforementioned shape-optimized filter. Both papers present waveguide filters
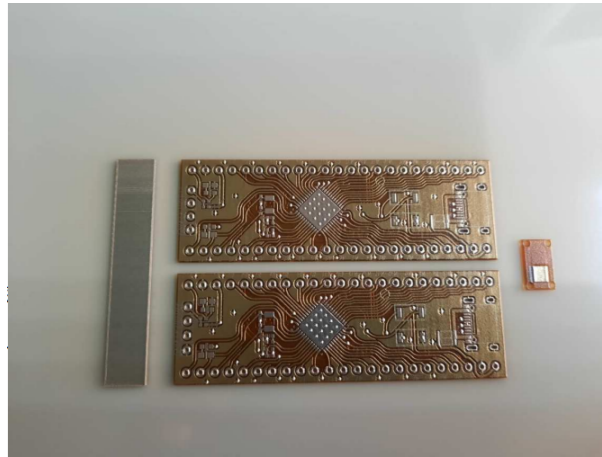

Fig. 1.9: Example of fully 3D-printed PCBs. Adopted from [32].
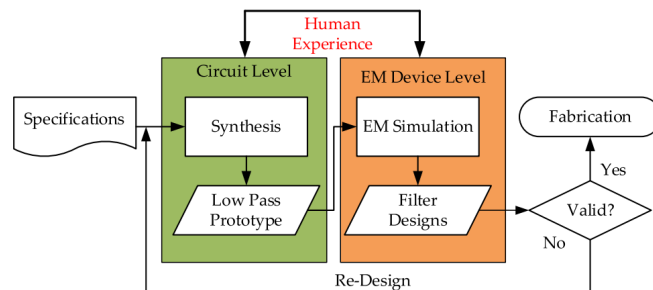
Fig. 1.10: General traditional design flow for microwave filters. Adopted from [34].

for the K_u band and demonstrate good agreement between the measured and simulated data. While SLM shows promise in K_u band applications, surface roughness might pose challenges at higher frequencies (Fig. 1.12). SLA 3D printing technology can print precisely with good surface roughness. In [39] and [40], authors presented twisted waveguide filters for the K_a band. Both structures serve polarization twisting and filtering simultaneously. These structures couldn't be manufactured using conventional methods. Moreover, the filters are lightweight due to the polymer material. Additionally, the work in [41] introduces a monolithic 3D-printed filter with a twisted metal-insert bandpass design (Fig. 1.13). In [42], a SLA 3D-printed waveguide filter for the W band is presented. The filter has a perforated construction with very tiny elements (0.5mm wide slots). The SLA 3D printing process

Fig. 1.11: Optimization error per iteration step during the filter shape deformation technique. Adopted from [35].

(a)   (b)

Fig. 1.12: SLM 3D-printed waveguide filter (a) and its cross-section (b). Adopted from [38].

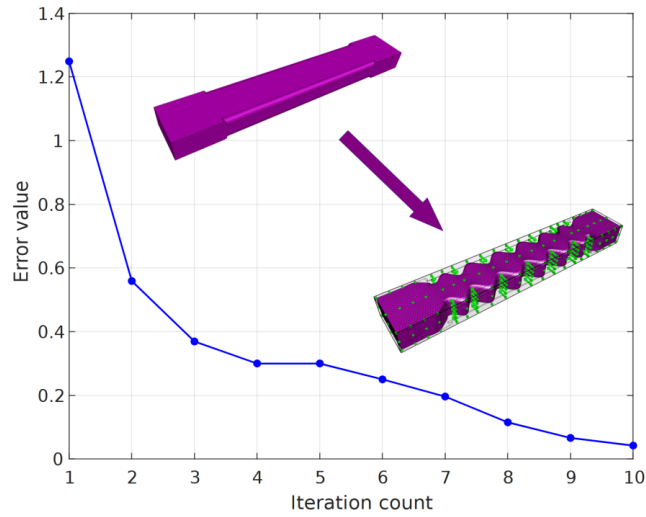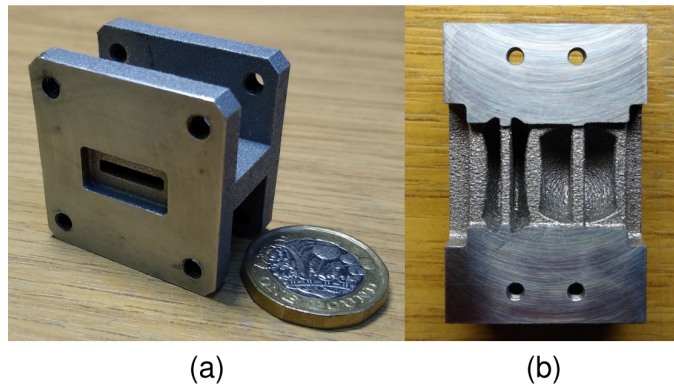provided precise structure resulting in good agreement with simulated data. A filter for the X band based on spherical resonators is presented in [43]. 3D printing enables the manufacturing of a special topology of the filter. Measurements also show very good agreement with simulated data. However, one limitation of these designs lies in the necessity for metal plating. For microwave waveguide filters, FDM 3D printing is also a viable choice. In [44], a customizable 3D-printed insert that can be placed into a standard WR-90 waveguide to realize a waveguide filter is presented. The plastic inserts were coated with nickel spray and electroplated with copper. A relatively high insert loss was achieved, attributed to the surface roughness of the 3D-printed structure. A waveguide filter manufactured using FDM print technology is presented in [45], manufactured in two pieces cut in the E-plane. The impact of E-plane and H-plane cuts on the filter performance of 3D-printed waveguide filters manufactured with FDM is examined in [46]. The authors recommend manufacturing filters separated in the E-plane, providing better and more consistent results. As evident, all these designs require the metalization of the printed parts which may also pose a challenge.

The current trend in microwave waveguide filter design is moving towards automation with a focus on achieving fully autonomous procedures. Artificial intelligence approaches often result in unconventional and complex structures, necessitating the use of 3D printing technology. Recent advancements demonstrate the suitability of 3D printing for manufacturing microwave waveguide filters. However, future investigations need to address challenges such as surface roughness in metal 3D printing technologies, metal coating of 3D-printed dielectric structures, and potential dielectric losses in 3D-printed materials.
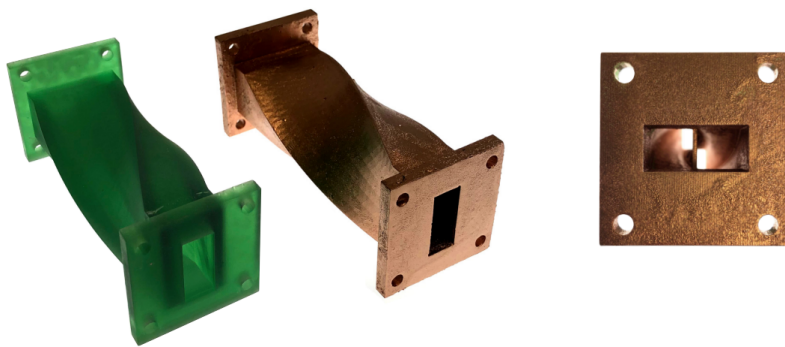

Fig. 1.13: Prototype of twist-component filter. Left image depicts prototype made from translucent-green photo-polymer resin while center and right images depict prototype with a base layer of copper aerosol-spray. Adopted from [41].

1.4 3D-Printed Materials and Their Characterization

For the design of microwave structures, it is essential to know the properties of the used dielectric materials. Therefore, in the case of 3D-printed materials, a suitable characterization process of electromagnetic properties is necessary. Thermoplastics are the most commonly used materials for FDM 3D printing technology. Consequently, the majority of published works focus on characterizing these materials. Since thermoplastics are non-magnetic, only their complex permittivity is typically considered in their characterization. The published results are summarized and discussed in this section. The state-of-the-art results are listed in Table 1.1.

In [47], the results of complex permittivity measurements of PLA in the DC-18 GHz band are presented. For measurements, the Transmission-Reflection (TR) method is used. This method is based on the measurement of the scattering parameters of a sample located in a sample holder. A piece of waveguide or a coaxial line can be used as the sample holder (Fig. 1.14). In [50], the TR method is used and incorporated with an optimization process to minimize measurement error. The algorithm finds the best ϵ_r that minimizes the mean squared error between the measured scattering parameters and the model based on Nicholson-Ross-Weir (NRW) equations [55]. Measurements of a wide range of materials, some intended for 3D

Material	$\epsilon_r'(-)$	$\epsilon_r''(-)$	$\mu_r'(-)$	$\mu_r''(-)$	f(GHz)	Ref
PLA	2.75	0.041	-	-	0-18	[47]
PLA	2.75	0.03	-	-	0.5-20	[48]
PLA	2.75-2.93	0.033-0.045	-	-	40	[48]
PLA	2.57	0.024	-	-	30-50	[48]
PLA	2.74-3.05	0.039-0.051	-	-	60	[48]
PLA	3.47	0.25	-	-	9-10	[49]
PLA cond.	6.81	3.36	-	-	9-10	[49]
PLA mag.	3.65	0.68	-	-	9-10	[49]
ABS	2.4	0.013	-	-	30-50	[50]
Porcelite	3.3	0.086	-	-	55-95	[51]
Vorex	2.6	0.049	-	-	55-95	[51]
NinjaFLEX	2.95	0.177	-	-	2.4	[52]
TW-CON175BK	9.93-10.3	2.88-2.58	1	0	8-12	[53]
CopperFill	8	0.48	0.7	0.07	10	[54]
BrassFill	8.15	0.12	1.25	0.25	10	[54]

Tab. 1.1: Comparison of published values of complex relative permittivity and permeability of 3D-printed materials.

printing, have been made in the 30-50 GHz band and presented in this work. The TR method is very sensitive to the geometric accuracy of the measured samples. If the material sample does not completely fill the sample holder cross-section, air gaps are created around the sample which can lead to significant measurement errors.

In [48], the results of measurements of the complex permittivity of PLA in the band 0.5-20 GHz are presented. For the characterization, a microstrip structure with two coupled resonators is used. The complex permittivity of the material is extracted using an optimization process. A numerical model of the structure is optimized, and the difference between measured and simulated scattering parameters is used as a fitness function. One disadvantage of this method lies in the necessity of applying the optimization process during the extraction.

In [52], a flexible 3D-printed material "Ninja FLEX" is characterized using a method that employs a planar circular resonator. The dielectric constant of the material is extracted from the shift of the resonant frequency. The main disadvantage of this method is that it is a narrowband measurement technique.

Composite materials designed for 3D printing, created by mixing thermoplastic with suitable additives, may contain metallic additives. The determination of complex permittivity and complex permeability of the materials measured in [53] and [54] utilized the TR method. Measurement of parameters of ABS with carbon additives intended for 3D printing is published in [53]. The material exhibits very specific properties. In the X-band, the real part of permittivity is about 10 and slightly decreases with increasing frequency. The addition of carbon increases the
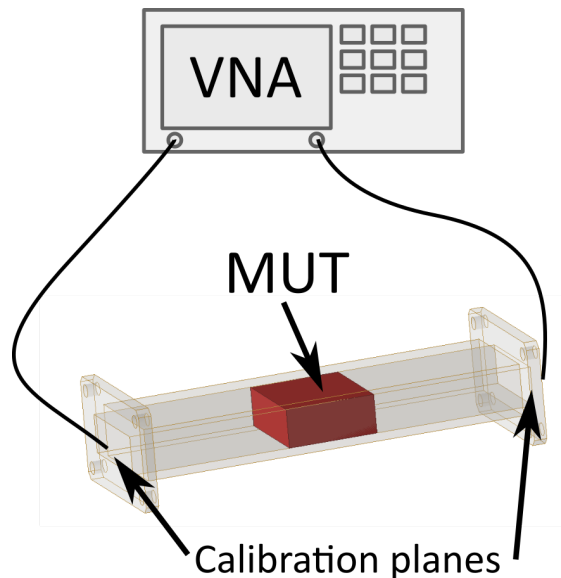

Fig. 1.14: Transmission-Reflection measurement setup where a piece of waveguide is used as a sample holder.

imaginary part of the permittivity, leading to dielectric losses of about 0.27. This material is used to design a matched load in a rectangular waveguide in this work. In [54], measurements at 10 GHz of two materials based on PLA with the addition of metal powders are published. The measured materials are "CopperFill" with the addition of copper powder and "BrassFill" with the addition of brass powder. For "CopperFill," the extracted real part of permittivity is 8, the electric loss tangent 0.06, the real part of permeability 0.7, and the magnetic loss tangent 0.1. The "BrassFill" material exhibits the real part of permittivity 8.15, the electric loss tangent 0.015, the real part of permeability 1.25, and the magnetic loss tangent 0.2. The behavior of the materials is explained by percolation phenomena in the microwave regime. The conductive particles tend to form clusters, which cause eddy currents and therefore provide effective magnetic behavior with artificial effective relative permeability.

Drawing from state-of-the-art findings, it becomes evident that the permittivity of 3D-printed materials can exhibit variations even within the same material type. It is plausible that materials sourced from different manufacturers might possess slight compositional differences resulting in distinct electromagnetic properties. Additionally, the color of a given material could introduce further variations. Consequently, before delving into investigations of 3D-printed microwave structures, it becomes imperative to employ a suitable process for the material characterization of the 3D-printed materials. The TR method using NRW calculation seems a suitable solution [56]. The procedure enables extraction of complex permittivity as well as complex permeability. The method is adept at providing broadband measurements and is applicable up to 100 GHz utilizing a designated waveguide as a sample holder. For lower frequencies, coaxial lines can be employed.

2 Objectives

The previous state-of-the-art chapter briefly summarized the potential of pixelated structures in terms of microwave applications. A crucial aspect is an effective optimization procedure, where there seems to be room for the development of an optimization algorithm that automatically accounts for the varying significance of individual pixels. Pixelated structures may be promising for a wide range of SIW horn antennas. The use of pixelated structures can lead to unconventional solutions and help address certain limitations of SIW horn antennas such as unequal radiation patterns in the principal planes. Since pixelated structures can provide non-traditional solutions tailored to the desired parameters of the final design, they are also promising in terms of automated design procedures for microwave structures such as waveguide filters. Based on these considerations, three objectives of this dissertation thesis can be formulated.

As discussed in the last subchapter of the state-of-the-art section, the electromagnetic parameters of materials must be known in order to design microwave structures. Since this dissertation focuses on 3D-printed microwave structures, the first logical step is to determine the electromagnetic properties of the 3D-printed materials. Therefore, the third chapter focuses on this topic.

Objective 1

Development of an Efficient Optimization Procedure for Pixelated Structures.

As evident from state-of-the-art literature, pixelated structures hold significant promise in the realm of microwave technology. They can significantly enhance performance, reduce size, or mitigate undesired effects. When coupled with 3D printing, a spatial realization of pixelated structures becomes feasible. As structures become more complex, the need for an efficient optimization procedure becomes apparent. Therefore, it is desirable to establish an efficient optimization algorithm suitable for pixelated structures.

Objective 2

Design Procedure for Pixelated SIW Horn Antennas.

Pixelated structures offer significant flexibility in the final shape. Utilizing a dielectric load with a pixelated arrangement for SIW horn antennas holds unique promise for antenna design. The structure can be implemented as a dielectric lattice with each cell either filled or unfilled. By introducing an air inclusion into the filled cell, its effective permittivity can be reduced [57] resulting in a pixelated structure with multistate permittivity. From the state-of-the-art literature, it can be inferred that one of the drawbacks of SIW horn antennas, namely unequal beam widths in principal planes, has not been adequately addressed. Therefore, the focus of this objective will be directed toward resolving this issue.

Objective 3

Automated Design Procedure for Waveguide Microwave Filters Based on Pixelation Strategy.

Despite attempts presented in state-of-the-art works, a fully automated design procedure for microwave waveguide filters has not yet been established. While pixelation is capable of achieving structures with sufficient performance and weak dependence on the initial state the design of a waveguide filter starting from a non-resonant structure could be feasible. This would open up the possibility of a fully automated design procedure based only on the given space and the desired filter response.

3   3D-Printed Material Characterization

For the design of microwave structures, the electromagnetic properties of the materials must be known. Materials for additive manufacturing can be divided into two main categories: homogeneous materials and composite materials consisting of two or more different components. Focusing on the most commonly used 3D-printing technology, FDM, the homogeneous materials are classical thermoplastics such as PLA or ABS. In contrast, heterogeneous materials are thermoplastics with added inclusions. On the market, one can find materials mixed with metal dust (e.g., [58] or [59]), carbon fibers, or cork. These materials are primarily designed to create 3D-printed products that resemble wood, copper, and other textures or to add additional functionality to the material, e.g., to make it electrically conductive, thermally conductive, or magnetically responsive. Obviously, these inclusions can affect the electromagnetic properties of the materials.

In the first subchapter, the characterization of a set of common thermoplastic materials is presented. A Transmission-Reflection (TR) method was used for this characterization. This method is based on measuring the transmission and reflection of a Material Under Test (MUT) located in a sample holder (typically a piece of coaxial line or waveguide). Since thermoplastics are non-magnetic, only complex permittivity is determined for those materials. In the second subchapter, the same method is applied to characterize composite 3D-printed materials. For materials with conductive inclusions, it was observed that the inclusions also affect magnetic properties if they are made of ferromagnetic or ferrimagnetic materials. Therefore, the complex permeability has to be included in the parameter extraction process. Unfortunately, the characterization of 3D-printed composite materials poses significant challenges, and the method used was found to be unsuitable for this purpose.

3.1   Homogeneous Thermoplastic Materials

In this subchapter, the measurement of the complex permittivity of common materials used in FDM, such as ABS, PLA, Polyethylene Terephthalate (PET), and the less common XT co-polyester [60], is presented. The results were published in the conference paper [JZ61]. The measurements were performed in the frequency range from 1 to 10 GHz. For the measurement, the TR method was employed [55], which is based on measuring the scattering parameters of a sample placed in a sample holder using a Vector Network Analyzer (VNA).

To extract the complex permittivity, an iterative procedure described in [62] was used. The equations were simplified for the case where the measurement is conducted in a coaxial line ($\lambda_c \to \infty$) and the materials under investigation are non-magnetic

$(\mu_r^* = 1)$. The complex relative permittivity

$$\varepsilon_r^* = \varepsilon_r' - j\varepsilon_r'' \tag{3.1}$$

can be obtained by solving the following equation:

$$S_{21}S_{12} - S_{11}S_{22} = \exp\left[(-2\gamma_0)(L_{air} - L)\right]\frac{z^2 - \Gamma^2}{1 - z^2\Gamma^2}, \tag{3.2}$$

where $S_{21}S_{12} - S_{11}S_{22}$ is the determinant of the scattering matrix. The propagation constant in air, γ_0, can be obtained by:

$$\gamma_0 = j\frac{\omega}{c}, \tag{3.3}$$

where ω is the angular frequency, c is the speed of light in air, and L_{air} and L are the lengths of the sample holder and the measured sample, respectively. The transmission coefficient z is calculated as:

$$z = \exp(-\gamma L), \tag{3.4}$$

where the propagation constant in the measured material, γ, is given by:

$$\gamma = j\frac{\omega\sqrt{\epsilon_r^*}}{c}. \tag{3.5}$$

The reflection coefficient Γ is obtained by:

$$\Gamma = \frac{\frac{c}{c_{lab}}\sqrt{\frac{1}{\epsilon_r^*}} - 1}{\frac{c}{c_{lab}}\sqrt{\frac{1}{\epsilon_r^*}} + 1}. \tag{3.6}$$

In this equation, c_{lab} is the speed of light in the laboratory environment. This procedure is independent of the position of the sample in the sample holder. The real and imaginary parts of the complex relative permittivity must be iteratively determined for each frequency point.

An N-type male coaxial adapter with an air dielectric was used as the sample holder, as shown in Fig. 3.1a. The samples for measurement were fabricated using a Prusa 3D printer (Fig. 3.1b) which operates based on the FDM 3D printing technique with a nozzle diameter of 0.4 mm. The samples were printed using a concentric ring pattern and a 100% infill factor. Each sample had an outer diameter of 7 mm and an inner diameter of 3 mm. The printing process was fine-tuned to ensure the samples fit precisely into the coaxial adapter which is crucial for accurate measurements.

The ABS material is a tough and heat-resistant thermoplastic polymer, typically printed at a nozzle temperature of 255 °C. However, it has some drawbacks, such as lower printing resolution and sensitivity to room temperature variations. PET, the most commonly used thermoplastic polymer, offers durability and excellent layer
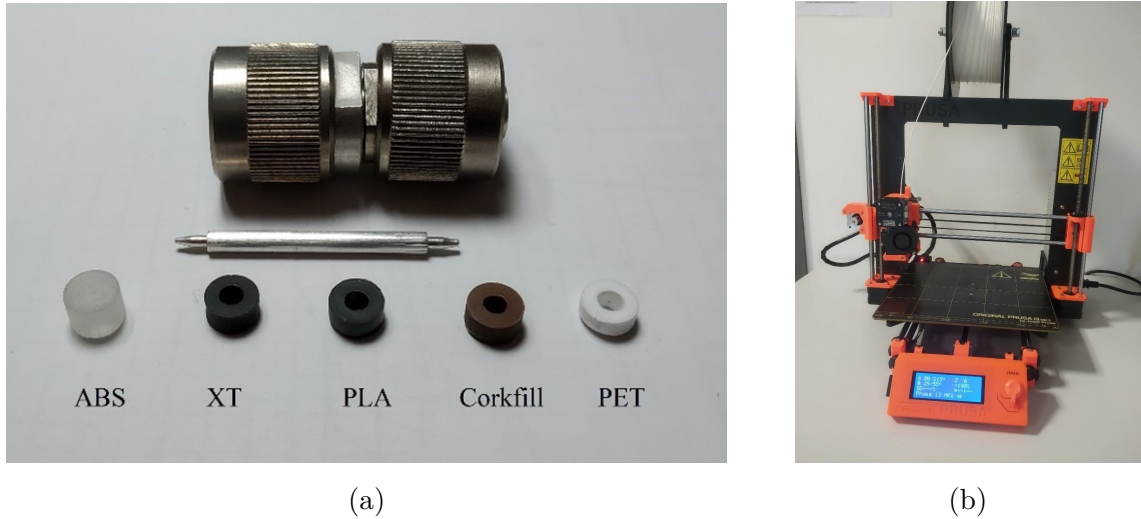
(a)   (b)

Fig. 3.1: (a) Prepared material samples of 3D-printed homogeneous thermoplastic materials and the sample holder. (b) Prusa i3 MK2 3D printer.
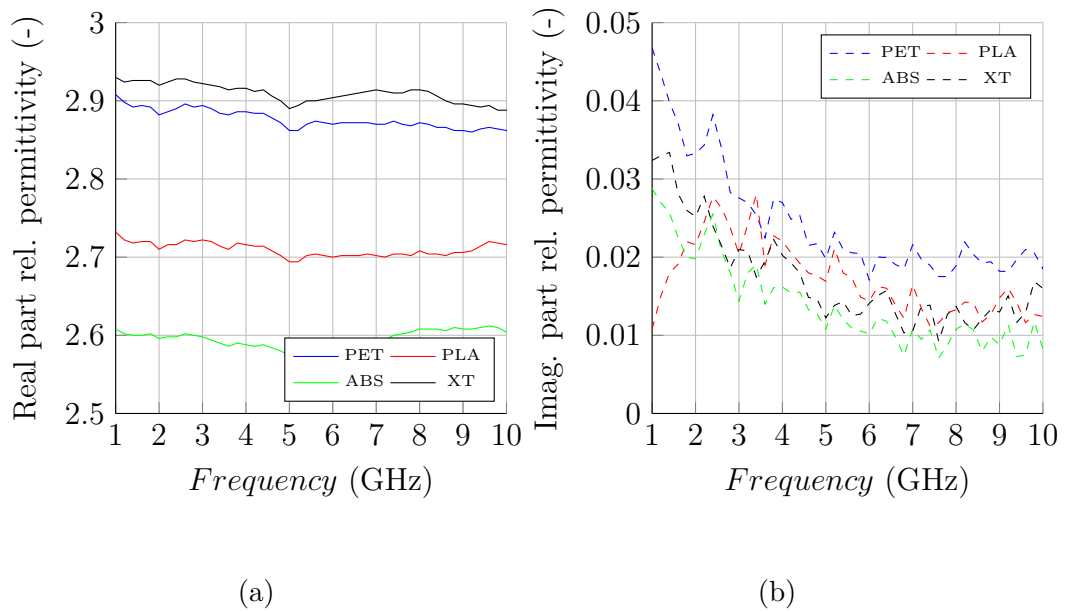

(a)   (b)

Fig. 3.2: Measured results of (a) real part of complex relative permittivity and (b) imaginary part of complex relative permittivity for 3D-printed homogeneous thermoplastic materials.

adhesion, with a recommended printing temperature of 240 °C. The PLA material is highly user-friendly due to its low printing temperature of 215 °C, but it has low heat resistance. Lastly, XT co-polyester is more durable and heat-resistant than PLA, with a printing temperature range of 240–260 °C and excellent layer adhesion.

The measured results are presented in Fig. 3.2. The real part of the relative

| Material | Complex relative permittivity | | | | Ref. frequency range (GHz) |
| | Real part (-) | | Imaginary part (-) | | |
	This work	Referenced	This work	Referenced	
ABS	2.6	2.4 [50]	0.014	0.0132 [50]	30 to 50
		2.8 [63]		0.0252 [63]	2 to 20
PET	2.87		0.024		
PLA	2.71	2.75 [47]	0.017	0.041 [47]	DC to 18
		2.57-2.72 [50]		0.024-0.027 [50]	30 to 50
		2.75 [48]		0 03[48]	2 to 20
XT	2.91		0.017		

Tab. 3.1: Comparison of measured materials with published values.

permittivity for the tested materials ranges from 2.55 to 2.95. The ABS material exhibited the lowest values of the real part, approximately 2.6, as well as the lowest imaginary part values. In contrast, the XT co-polyester material showed the highest real part values, approximately 2.91. The measurement method proved to be stable, and the obtained results align well with state-of-the-art findings. Tab. 3.1 provides a comparison of the measured results with published data. As is obvious, the values of the complex permittivity for the same materials may slightly differ. This is caused by variations in polymer composition, manufacturing tolerances, and differences in printing parameters such as temperature, layer orientation, or infill density. Even environmental factors like humidity absorption or thermal aging can further influence the material properties over time. This highlights the importance of characterizing materials directly before using them in the design of 3D-printed microwave structures.

3.2 Composite Materials

In this subchapter, the results and conclusions from measurements of 3D-printed composite materials are presented. Two materials, Copperfill [58] and Steelfill [59], made by Colorfabb, are based on a blend of PLA with Polyhydroxyalkanoate (PHA) and an admixture of copper and steel powder, respectively. Note that these materials were developed for printing parts with a metallic-like surface. However, the metallic admixtures in these materials influence their dielectric and magnetic properties.

For the measurement of complex permittivity and permeability, the TR method was used. For the extraction, an explicit solution adopted from [56] was applied. This solution fails if the sample length is a multiple of one-half wavelength within

the sample caused by resonant effects and phase ambiguity in the calculation. Consequently, the method must be extended to address this problem. One approach is based on measuring two samples with different lengths and selecting valid values, excluding ranges where the sample length is a multiple of half the wavelength. Another approach involves measuring a relatively long sample and interpolating regions where the solution fails. A further method relies on measuring a thin sample at frequencies below its first resonance. This requires selecting an optimal sample length for the frequency band of interest, ensuring the sample's first resonance is above this band. However, the sample should also be as long as possible to improve measurement accuracy. Thin samples degrade accuracy, particularly in the imaginary parts of the complex relative permittivity and permeability. The explicit solution's advantage is that extraction is performed directly from the measured data.

The relative complex permeability of the material

$$\mu_r^* = \mu_r' - j\mu_r'' \tag{3.7}$$

can be obtained by

$$\mu_r^* = -\frac{1+\Gamma_2}{1-\Gamma_2}\frac{1}{\gamma_0 L}\left(\ln Z + 2\pi jn\right), \tag{3.8}$$

and the relative complex permittivity

$$\varepsilon_r^* = \varepsilon_r' - j\varepsilon_r'' \tag{3.9}$$

can be expressed as

$$\varepsilon_r^* = \frac{\frac{c^2}{\omega^2}\left[\left(\frac{2\pi}{\lambda_c}\right)^2 - \frac{1}{L^2}\left(\ln Z + 2\pi jn\right)^2\right]}{\mu_r^*}. \tag{3.10}$$

In these equations, γ_0 is the propagation constant, λ_c is the cutoff wavelength of the sample holder, L is the sample length, c is the speed of light, and ω is the angular frequency. The correct value of n can be determined using group delay comparison as described in the NRW technique [56] or by the thin sample approach discussed earlier. The transmission and reflection constants Z and Γ_2 are defined as:

$$\Gamma_2 = -\sqrt{\frac{x - Z^2}{xZ^2 - 1}} \tag{3.11}$$

$$Z = \frac{x+1}{2y} - \sqrt{\left(\frac{x+1}{2y}\right)^2 - 1}, \tag{3.12}$$

where

$$x = (S_{21}S_{12} - S_{11}S_{22})\exp\left[2\gamma_0(L_{air} - L)\right], \tag{3.13}$$

$$y = \left(\frac{S_{21} + S_{12}}{2}\right)\exp\left[\gamma_0(L_{air} - L)\right], \tag{3.14}$$

and the propagation constant in vacuum is defined as

$$\gamma_0 = j\sqrt{\left(\frac{\omega}{c}\right)^2 - \left(\frac{2\pi}{\lambda_c}\right)^2}. \tag{3.15}$$

In equations 3.13 and 3.14, S_{11}, S_{12}, S_{21}, and S_{22} represent the measured scattering parameters, and L_{air} is the length of the empty sample holder.

The samples were prepared in the same way as in the case of the homogeneous thermoplastic materials. The samples were also fabricated using the Prusa 3D printer with the 0.4 mm nozzle using the concentric ring print style with the 100% infill factor. A set of samples was made with lengths of 1, 2, 3, and 4 mm. The ideal length of the samples was determined as described above. The scattering parameters of the samples, once inserted into the sample holder, were measured, and the first resonances, which indicate half of the wavelength in the measured materials, were determined. The ideal length of the samples was 2 mm, which enabled the extraction of the complex permittivity and permeability up to 10 GHz. The extracted parameters are shown in Fig. 3.3. Measurements were also conducted in waveguides R100 and R70 to compare the results. A set of samples (2 mm, 3 mm, and 4 mm for R100; 2 mm, 4 mm, and 6 mm for R70) was manufactured as in the previous case to fit the cross-section of the waveguides precisely. The extracted results for the real parts of the measurements conducted in the waveguides compared with the results obtained from coaxial measurements are shown in Fig. 3.4 and Fig. 3.5. The results are shown only for the Copperfill material to demonstrate the behavior of the composite materials with metal inclusion. A similar behavior was also observed for the Steelfill material. It can be seen in Fig. 3.4, the results of the real part of the complex relative permittivity vary between the samples. On the other hand, the results for the real part of the complex relative permeability appear quite stable across the waveguide measurements. The measured results of the Copperfill material were also published in [54] where the Copperfill material was used for manufacturing a frequency-selective surface. The obtained values are $\epsilon_r' = 8$ and $\mu_r' = 0.7$ at 10 GHz, using the same measurement method, which is comparable with the results presented in this work. The authors also mentioned that they performed the measurements several times, and the measured results mostly fit best for the same thickness of the samples (and also for the thickness of the final FSS structures). Based on these observations, it appears that measurements of composite materials should be carried out on samples that are as close as possible to the intended application.
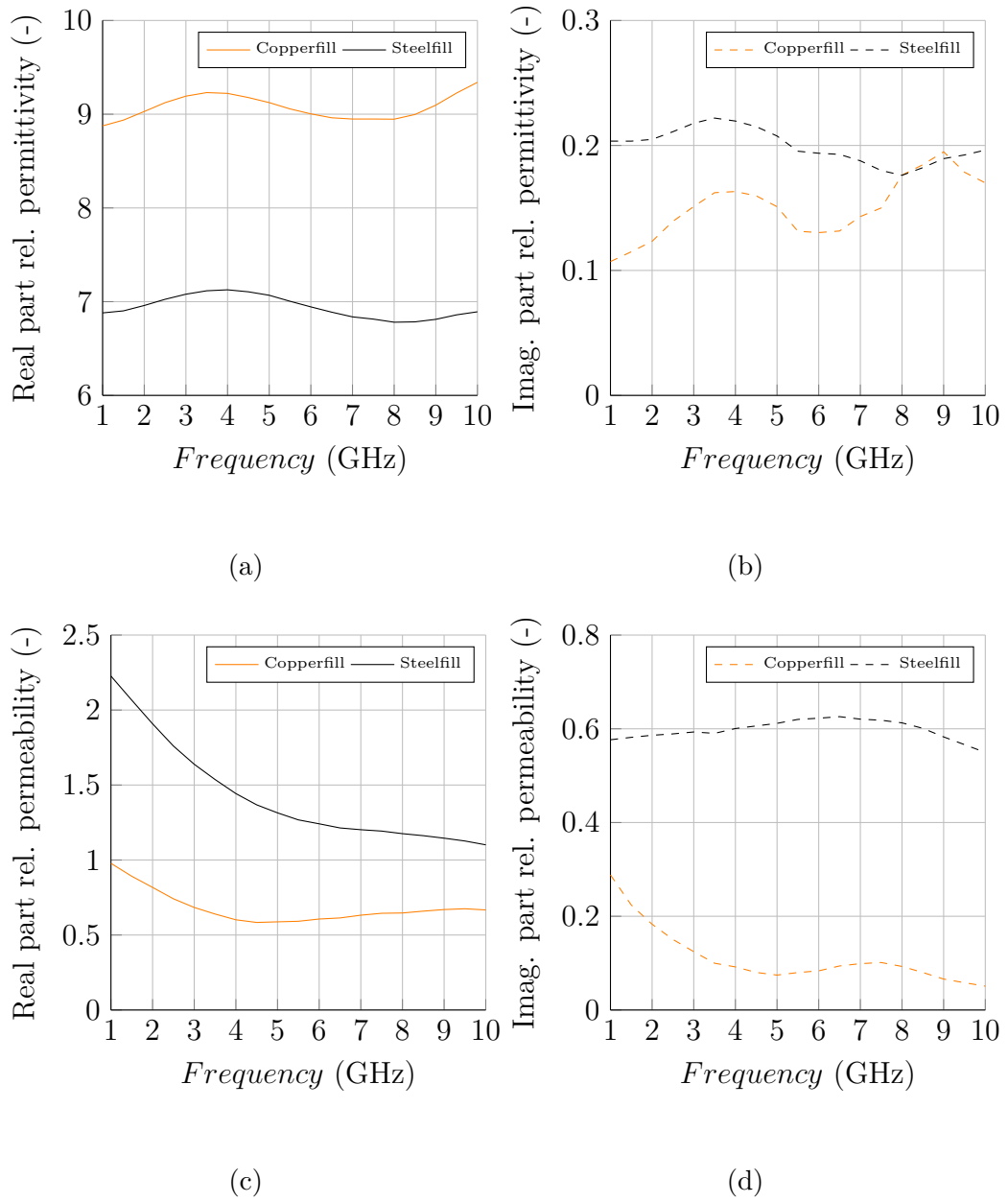
(a)

(b)

(c)

(d)

Fig. 3.3: Measured results of (a) real part of complex relative permittivity, (b) imaginary part of complex relative permittivity, (c) real part of complex relative permeability, and (d) imaginary part of complex relative permeability for measured 3D-printed composite materials.
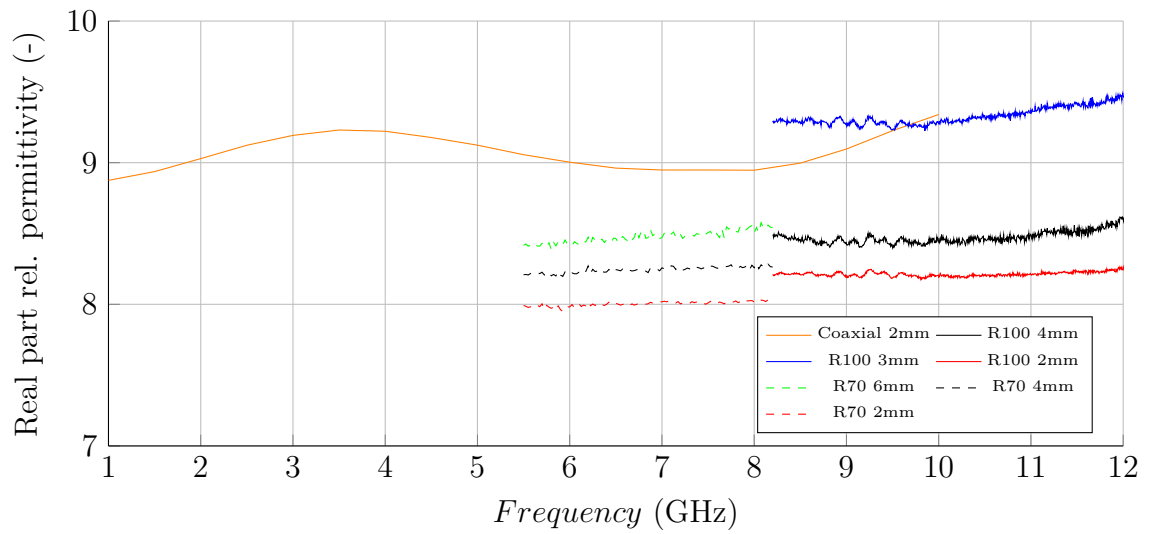
27

Fig. 3.4: Measured results of real part of complex relative permittivity of 3D-printed composite materials. Comparison of results from measurements conducted in a coaxial adapter and waveguides.
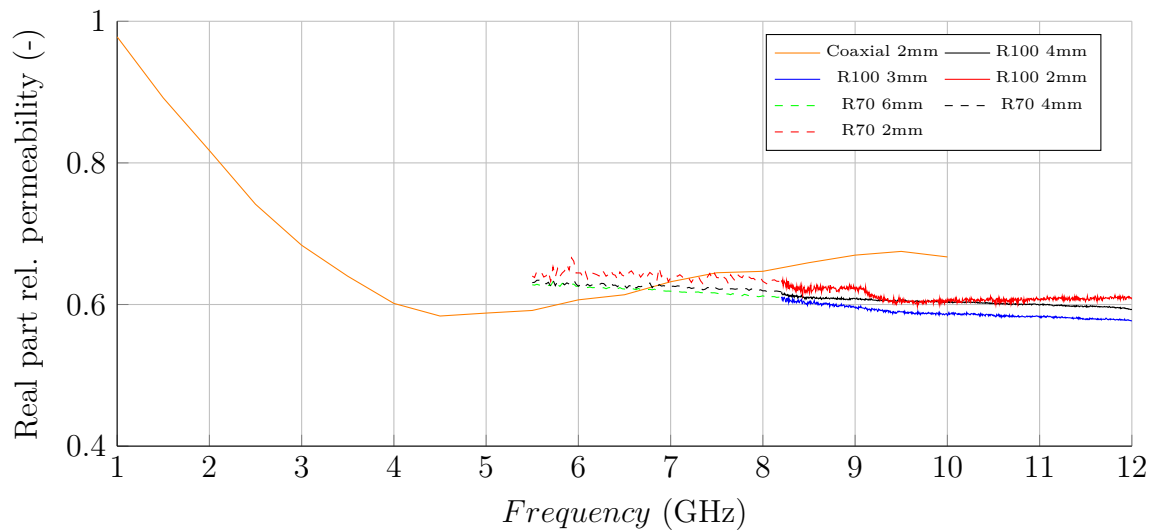

Fig. 3.5: Measured results of real part of complex relative permeability of 3D-printed composite materials. Comparison of results from measurements conducted in a coaxial adapter and waveguides.

3.3 Summary

In this chapter, a suitable method for the characterization of homogeneous thermoplastic materials was adopted and used to measure a set of materials commonly used for FDM 3D printing. The results of the measurements in a coaxial adapter up to 10 GHz were presented in the conference paper [JZ61]. As the next step, the characterization of 3D-printed composite materials was also examined. Since the results obtained from measurements conducted with a coaxial adapter as a sample holder were unstable, measurements using waveguides as sample holders were additionally performed. The results varied for different sample thicknesses which was consistent with the conclusions presented in [54]. Thus, it was concluded that the measurement of 3D-printed composite materials needs to be tailored to the target application. The findings and results will be used further in this dissertation.

While practical applications show slight discrepancies in the electromagnetic parameters of homogeneous thermoplastic materials, future work may focus on the influence of printing profiles and sample orientation during measurement. In the printing process, the first and last few layers can introduce inhomogeneities, potentially affecting the measured parameters of composite material samples with different lengths. Mechanically removing these outer layers may standardize results across samples of various lengths. Alternatively, using a very long sample may help mitigate the influence of these outer layers. These approaches may be subjects for further investigation.

4 Binary Ink Stamp Optimization

In this chapter, a novel heuristic algorithm called Binary Ink Stamp Optimization (BISO) is described. This algorithm is developed specifically for optimizing binary patterns. The key feature of BISO is its ability to reflect the significance of individual bits during optimization. BISO was introduced in the paper [JZ64].

In the first subchapter, the basic principle of the algorithm is presented, and its specific optimization steps are described. Then, the algoritm's behavior during the optimization and influence of the main parameters to the algorithm's convergency are discussed. In the final subchapter, BISO is tested on 15 benchmark functions and the results are compared with six other binary optimization algorithms. The development of this algorithm is related to the Objective 1 of this thesis.

4.1 Algorithm Description

In state-of-the-art works, Genetic Algorithm (GA) is predominantly used as an optimization tool for pixelated antenna structures. GA updates a binary vector using selection, crossover, and mutation procedures [65]. During the optimization process, each bit is given equal significance. However, in real-world applications of binary patterns, certain pixels may have a greater influence on the properties of the structure. In response to this, an evolutionary optimization approach for binary patterns is proposed. BISO reflects the significance of the bits during the optimization process providing a key advantage over other algorithms in terms of optimizing binary patterns.

BISO is a heuristic optimization algorithm designed for binary problems. It draws inspiration from stamps with varying ink saturation. Each stamp corresponds to a previously generated individual with its ink saturation determined by its fitness value. The next generation is determined based on a probability matrix which can be visualized as an imprint of all stamps overlaying each other. Darker positions indicate a higher probability of generating a "1" while brighter positions favor the generation of "0" (Fig. 4.1).

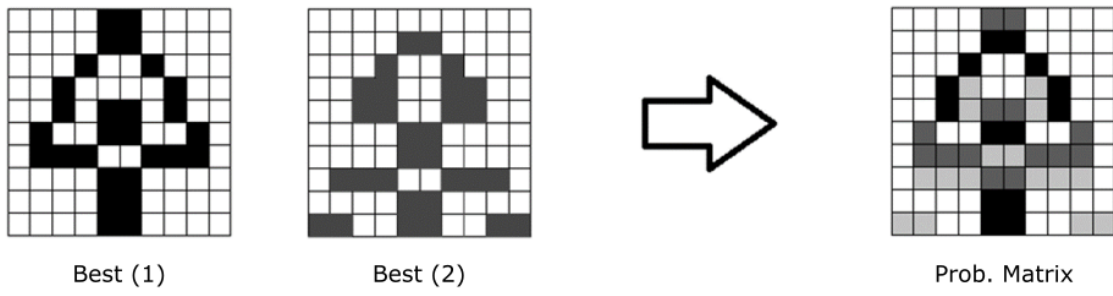The general steps of BISO are depicted in the flow chart in Fig. 4.2.

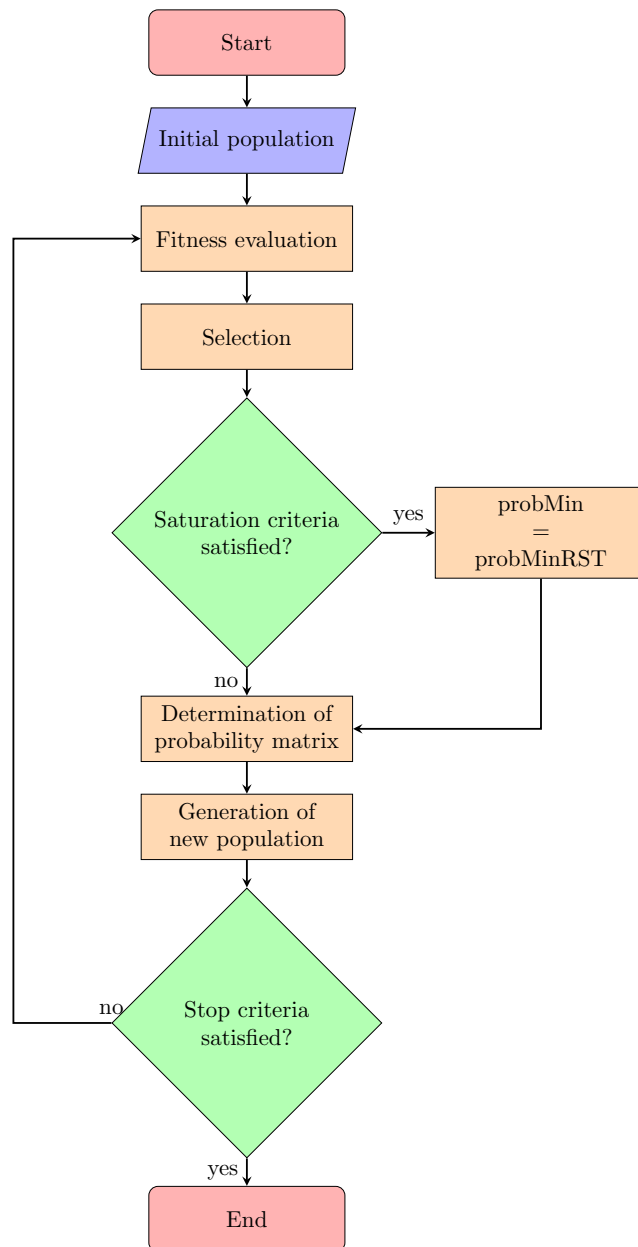Fig. 4.1: Illustration of BISO algorithm principle.

Fig. 4.2: Flow chart of BISO algorithm.

31

The following parameters has to be set at the start of the optimization run:

- *Npop* – the number of individuals in each iteration,
- *Nelit* – the number of selected elitist individuals,
- *Niter* – the maximal number of iterations,
- *probMin* – the minimal probability of generating "1" in the next iteration,
- *probMinRST* – the minimal probability of generating "1" in the next iteration when the algorithm gets stuck in a local extreme and the reset routine is activated,
- *rstCoeff* – the criteria for activation of the reset routine,
- *sigCoeff* – the steepness of the sigmoid function.

At the start, an initial population is randomly generated as a binary matrix of size *Npop×Ndim* where *Ndim* is the number of optimized variables. The rows in this matrix correspond to the individuals of the first population. After the fitness evaluation, individuals are sorted according to their value. A set of individuals with a better rank in the ordered set is selected. At this point, the mean Hamming distance between these elite individuals is determined divided by *Ndim* and compared with *rstCoeff*. This part is designed to prevent the algorithm from being stuck in a local minimum. The decreasing Hamming distance between elite individuals indicates that the sub-region of the domain space has been exhaustively explored and the algorithm has reached a local minimum. In the next step, the probability matrix is determined. To simplify the implementation, the matrix is transformed into a vector. The vector is defined as a weighted sum of components according to the best individuals:

$$probVect(i) = \frac{1}{Nelit} \sum_{k=1}^{Nelit} \begin{cases} [1 - w(k)] & \text{if } \mathbf{Elite}(k, i) = 1 \\ w(k) & \text{if } \mathbf{Elite}(k, i) = 0 \end{cases}, \qquad (4.1)$$

where i is the index of the variable, $\mathbf{Elite}$ is the matrix of the elite individuals, k is the index of the individual in $\mathbf{Elite}$, and w denotes the weight of an individual according to the sigmoid function:

$$w(k) = probMin + \frac{0.5 - 2probMin}{1 + exp[-\frac{1}{meanE}f(k) - sigCoeff \times meanE]}, \qquad (4.2)$$

where $meanE$ is the mean fitness value of the current elite individuals, and f denotes the fitness value. The range of the sigmoid function 4.2 is from *probMin* (specified by the user) to $0.5 - probMin$. These two values determine the minimum and maximum probability of generating "1". The *probMin* parameter significantly influences the convergence rate of the algorithm. For high values of the parameter ($probMin > 0.1$), the convergence rate is low, and achieving an optimum requires a high number

of iterations. However, for low values of the parameter, the algorithm strongly converges toward the nearest minimum. For this purpose, the so-called "reset" routine is implemented. If the Hamming distance between the elite individuals of one population is below *Ndim×rstCoeff*, the value of the parameter *probMin* is set to *probMinRST*. In the case that the value of *probMinRST* is 0.5, the next population is generated randomly.

The new population is generated according to the following equation in every iteration:

$$newPop(j,i) = \begin{cases} 1 & \text{if} \quad rand \leq probVect(i) \\ 0 & \text{if} \quad rand > probVect(i) \end{cases}, \tag{4.3}$$

where $j \in \{1, 2, ..., Npop\}$.

4.2   Algorithm Behaviour

This subchapter shows the influence of the algorithm's settings on its convergence during optimization. A typical algorithm convergence is shown in Fig. 4.3. The red curve corresponds to the fitness value of the best individual found so far and the blue curve corresponds to the mean fitness values of the elite individuals in the current generation. The peaks visible in the mean value of the elite individuals are caused by the reset routine, which introduces a much higher degree of randomness into the next generation once its activation criterion is met (to be discussed later).
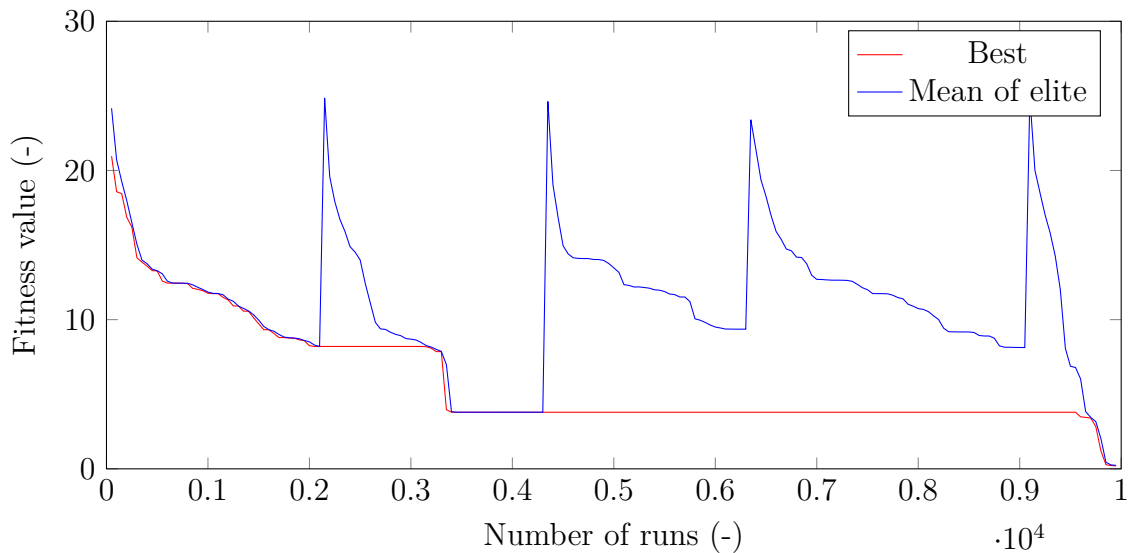

Fig. 4.3: Example of convergence of BISO algorithm over fitness function runs.

By adjusting the algorithm's parameters, it is possible to balance between its ability for exploration and exploitation. In practice, it is advantageous to understand the complexity of the problem being optimized as this allows the algorithm's settings to be better tailored.

Sample runs of the algorithm with different settings were performed to demonstrate its behavior and convergence. The parameters chosen to illustrate the algorithm's behavior are those that strongly influence its performance and are unique to this algorithm. These parameters are $minProb$, $minProbRST$, and $rstCoeff$. The f_{b2} test function (described in Tab. 4.2) with a dimension of 100 was used for the sample runs. The default settings of the algorithm are shown in Tab. 4.1.

The $minProb$ parameter, which describes the minimum probability of generating a logic 1, was set to 0.005, 0.01, 0.02, and 0.03. The test runs are shown in Fig. 4.4. In general, this parameter mainly influences the frequency of reset routines. A lower value of this parameter results in faster convergence to a local minimum. If the $minProb$ parameter is set too low, there may be insufficient exploration of subareas as the algorithm can easily get stuck in a nearby minimum. On the other hand, setting it to a higher value leads to an overly extensive search of the subregion which may slow down the overall convergence of the algorithm. For relatively high values, the individuals in each new generation are formed with such a degree of randomness that the reset routine condition is very unlikely to be met as can be seen in Fig. 4.4d. Thus, it is generally preferable to set the $minProb$ parameter to a lower value. Unless the behavior of the optimization problem is well understood, the value should not exceed 0.01.

The $minProbRST$ parameter is identical in principle to the previous parameter: it specifies the minimum probability of generating a logical 1. However, the $minProbRST$ parameter is applied only if the condition for the algorithm's reset routine is met. If its value is 0.5, the next generation is generated completely randomly resulting in a true reset of the algorithm run. The test runs were conducted for $minProbRST$ values of 0.1, 0.2, 0.3, and 0.5 (Fig. 4.5). If its value is lower than 0.5, the next generation still contains some information about the previous generations,

Parameter	Value	Parameter	Value
$Nelit$	5	$minProb$	0.01
$Niter$	200	$minProbRST$	0.5
$Npop$	50	$sigCoeff$	10
		$rstCoeff$	0.01

Tab. 4.1: Basic parameter settings for BISO algorithm for the test runs.

but it is generated with much higher randomness. This can be advantageous if the optimization problem contains some very significant bits that strongly influence the behavior of the optimized function. The fingerprint of these bits will still be present to some extent in the next generation, so the algorithm does not need to "detect" the significance of these bits again. The function chosen for the demonstration runs is an example of this type of problem. This function contains several significant bits that determine the parameters of a sine function which is used to modulate the rest

(a) $minProb = 0.005$

(b) $minProb = 0.01$

(c) $minProb = 0.02$
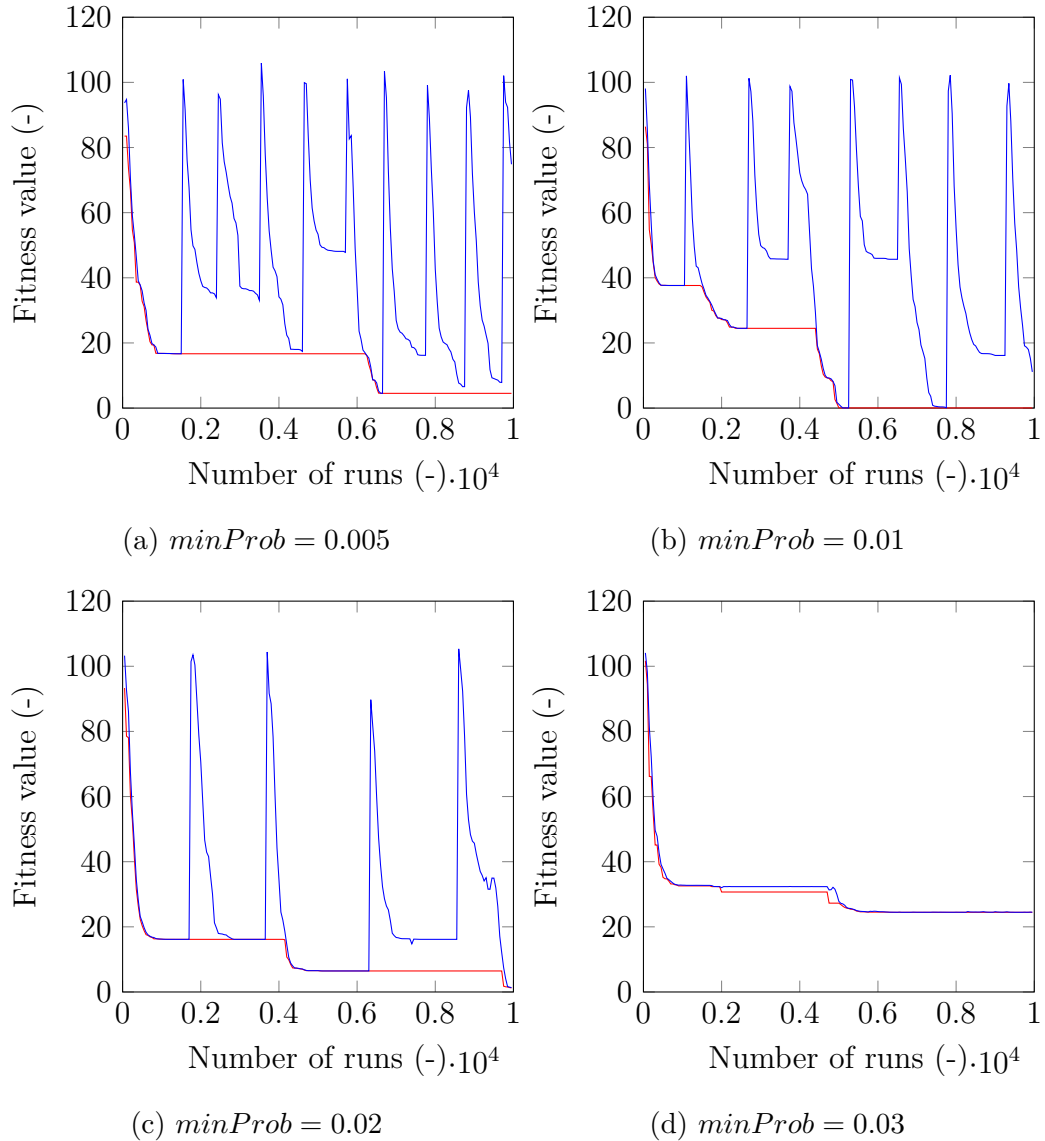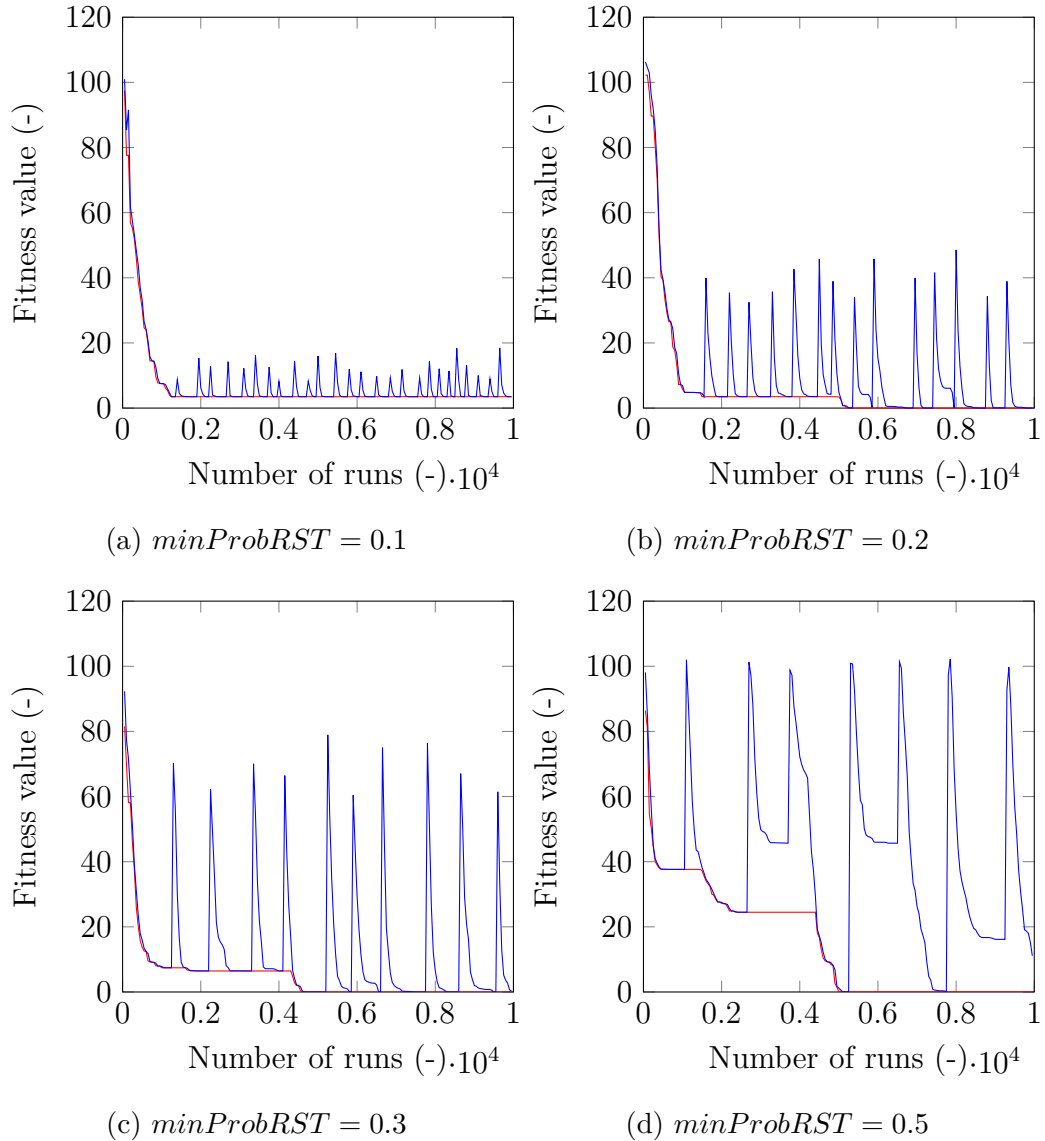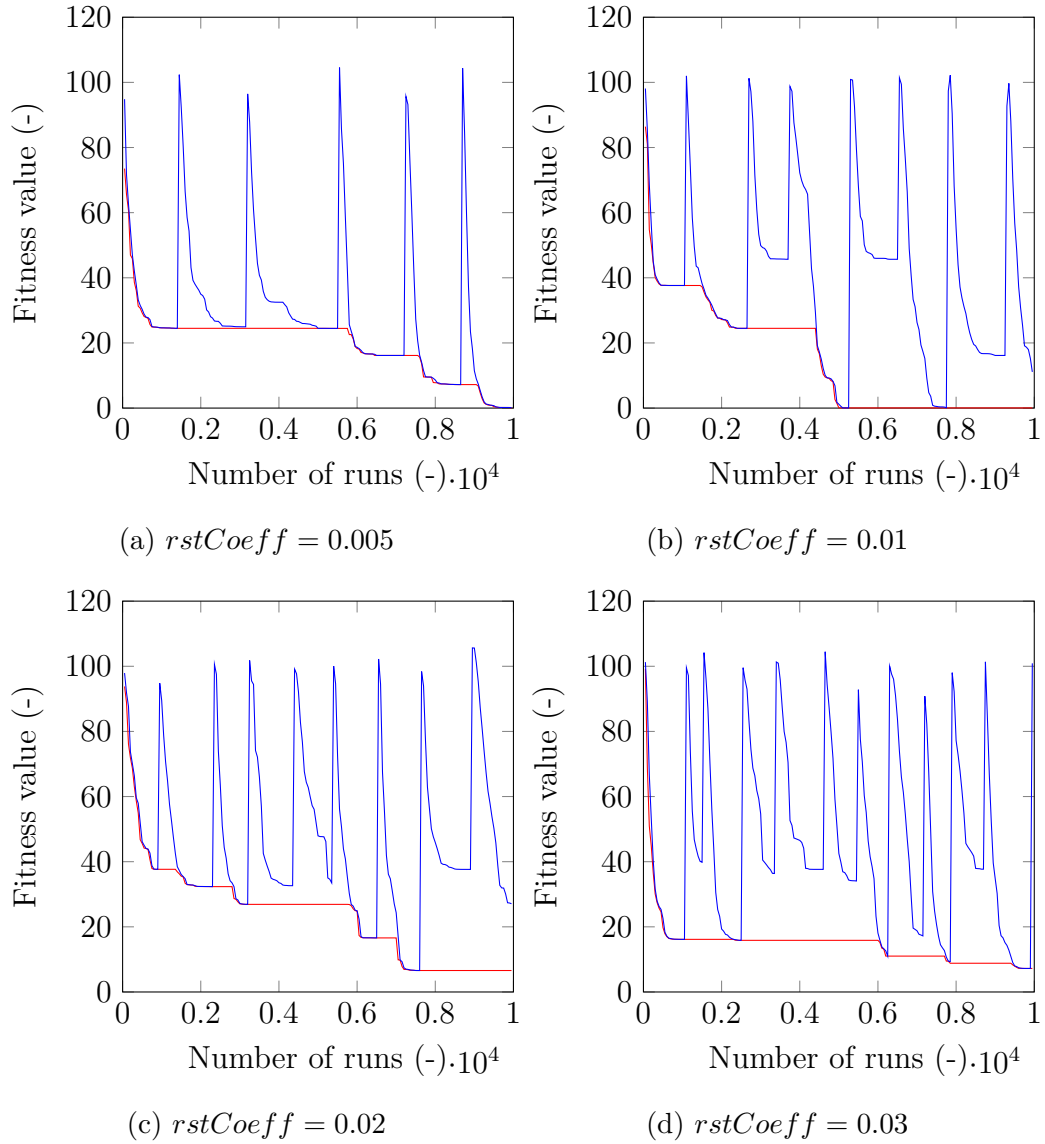
(d) $minProb = 0.03$

Fig. 4.4: Convergence examples of BISO algorithm with $minProb$ set to (a) 0.005, (b) 0.01, (c) 0.02, and (d) 0.03. Red curve represents fitness value of the best individual so far, and blue curve represents mean fitness value of elite individuals in current iteration.

35

of the bits. The sum of the modulated bits is then the output of the test function. Thus, it is more convenient to use a value for $minProbRST$ less than 0.5 for this type of function. On the other hand, if the optimized problem contains very steep local extremes setting a lower value may make it more difficult for the algorithm to leave the region of this extreme. Therefore, in general, it can be recommended to set the $minProbRST$ parameter to 0.5. This ensures that the algorithm will not get stuck in a local extreme when a reset routine occurs.

(a) $minProbRST = 0.1$

(b) $minProbRST = 0.2$

(c) $minProbRST = 0.3$

(d) $minProbRST = 0.5$

Fig. 4.5: Convergence examples of BISO algorithm with $minProbRST$ set to (a) 0.1, (b) 0.2, (c) 0.3, and (d) 0.5. Red curve represents fitness value of the best individual so far, and blue curve represents mean fitness value of elite individuals in current iteration.

The parameter $rstCoeff$ specifies the condition for applying the reset routine of the algorithm. Test runs for $rstCoeff$ values of 0.005, 0.01, 0.02, and 0.03 are shown in Fig. 4.6. If the mean Hamming distance between the individuals in the elite group (divided by the dimension of the optimization problem) is less than $rstCoeff$, the reset routine is invoked. Thus, this parameter indicates the depth to which the current subregion is searched. If it is set to a lower value, the individuals in the elite group must be very close to each other which suggests they are also close

(a) $rstCoeff = 0.005$

(b) $rstCoeff = 0.01$

(c) $rstCoeff = 0.02$

(d) $rstCoeff = 0.03$

Fig. 4.6: Convergence examples of BISO algorithm when $rstCoeff$ was set to (a) 0.005, (b) 0.01, (c) 0.02, and (d) 0.03. Red curve represents fitness value of the best individual so far, and blue curve represents mean fitness value of elite individuals in current iteration.

to the local minimum. If the parameter is set to a higher value, the algorithm is less likely to reach a local minimum. On the other hand, a higher value allows the algorithm to leave the subregion faster and explore a larger part of the state space in fewer generations. In general, it is recommended to set the parameter to 0.01. However, for less computationally expensive problems, it is possible to set the value even lower to ensure a higher probability of finding true local minima.

4.3 Benchmark Results

BISO was tested on 15 benchmark functions with binary variables and compared with 6 other binary optimization algorithms. Most of the benchmark functions (f_1-f_{13}) were adopted from [66]. The selected benchmark functions can be divided into two categories: unimodal (f_1-f_7) and multimodal (f_7-f_{13}) functions. The unimodal functions are useful for examining the convergence rate of optimization algorithms while the multimodal functions benchmark the ability of algorithms to avoid local minima. Another two test problems (f_{b1}, f_{b2}) were proposed to measure the Hamming distance and weighted Hamming distance between the current individual and the goal vector, respectively. Definitions of the benchmark functions are listed in Tab. 4.2. The state-of-the-art algorithms for comparison were Binary Particle Swarm Optimization (BPSO) [67], Genetic Algorithm (GA) [65], Binary Covariance Matrix Adaptation Evolution Strategy (BCMAES) [68], Binary Bat Algorithm (BBA) [66], Binary Dragonfly Algorithm (BDA) [69], and Multi-Verse Optimization (MVO) [70]. The algorithms were tested with four different dimensions ($Ndim = \{30, 120, 300, 900\}$) for each function. Please note that the results are averaged over 100 independent optimization runs. The obtained results are graphically illustrated in Fig. 4.7-4.10 and summarized in appendix (Tab. 1-4).

From the results, it can be concluded that BCMAES provides the worst results in most cases. In some instances, MVO has achieved good results, but overall, poorer performance prevails. BPSO performed well for a lower number of dimensions but was not always effective for higher-dimensional cases. Similarly, BDA yielded worse results in some cases with a larger number of dimensions. BISO, GA, and BBA were the most efficient; however, BBA significantly underperformed in a few cases (e.g., f_5 and f_{11} for $Ndim = 900$). BISO and GA consistently achieved very good results across all tested functions and dimensions. In direct comparison, BISO outperformed GA in most cases.

Symbol	Function	Range	f_{opt}
f_1	$f_1 = \sum\limits_{i=1}^{N} x_i^2$	$\langle -100, 100 \rangle$	0
f_2	$f_2 = \sum\limits_{i=1}^{N} |x_i| + \prod\limits_{i=1}^{N} |x_i|$	$\langle -10, 10 \rangle$	0
f_3	$f_3 = \sum\limits_{i=1}^{N} \left(\sum\limits_{j=1}^{i-1} x_j \right)^2$	$\langle -100, 100 \rangle$	0
f_4	$f_4 = max_i \{ |x_i|, 1 \le i \le N \}$	$\langle -100, 100 \rangle$	0
f_5	$f_5 = \sum\limits_{i=1}^{N} \left[100 \left(x_{i+1} - x_i^2 \right)^2 + (x_i - 1)^2 \right]$	$\langle -30, 30 \rangle$	0
f_6	$f_6 = \sum\limits_{i=1}^{N} (x_i + 0.5)^2$	$\langle -100, 100 \rangle$	0
f_7	$f_7 = \sum\limits_{i=1}^{N} i x_i^4$	$\langle -1.28, 1.28 \rangle$	0
f_8	$f_8 = \sum\limits_{i=1}^{N} -x_i \sin \left(\sqrt{|x_i|} \right)$	$\langle -500, 500 \rangle$	$-418.983 \times N$
f_9	$f_9 = \sum\limits_{i=1}^{N} \left[x_1^2 - 10 \cos (2\pi x_i) + 10 \right]$	$\langle -5.12, 5.12 \rangle$	0
f_{10}	$f_{10} = -20 \exp \left(-0.2 \sqrt{\frac{1}{N} \sum\limits_{i=1}^{N} x_i^2} \right) - \exp \left[\frac{1}{N} \sum\limits_{i=1}^{N} \cos (2\pi x_i) \right] + 20 + e$	$\langle -32, 32 \rangle$	0
f_{11}	$f_{11} = \frac{1}{4000} \sum\limits_{i=1}^{N} x_i^2 - \prod\limits_{i=1}^{N} \cos \left(\frac{x_i}{\sqrt{i}} \right) + 1$	$\langle -600, 600 \rangle$	0
f_{12}	$f_{12} = -\sum\limits_{i=1}^{N} \sin (x_i) \left[\sin \left(\frac{i x_i^2}{\pi} \right) \right]^{2m}, m = 10$	$\langle 0, \pi \rangle$	-1.801*
f_{13}	$f_{13} = \left\{ \left[\sum\limits_{i=1}^{N} \sin^2 (x_i) \right] - \exp \left(-\sum\limits_{i=1}^{N} x_i^2 \right) \right\} \exp \left[-\sum\limits_{i=1}^{N} \sin^2 \left(\sqrt{|x_i|} \right) \right]$	$\langle -10, 10 \rangle$	-1
f_{b1}	$f_{b1} = \sum\limits_{i=1}^{N} |x_i - x_{i,goal}|$	$\langle 0, 1 \rangle$	0
f_{b2}	$f_{b2} = \sum\limits_{i=16}^{N} \left| x_i A \sin^{2E} \left(\frac{2\pi i}{P} \right) - x_{i,goal} A_{goal} \sin^{2E_{goal}} \left(\frac{2\pi i}{P_{goal}} \right) \right|$	$\langle 0, 1 \rangle$	0

$A = 1 + \frac{10}{2^5} \sum\limits_{i=1}^{5} x_i 2^{i-1}$

$P = \frac{Nbin}{2} \left[1 + \frac{1}{2^5} \sum\limits_{i=6}^{10} x_i 2^{i-6} \right]$

$E = 1 + \sum\limits_{i=11}^{15} x_i 2^{i-11}$

*Global minimum for $N = 2$, global minima for $N = \{8, 20, 60\}$ are published in [71]

Tab. 4.2: Benchmark functions used for evaluation of BISO algorithm.
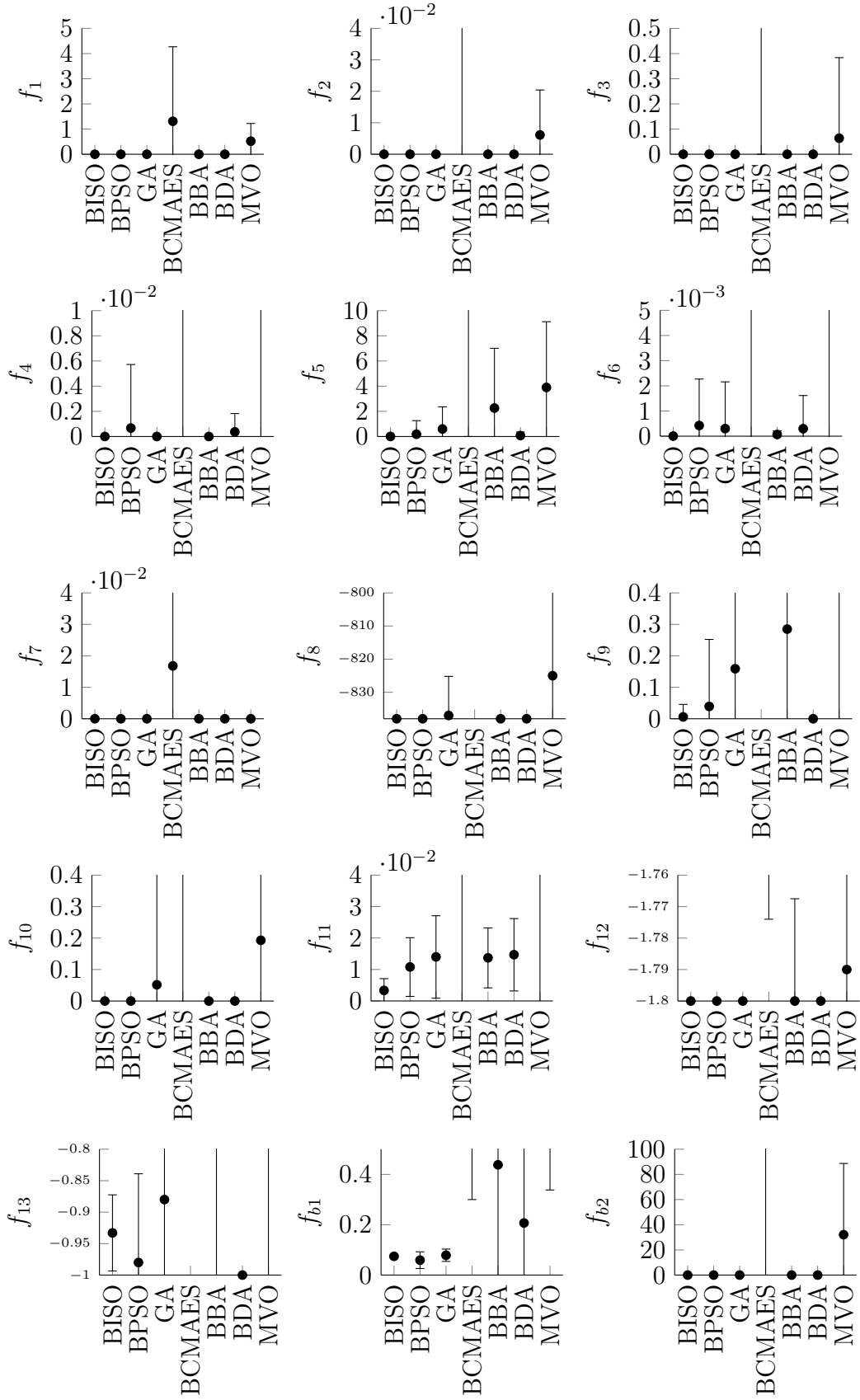
Fig. 4.7: Graphical representation of results for benchmark functions for $Ndim = 30$.
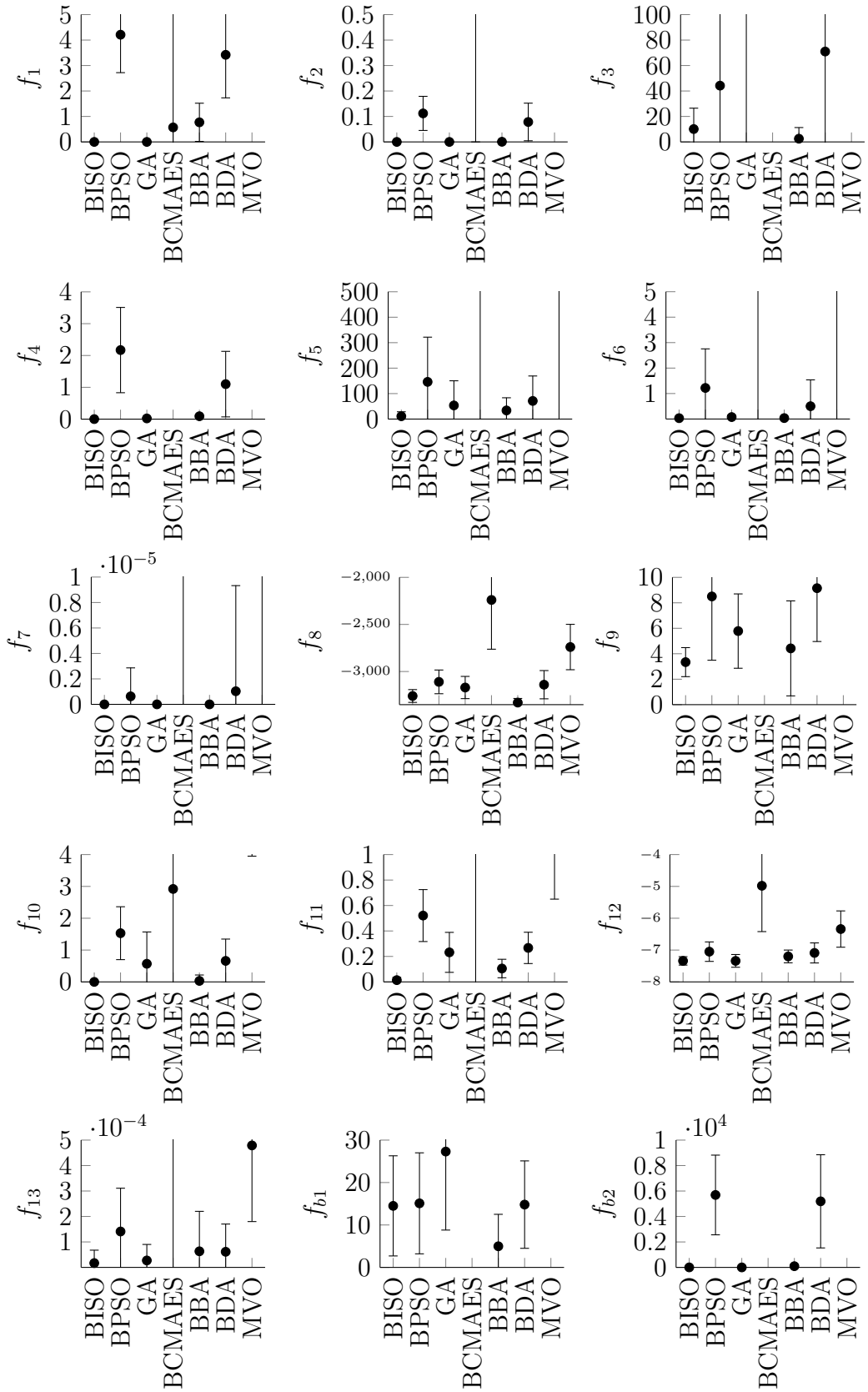
Fig. 4.8: Graphical representation of results for benchmark functions for $Ndim = 120$.
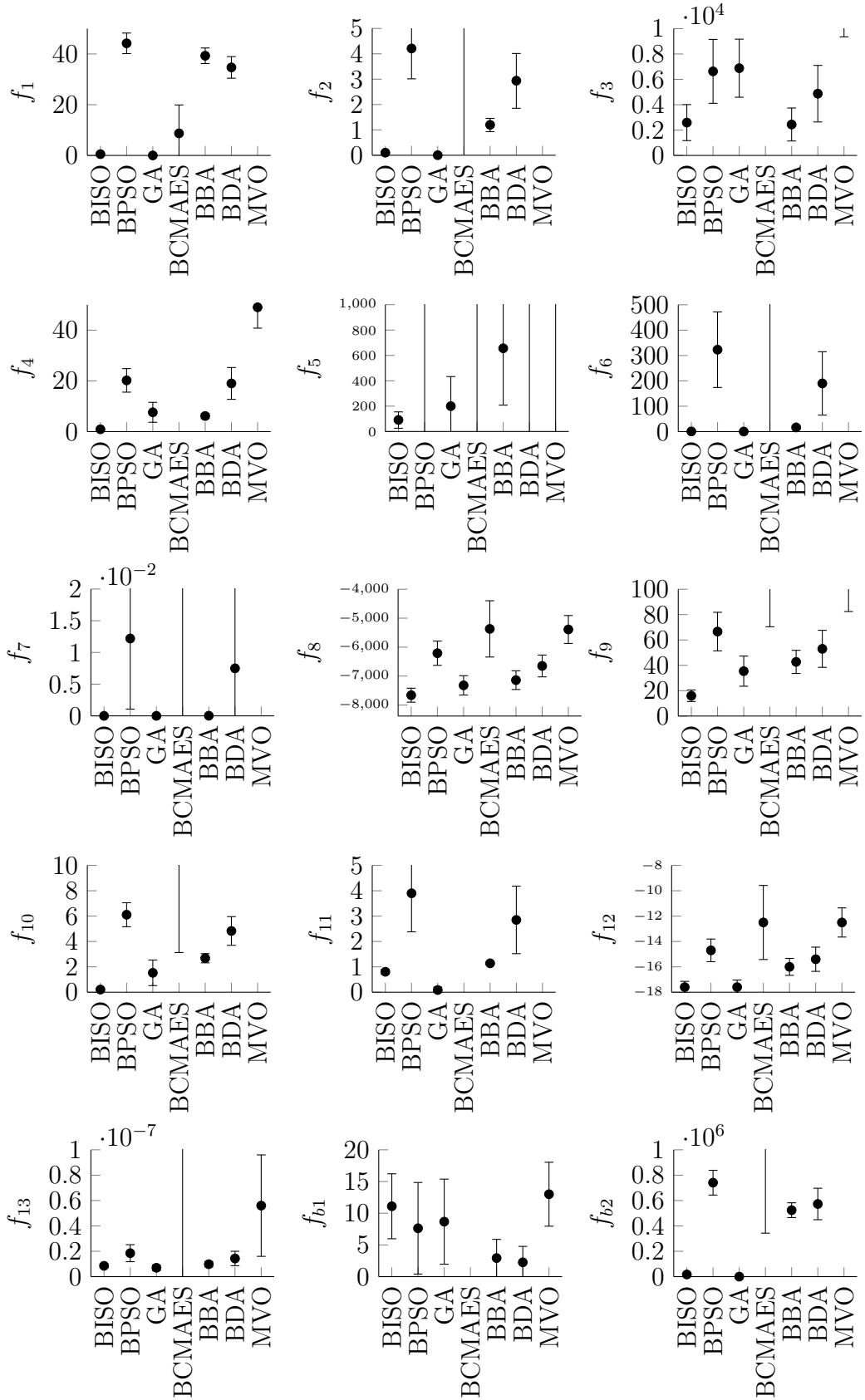
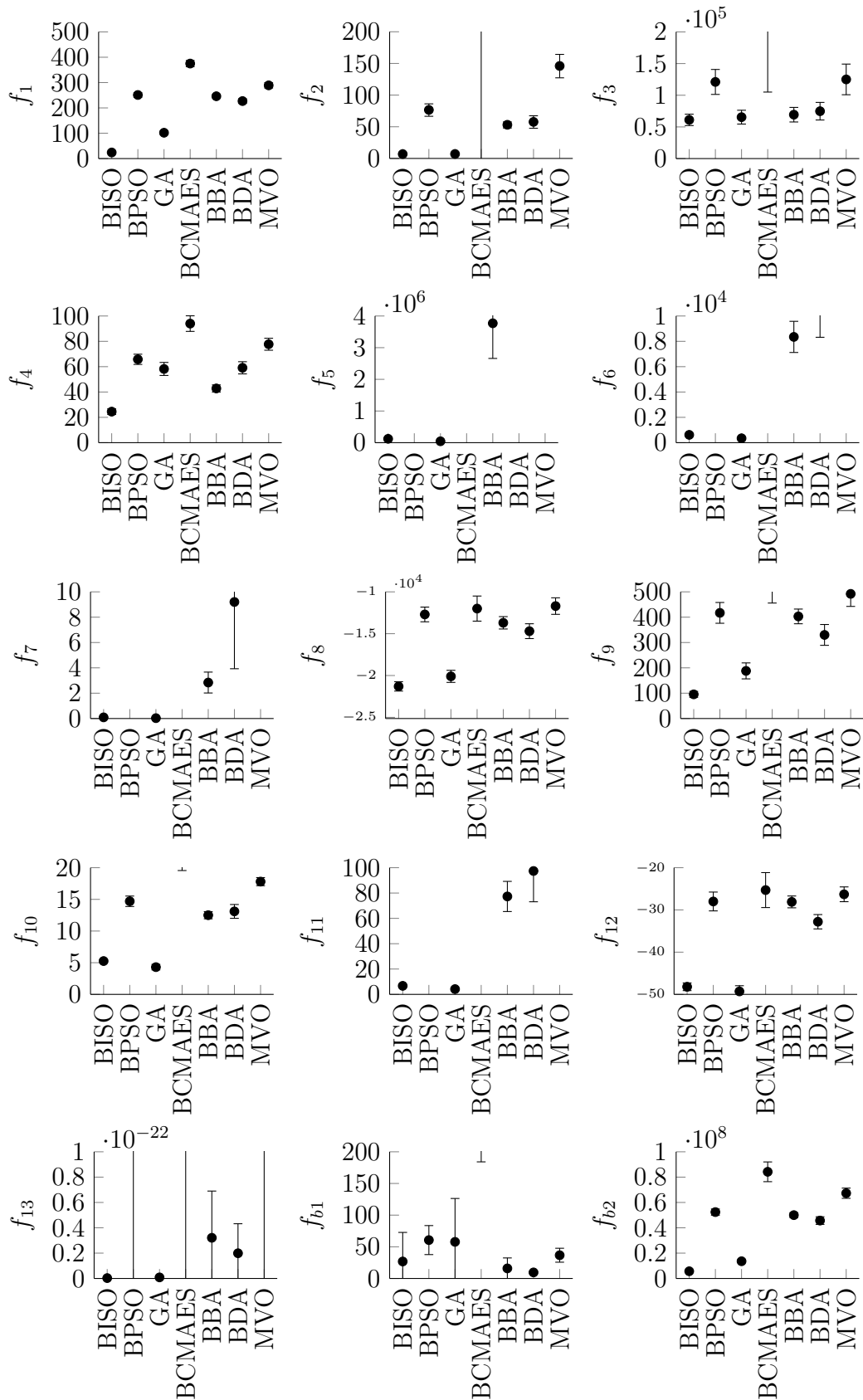Fig. 4.9: Graphical representation of results for benchmark functions for $Ndim = 300$.

Fig. 4.10: Graphical representation of results for benchmark functions for $Ndim = 900$.

4.4 Summary

This chapter introduced a novel heuristic algorithm, the BISO, designed to optimize binary patterns with a unique focus on incorporating the significance of individual bits during optimization. The algorithm's principle, inspired by varying ink saturations of stamps, allows for a probabilistic representation of solutions that dynamically evolves with fitness-based feedback. The detailed steps of the algorithm were described including its initialization, probability matrix formulation, and the reset routine to mitigate premature convergence.

The behavior of BISO was analyzed in relation to its key parameters, such as $minProb$, $minProbRST$, and $rstCoeff$, which significantly influence the balance between exploration and exploitation. Sample runs demonstrated how parameter tuning impacts convergence and highlighted strategies for setting these parameters based on problem complexity and computational constraints.

Finally, benchmark tests on 15 functions showcased BISO's robustness and efficiency compared to six state-of-the-art binary optimization algorithms. The results indicate that BISO consistently performs well across various problem types particularly excelling in high-dimensional and multimodal optimization tasks. This establishes BISO as a competitive and effective method for binary optimization challenges.

Future research may focus on further improving the adaptability and efficiency of the BISO algorithm. Enhancements could include dynamic parameter tuning mechanisms to balance exploration and exploitation during runtime. Exploring hybridization opportunities by combining BISO with other optimization strategies, such as metaheuristics or machine learning, may also lead to significant improvements in performance for complex optimization scenarios.

In the following chapters of this dissertation, the algorithm will be applied in the design of real microwave devices. Specifically, it will be used for the optimization of SIW horn antennas loaded with a pixelated structure where this structure will be optimized using the BISO algorithm to achieve the desired parameters. In Chapter 6, the algorithm will be utilized for the development of an automated procedure for the design of microwave filters. BISO, as a tool for searching the optimal pixel arrangement to meet the required specifications, will form the core of this procedure.

5 Pixelated SIW Horn Antennas

In this chapter, a procedure for the design of pixelated SIW horn antennas based on BISO algorithm is proposed. The procedure is exploited for the design of three pixelated SIW horn antennas with almost equal Half Power Beam Width (HPBW) in principal planes. The first two antennas radiate linearly and circularly polarized wave and are based on two (binary) stage pixelization strategy [JZ64]. On the other hand, the last antenna radiating a circularly polarized wave is based on a four-stage pixelization strategy [JZ72]. Thank to that multistage strategy the designed antenna exhibits better radiation performance and has smaller dimensions than the antenna based on two stage strategy [JZ64]. All three presented antennas are designed for the 24 GHz Industrial, Scientific, and Medical (ISM) band. The results of this chapter are related to the Objective 2 of this thesis.

5.1 Design Procedure Description

This subchapter outlines the proposed procedure for designing pixelated SIW horn antennas. The procedure can be divided into the following main steps:

- **Base SIW Horn Antenna Definition**

First, a base SIW horn antenna is defined. This antenna should meet the required dimensional and operational frequency specifications. The initial dimensions can be obtained using design graphs for conventional H-plane sectoral horn antennas [73] or through a simple parametric sweep using numerical simulations. While it is advantageous to start with a design that achieves maximum directivity within the specified size constraints this is not strictly necessary.

- **Definition of Pixelization Strategy**

Next, the pixelization strategy is defined. The pixel structure in the form of a dielectric load can be placed in front of the antenna aperture. A rectangular shape can be described by a binary matrix based on the chosen dimensions of the individual pixels and the overall dimensions of the pixel structure. A more advanced approach involves embedding a nested pixel structure within the antenna funnel as demonstrated in the designs presented later in this chapter. At this stage, the manufacturing process should also be considered. For example, 3D printing allows complex pixel shapes whereas conventional fabrication techniques typically limit pixels to circular holes.

- **Fitness Function Definition**

A fitness function based on the Euclidean distance in terms of the observed antenna parameters from an ideal solution is then established. This ideal solution reflects the desired antenna performance—such as a target radiation pattern, gain,

sidelobe level, etc. Each contributing metric is assigned a weight and deviations are penalized proportionally in the fitness score.

- **Optimization Process**

During the optimization process, each design candidate is evaluated using full-wave numerical simulation to extract its characteristics. To reduce computation time, the SIW structure can be simplified by replacing vias with continuous vertical metallic walls which approximate the wave confinement behavior with significantly fewer mesh elements. Applying symmetry planes during the analysis can also help significantly.

- **Antenna Finalization**

After the optimization, the best-performing pixel configuration is translated into a complete SIW horn structure. This includes reconstructing the SIW sidewalls using metallized via holes and ensuring compatibility with the chosen fabrication process. The input transition to the SIW must also be addressed which may involve a microstrip-to-SIW taper, coaxial probe, or a waveguide port depending on the application and signal source.

The following subchapters demonstrate the application of this procedure to the design of three pixelated SIW horn antennas with equal HPBW in the principal planes. While this requirement is relatively uncommon for this class of antennas, as highlighted in the state-of-the-art chapter, the versatility of the BISO algorithm allows it to effectively address such design constraints.

5.2 Pixelated LP SIW Horn Antenna

In this subchapter, the BISO algorithm is utilized to design a Linearly Polarized (LP) SIW horn antenna with nearly equal beamwidths for the 24 GHz ISM frequency band. A conventional SIW horn antenna is employed to achieve this objective. The dimensions of the antenna are optimized for maximal directivity. The antenna is depicted in Fig. 5.1a. The normalized radiation patterns of the simplified version (where the vias are replaced with solid walls) of the SIW horn antenna are shown in Fig. 5.1b. The E- and H-plane beamwidths of the antenna are 138.6° and 25.6°, respectively. The antenna provides a gain of 8.2 dBi (please note that the losses of the substrate were not considered). The antenna is designed for a substrate with a thickness of 3.3 mm and a relative permittivity of 2.75.

The pixelated LP SIW horn antenna is designed to achieve equal HPBW in the E- and H-planes of the radiation pattern with an emphasis on Side Lobes Level (SLL) reduction. The antenna is axially symmetrical, as shown in Fig. 5.2. The pixelization is applied over a grid intersected with the body of the antenna. Cells assigned with
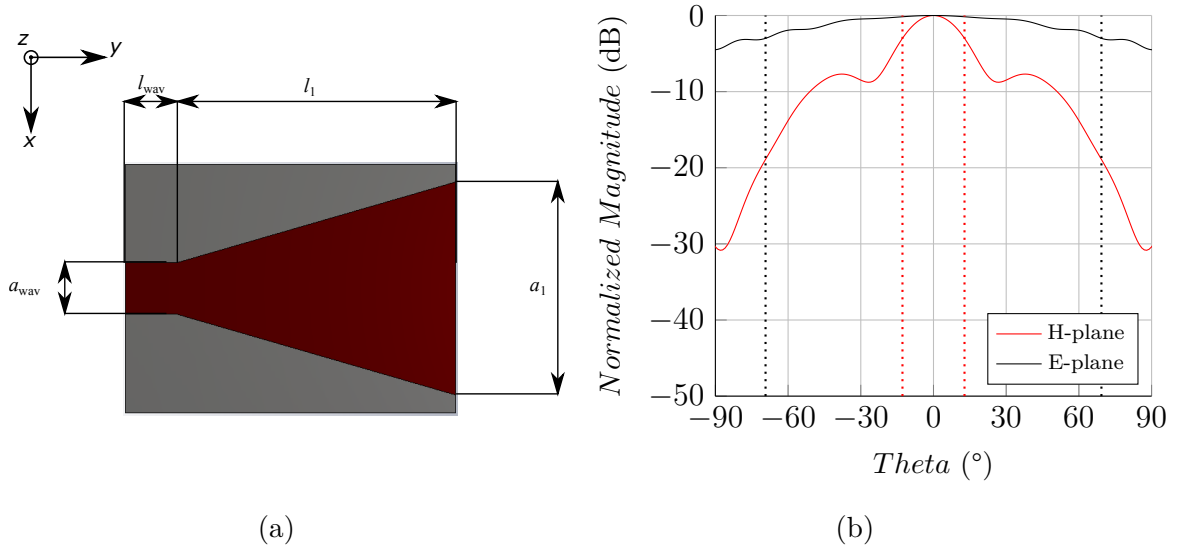
Fig. 5.1: (a) A simplified model of conventional SIW horn antenna, where vertical solid walls are used instead of vias ($a_1 = 24$ mm, $a_{\text{wav}} = 5.8$ mm, $l_1 = 31.5$ mm, $l_{\text{wav}} = 5.8$ mm). (b) Normalized simulated radiation patterns of the simplified SIW horn antenna at 24 GHz. HPBW is indicated by vertical dotted lines.

"1" are filled with substrate material, and cells with "0" are filled with air. The pixel grid geometry is controlled using parameters l_{c1}-l_{c6}, which are integer multiples of the side length of the pixels and therefore refer to the number of pixels in the columns. Bits of the optimized pattern that are outside the grid become so-called dummy pixels because these positions are defined as filled with the substrate material and covered by a metal layer. After several trials, it was observed that the shape of the grid can be roughly approximated with a parabolic shape; therefore, some of the pixels are allocated to determine the parameters l_{c1}-l_{c7} (these pixels are highlighted in blue in Fig. 5.4a). This approach helps to reduce the number of pixels. The variable l_{c7} is used to determine the length of the edge metallization.

The total number of pixels in the optimized pattern is 6×28. The fitness function is defined as the Euclidean distance from the optimal solution using normalized components. The fitness function f is specified as follows:

$$f = \sqrt{f_{S11}{}^2 + f_{HPBW}{}^2 + f_{SLL}{}^2 + f_G{}^2}, \tag{5.1}$$

where f_{S11}, f_{HPBW}, f_{SLL}, and f_G are the normalized components corresponding to all considered antenna parameters. All components (except f_{HPBW}) are defined within the range of 0 to 1. A value of 1 indicates that the parameter meets only the minimum required value or worse while a value of 0 means that the parameter meets or exceeds an excellent threshold chosen to be marginally realistic for the given configuration.

47

The reflection coefficient component f_{S11} is defined to have a value of zero when the reflection coefficient is -15 dB. For any higher (i.e., worse) value the component increases above zero. The f_{HPBW} component, representing the difference between HPBW in the E- and H-planes, is defined as the HPBW difference divided by 10. As a result, this component can exceed 1 and therefore has the most significant impact on the overall fitness.

For the SLL component f_{SLL}, the approximate maximum achievable value was first estimated to be 14 dBi. Based on this, two threshold values are chosen: 8 dBi (the minimum acceptable value for design) and 20 dBi (providing margin in case the maximum estimate was too low). The component value is then calculated as a linear function between these thresholds. Any SLL less than 8 dBi is rated as 1, and any greater than 20 dBi is rated as 0.

The gain component f_G is defined analogously. The estimated maximum gain was 11.5 dBi, with a lower limit of 8 dBi and an upper limit of 15 dBi.
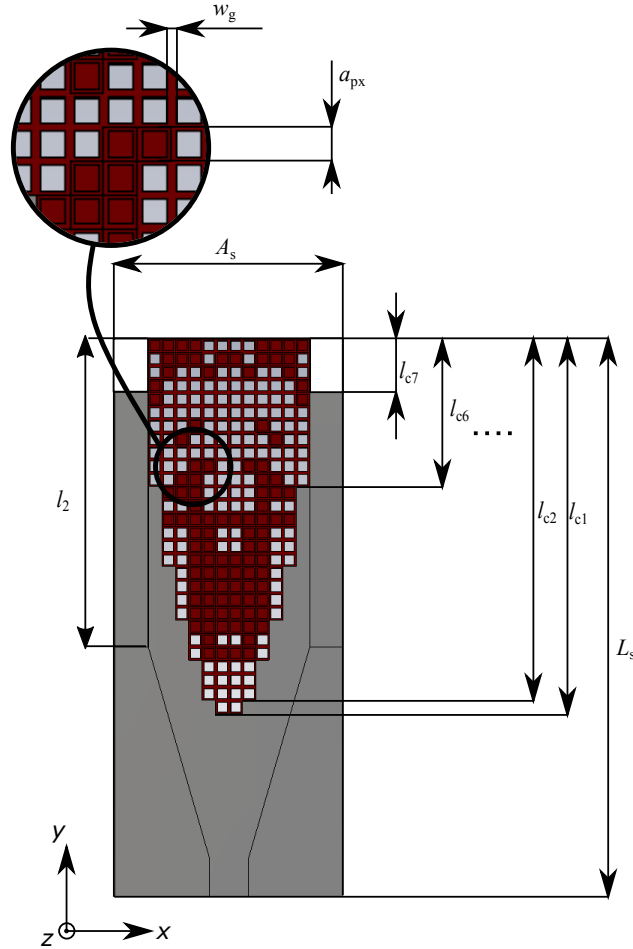
Fig. 5.2: Simplified model of the proposed pixelated LP SIW horn antenna.

Parameter	Value	Parameter	Value
$Nelit$	5	$minProb$	0.01
$Niter$	250	$minProbRST$	0.5
$Npop$	25	$sigCoeff$	10
		$rstCoeff$	0.01

Tab. 5.1: Parameter settings for BISO algorithm during the optimization of pixelated LP SIW horn antenna.

The components are defined by the following equations:

$$f_{S11} = \begin{cases} \frac{S11}{15} + 1 & \text{if } S11 \geq -15 \\ 0 & \text{if } S11 < -15 \end{cases}, \tag{5.2}$$

$$f_{HPBW} = \frac{\Delta_{HPBW}}{10}, \tag{5.3}$$

$$f_{SLL} = \begin{cases} 1 & \text{if } SLL < 8 \\ -\frac{SLL}{12} + \frac{5}{3} & \text{if } 8 \leq SLL \leq 20 \\ 0 & \text{if } SLL > 20 \end{cases}, \tag{5.4}$$

and

$$f_{G} = \begin{cases} 1 & \text{if } G < 8 \\ -\frac{G}{7} + \frac{15}{7} & \text{if } 8 \leq G \leq 15 \\ 0 & \text{if } G > 15 \end{cases}, \tag{5.5}$$

where $S11$ is the reflection coefficient at 24.125 GHz in dB, Δ_{HPBW} is the difference between HPBW in the E- and H-planes at 24.125 GHz in degrees, SLL is the SLL at 24.125 GHz in dB, and G is the gain in the main direction at 24.125 GHz in dBi.

The settings of the BISO algorithm, as well as the antenna model for optimization, were determined through several trial runs. The parameters of the BISO algorithm during the optimization were set as shown in Tab. 5.1. The parameters were adjusted to achieve a tradeoff between the algorithm's ability to explore and exploit the search space. After this tuning process, four independent runs with the same settings were conducted. To obtain the parameters of individuals, the electromagnetic simulations were performed using CST Studio Suite. For the sake of the speed of the design process, a simplified model of the SIW horn antenna with vertical solid walls was utilized. The optimization process was controlled by an in-house MATLAB code. An example of an optimization run is shown in Fig. 5.3. This figure illustrates the best individuals from three independent generations, along with the probability matrix that governs the generation of the next population (the black corresponds to the highest probability of generating "1", and the white corresponds to the highest probability of generating "0"). The first sample is from generation #106 which occurs

immediately after the reset routine. It can be seen in the radiation pattern, the antenna exhibits relatively high sidelobe levels. Additionally, the probability matrix indicates that the next generation will be formed with a relatively high degree of randomness. After twenty more generations, the antenna exhibits a more directive radiation pattern. A distinct scheme begins to emerge in the probability matrix particularly in the region defining the shape of the pixelated grid (see the lower right corner of the probability matrix). The best individual from generation #210 is shown at the upper right corner. The antenna demonstrates an excellent directional characteristic. Furthermore, the probability matrix reveals that the algorithm is intensively exploring a very limited region of the state space as very few positions in the matrix remain undecided.

The optimized pixelated pattern is shown in Fig. 5.4a. The simplified model was transformed into the SIW structure, and the coaxial-SIW transition was added (Fig. 5.4b). Dimensions of the optimized model are listed in Tab. 5.2. Note that the coaxial feed probe length in the substrate l_{in} is 1.8 mm. Values in parentheses
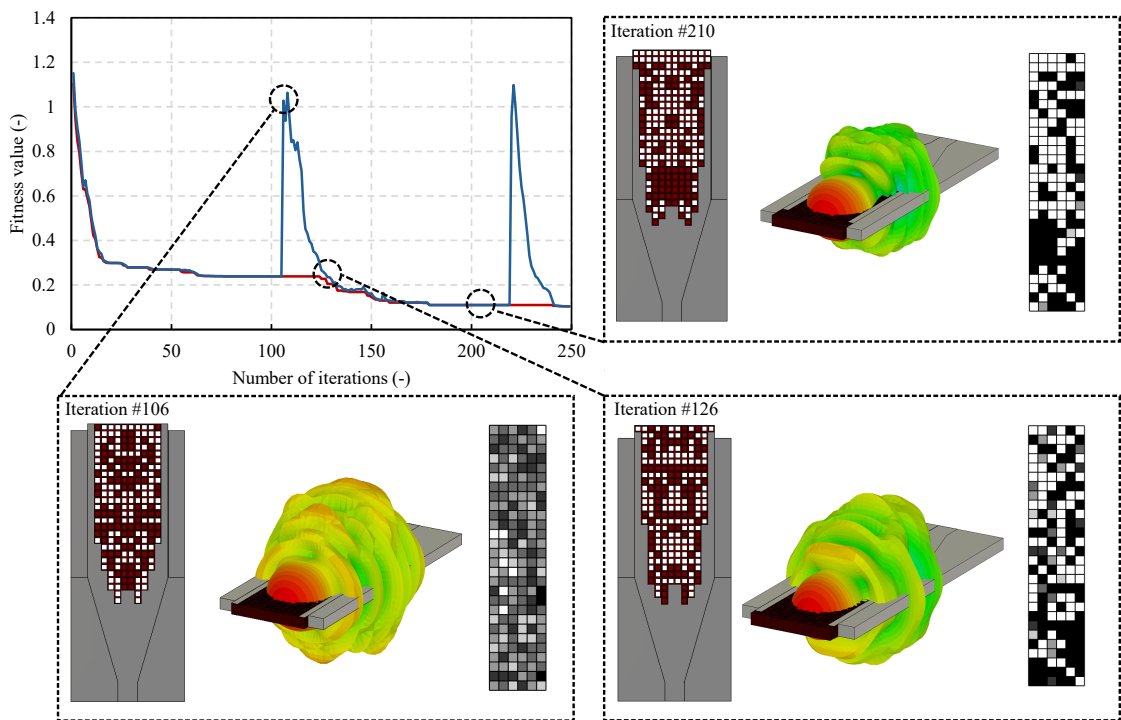
Fig. 5.3: Example of convergence curve from an optimization run for LP antenna with pixelated load. Red line represents fitness function value of the best individual so far while blue line represents mean fitness value of elite group. For three selected generations, best individual and probability matrix used for forming next generation are shown.

represent the optimal lengths found for l_{c1}-l_{c7}. The E-field distributions at the center frequency of the 24 GHz ISM band are shown in Fig. 5.4c. Obviously, the E-field is focused by the pixelated part.

To verify experimentally the optimized antenna, its dielectric part antenna was made of an XT co-polyester from Colofabb [60] using a FDM 3D printer Prusa i3 MK3S with a 0.25 mm nozzle. The dielectric part was fully printed without any post-processing steps such as drilling, grinding, etc. The top and bottom metal

      (a)   (b)   (c)
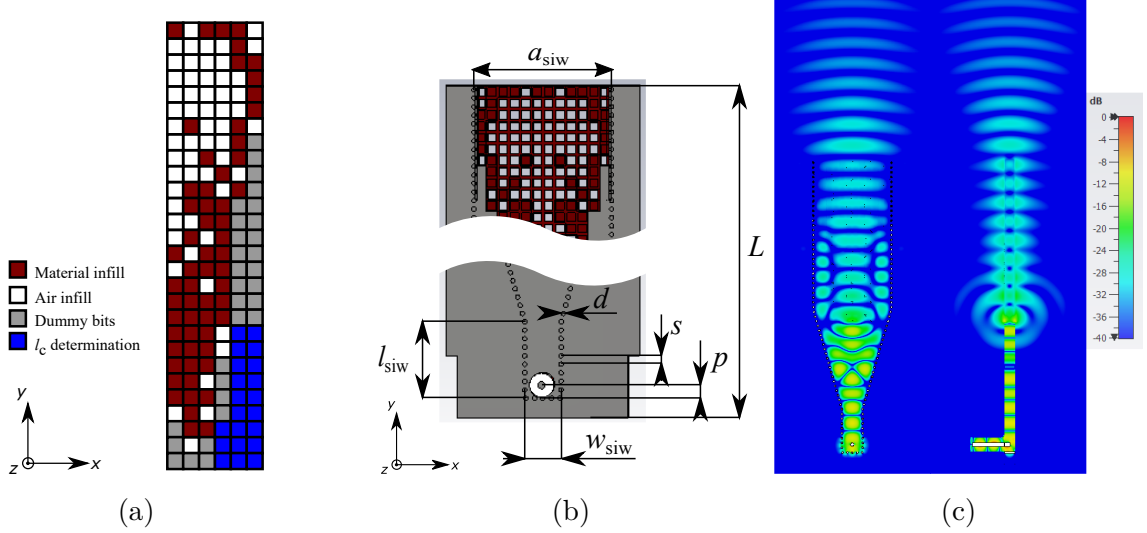
Fig. 5.4: (a) Optimized binary pattern for the pixelated LP SIW horn antenna. (b) Optimized linearly polarized antenna with SIW structure and coaxial-SIW transition.(c) Normalized E-field distribution of the pixelated LP SIW horn antenna at 24.125GHz in H-plane (left) and E-plane (right).

Parameter	mm	Parameter	mm
a_{px}	2	l_{c5}	22-36 (22)
A_s	34	l_{c6}	0-14 (14)
a_{siw}	24.2	l_{c7}	0-14 (0)
d	0.8	l_{in}	1.8
L	94.3	L_s	83.3
l_2	46	l_{siw}	13.5
l_{c1}	42-56 (50)	p	2.5
l_{c2}	42-56 (54)	s	1.5
l_{c3}	42-56 (52)	w_g	0.5
l_{c4}	36-50 (42)	w_{siw}	6.4

Tab. 5.2: Parameters of the proposed pixelated LP SIW horn antenna.

layers were made of copper foil and their optimized shape was cut. The vias of the SIW structure were created by a copper wire with a diameter of 0.8 mm. The individual vias were soldered to the top and bottom metal layers of the antenna, and the SMA connector was soldered.

The manufactured LP antenna (Fig. 5.5a) was measured in an anechoic chamber to experimentally verify its performance. The comparison of the measured and simulated reflection coefficient over the frequency band 22-26 GHz is shown in Fig. 5.5b. The measured reflection coefficient of the proposed antenna is below -18 dB in the whole 24 GHz ISM band. The measured radiation patterns (Fig. 5.6) show good agreement with the simulated ones. A small discrepancy between the measured and simulated results is caused by the inaccuracy of the fabrication technology and further by the fact that losses of the substrate were not considered during the design process of the antenna. The measured gain of the antenna is 14.2 dBi at the central frequency of the 24 GHz ISM band, the SLL is below -15 dB, E- and H-plane beamwidths are 26.5°and 25°, respectively. The nearly equal HPBW in the E- and H-plane is achieved for the single-layer configuration of the antenna.

Compared to the state-of-the-art works listed in Tab. 5.3, the proposed antenna stands out with its single-layer design, which simplifies fabrication and minimizes overall dimensions. It provides a competitive gain of 14.2 dBi, and the achieved low sidelobe level is comparable to other state-of-the-art designs, ensuring a well-defined radiation pattern. Overall, the proposed antenna offers a trade-off between simplicity, high gain, and directional performance with nearly equal HPBW in principal

<div align="center">(a)   (b)</div>
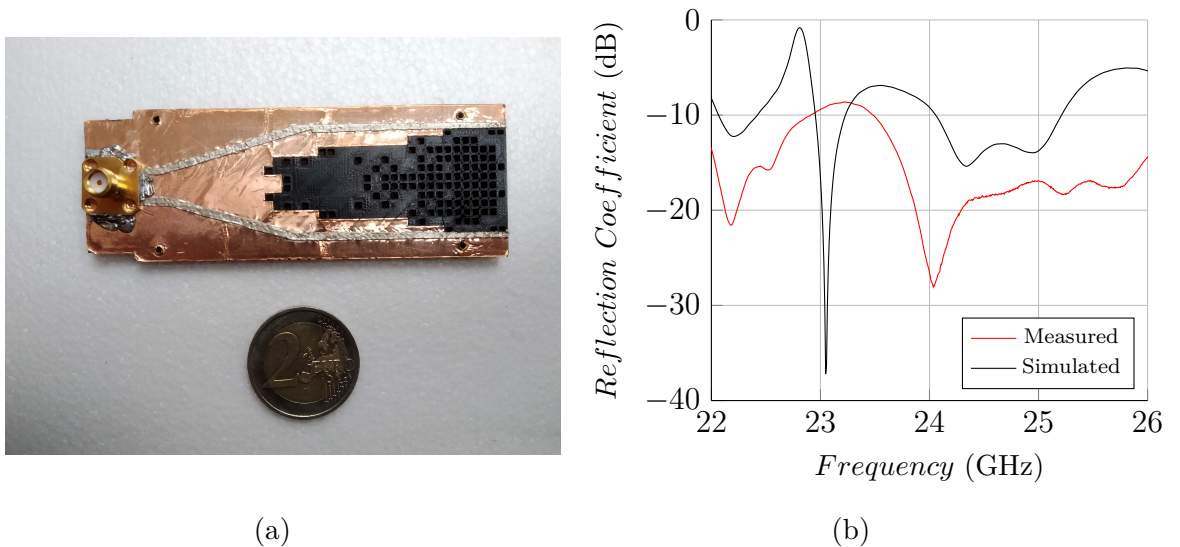
Fig. 5.5: (a) Manufactured prototype of the pixelated LP SIW horn antenna. (b) Measured and simulated reflection coefficient of the pixelated LP SIW horn antenna.

planes making it a strong alternative to more complex multi-layer antennas. In this scope, the proposed antenna outperforms the state-of-the-art works. Note that the SMA connector used for the antenna feeding is rated up to 26.5 GHz which is sufficient considering the fact that the antenna is designed for the 24 GHz ISM band. However, the measured impedance BW for the reflection coefficient lower than -10 dB cannot be considered valid because it is beyond the connector's operating range. Consequently, the presented values of -10 dB S11 BW are according to the simulated data.

(a)   (b)
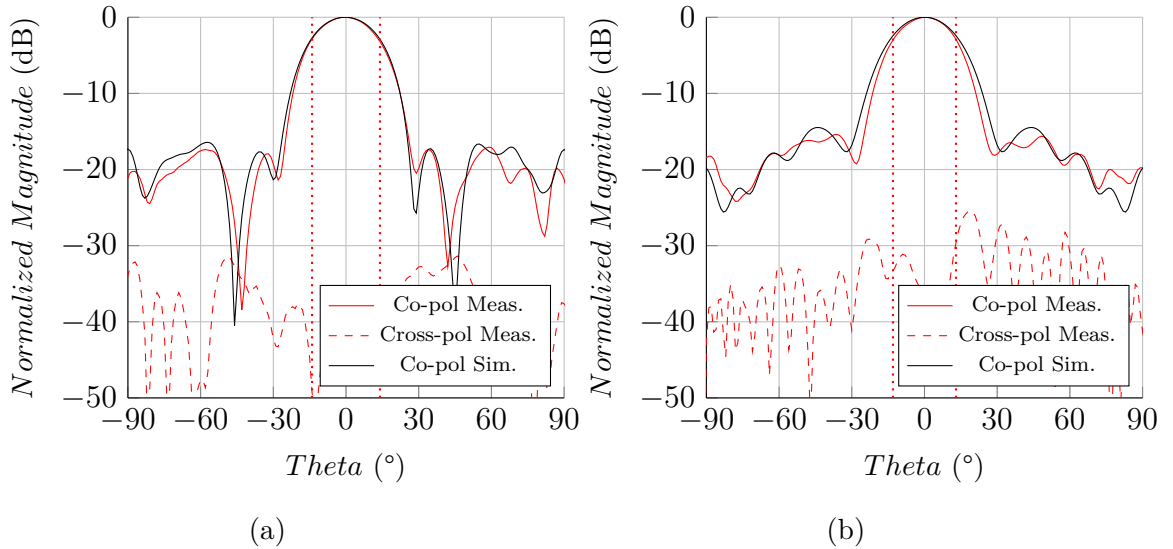
Fig. 5.6: Normalized measured and simulated radiation patterns of the pixelated LP SIW horn antenna at 24.125 GHz in (a) E-plane and (b) H-plane. Vertical dotted lines indicate measured HPBW.

Ref	Number of layers	Dimensions (λ_0)	Frequency (GHz)	-10 dB S11 BW (%)	Gain (dBi)	SLL (dB)	HPBW (°) H-plane/ E-plane
[74]	1	$(5.62 \times 1.68 \times 0.23)$	22	41	14.7	-15	25.8/34.7
[75]	1	$(4.92 \times 1.49 \times 0.26)$	24.15	13.7	15.4	-14.5	27/35
[76]	8	$(9.22 \times 2 \times 1.5)$	35.1	3	13.1	-24	33/33
[25]	7	$(5.6 \times 3.9 \times 2.5)$	32.78	69.7	10.2	-10	20/20
This work	1	$(7.66 \times 2.72 \times 0.27)$	24.125	4.9*	14.2	-15	25/26.5

*Presented -10 dB S11 BW is according to simulated data.

Tab. 5.3: Comparison of the proposed pixelated LP SIW horn antenna with state-of-the-art works.

5.3   Pixelated CP SIW Horn Antennas

In this subchapter, BISO algorithm is used to design two circularly polarized SIW horn antennas with nearly equal beamwidths in principal planes. Compared to the design procedure of the LP SIW horn antenna presented in the previous subchapter, the design procedure of the circularly polarized antennas differs in its topology. The difference lies in the configuration of the top and bottom metal layers. In this case, the layers are antipodal. The antenna with the antipodal structure is inspired by [77] where the ability of the antipodal structure to generate Circularly Polarized (CP) wave is presented. Two prototypes of antennas are presented in this subchapter. The first antenna using binary pixelization, as in the case of the LP antenna, and the second antenna is proposed using a four-state pixelization. Both antennas were also made of XT co-polyester material with a relative permittivity of 2.75 using the 3D printer Prusa i3 MK3S with a 0.25 mm nozzle.

5.3.1   CP Antenna with Binary Pixelated Load

The simplified antenna model used for the optimization is shown in Fig. 5.7. The pixel grid geometry is controlled using parameters $l_{c7} - l_{c13}$ which determine the number of pixels in the columns along with parameters $l_{c1} - l_{c6}$ that define the remaining adjusted part of the metal layer. The pixels corresponding to parameters $l_{c1} - l_{c13}$ are highlighted in blue in Fig. 5.9a.

The total number of pixels for the optimized pattern is 6×28. The parameters for the BISO algorithm were set as in the case of the LP antenna (Tab. 5.1). The fitness function f is defined similarly to the previous case. The main difference is the inclusion of a component for the axial ratio of the antenna instead of a component for side lobe suppression. The fitness function is defined as the Euclidean distance of the normalized components:

$$f = \sqrt{f_{S11}{}^2 + f_{HPBW}{}^2 + f_{AR}{}^2 + f_G{}^2},\tag{5.6}$$

where f_{S11} and f_{HPBW} are defined same as for the LP antenna:

$$f_{S11} = \begin{cases} \frac{S11}{15} + 1 & \text{if } S11 \geq -15, \\ 0 & \text{if } S11 < -15, \end{cases}\tag{5.7}$$

and

$$f_{HPBW} = \frac{\Delta_{HPBW}}{10},\tag{5.8}$$

where $S11$ is the reflection coefficient at 24.125 GHz in dB, and Δ_{HPBW} is the difference between the HPBW in the principal planes at 24.125 GHz in degrees. Components for the Axial Ratio (AR) and gain are defined as a linear dependency

between two threshold values. The threshodls for AR component f_{AR} are 10 dB ($f_{AR} = 1$) and 3 dB ($f_{AR} = 0$). Consequently, the normalized component for the axial ratio f_{AR} is defined as:

$$f_{AR} = \begin{cases} 1 & \text{if } AR > 10, \\ \frac{AR}{7} - \frac{3}{7} & \text{if } 3 \leq AR \leq 10, \\ 0 & \text{if } AR < 3, \end{cases} \tag{5.9}$$

Fig. 5.7: Simplified model of the binary pixelated CP SIW horn antenna.

where AR is the axial ratio in the main direction at 24.125 GHz, in dB. The expected gain for this design is 10.5 dBi and the thresholds are 8 dBi (f_G=1) and 13 dBi (f_G=0). The f_G is defined as:

$$f_G = \begin{cases} 1 & \text{if } G < 8, \\ -\frac{G}{5} + \frac{13}{5} & \text{if } 8 \leq G \leq 13, \\ 0 & \text{if } G > 13, \end{cases} \tag{5.10}$$

where G is the gain in the main direction at 24.125 GHz in dBi.

The assumption was that the behavior of the optimization (mainly due to the assumed parameter settings and the same number of pixels in the optimized matrix) would be similar to the optimization of the LP antenna. Similarly, four independent runs of the algorithm were performed, and the best variant was selected for the prototype relay. An example of a run of the algorithm is shown in Fig. 5.8. It can be seen, the algorithm tends to get stuck in a local minimum. This is mainly due to the large number of dummy pixels which makes it quite difficult to meet the conditions
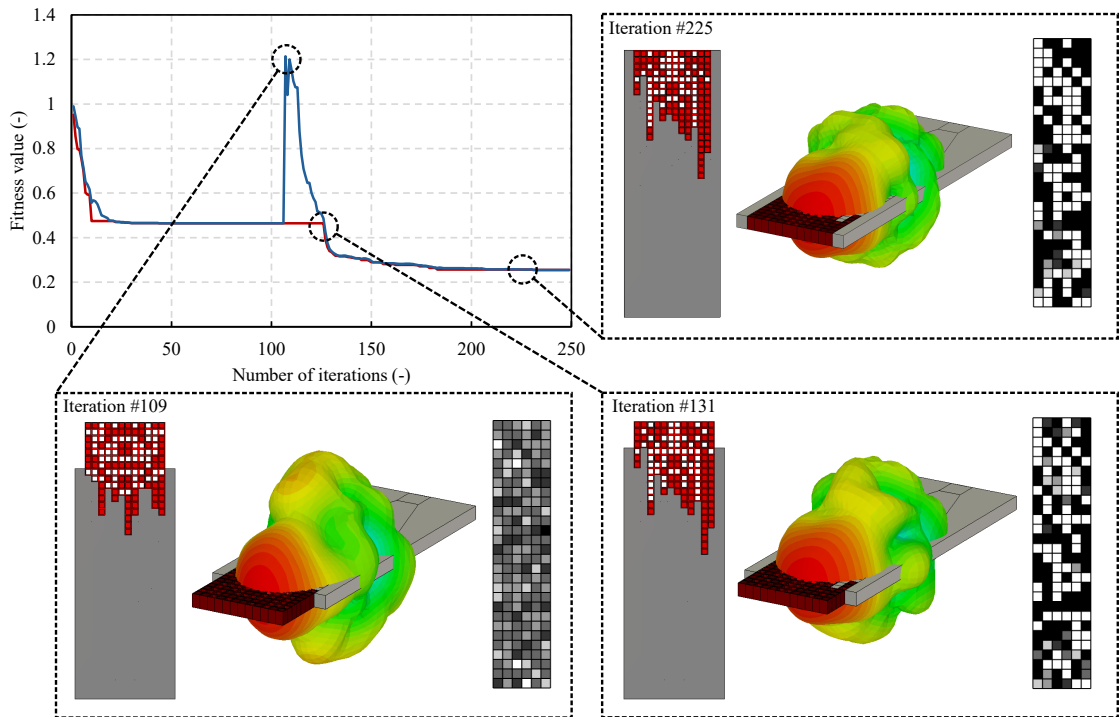
Fig. 5.8: Example of convergence curve from optimization run for CP antenna with binary pixelated load. Red line represents fitness function value of the best individual so far while blue line represents mean fitness value of elite group. For three selected generations, best individual and probability matrix used for forming next generation are shown.

for the reset routine. The best individuals of the three selected generations are shown. Generation #109 was the first generation after the reset routine. It can be seen that this individual has relatively poor radiation characteristics, and the probability matrix shows that the next generation will be generated with a relatively high degree of randomness. Comparing the next two individuals (generations #131 and #225) again shows that the first step of the algorithm was to find a suitable plating shape and then to determine the best configuration for the pixelated part. It can also be seen from the probability matrix for generation #225 that even though the algorithm has already converged to a very narrow subspace, there are still a non-negligible number of "undecided" pixels. This is mainly due to the larger number of dummy pixels.

The optimized pattern is shown in Fig. 5.9a, and the dimensions of the proposed CP antenna are listed in Tab. 5.4. Values in parentheses denote the found optimal lengths for the parameters $l_{c1} - l_{c13}$. The simplified model of the CP antenna was also transformed into the SIW structure, and the coaxial-SIW transition was added (Fig. 5.9b). The length of the feeding coaxial probe in the substrate l_{in} is 1.8 mm. The E-field distribution of the proposed CP antenna is shown in Fig. 5.9c. The CP antenna provides a less uniform E-field at the aperture compared to the LP antenna.

The antenna was manufactured in the same way as the LP antenna presented in the previous subchapter using co-polyester 3D-printed material and copper foil. The fabricated prototype of the antenna is shown in Fig. 5.10.

Parameter	mm	Parameter	mm
a_{px}	2	lc_8	12-26 (22)
A_s	30	lc_9	8-22 (22)
a_{siw}	25.1	lc_{10}	6-20 (20)
d	0.8	lc_{11}	4-18 (8)
L	94.3	lc_{12}	0-14 (14)
l_2	46	lc_{13}	0-14 (6)
lc_1	32-46 (34)	l_{in}	1.8
lc_2	30-44 (32)	L_s	83.3
lc_3	26-40 (28)	l_{siw}	13.5
lc_4	24-38 (26)	p	2.5
lc_5	20-34 (30)	s	1.5
lc_6	18-32 (28)	w_g	0.5
lc_7	14-28 (20)	w_{siw}	6.4

Tab. 5.4: Parameters of the proposed binary pixelated CP SIW horn antenna.

The measured and simulated reflection coefficient over the frequency band 22-26 GHz is shown in Fig. 5.11a. The measured reflection coefficient remains below -12 dB for the entire 24 GHz ISM band. The measured and simulated axial ratio (Fig. 5.11b) are below 3 dB over the operating band. The measured radiation patterns (Fig. 5.12) in the principal planes are in good agreement with the simulated ones. The antenna radiates the Right-Handed Circularly Polarized (RHCP) wave. As in the case of the LP antenna, a small discrepancy between the measured and simulated results is caused by the inaccuracy of the fabrication technology. The measured RHCP gain of the antenna is 8.9 dBi at the center frequency of the 24 GHz ISM band. The measured HPBW in the principal planes are 33.4°and 30.6°.

(a) (b) (c)
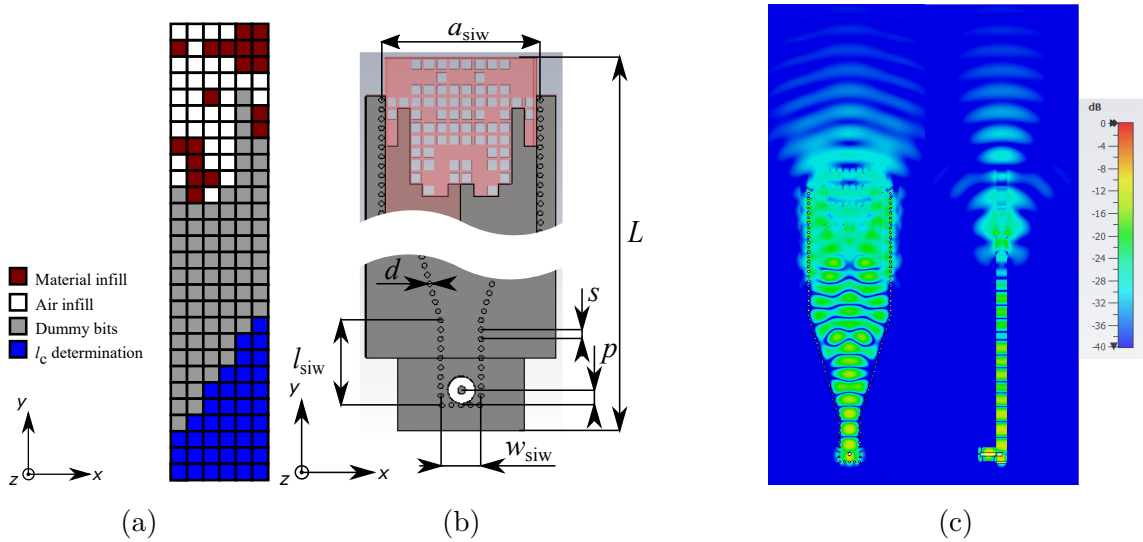
Fig. 5.9: (a) Optimized binary pattern for the binary pixelated CP SIW horn antenna. (b) Optimized binary pixelated CP antenna with SIW structure and coaxial-SIW transition. (c) Normalized E-field distribution of the binary pixelated CP SIW horn antenna at 24.125 GHz in xy plane (left) and yz plane (right).
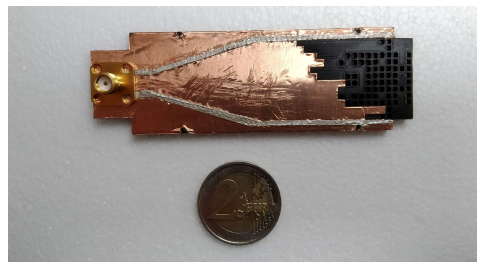
Fig. 5.10: Manufactured prototype of the binary pixelated CP SIW horn antenna.
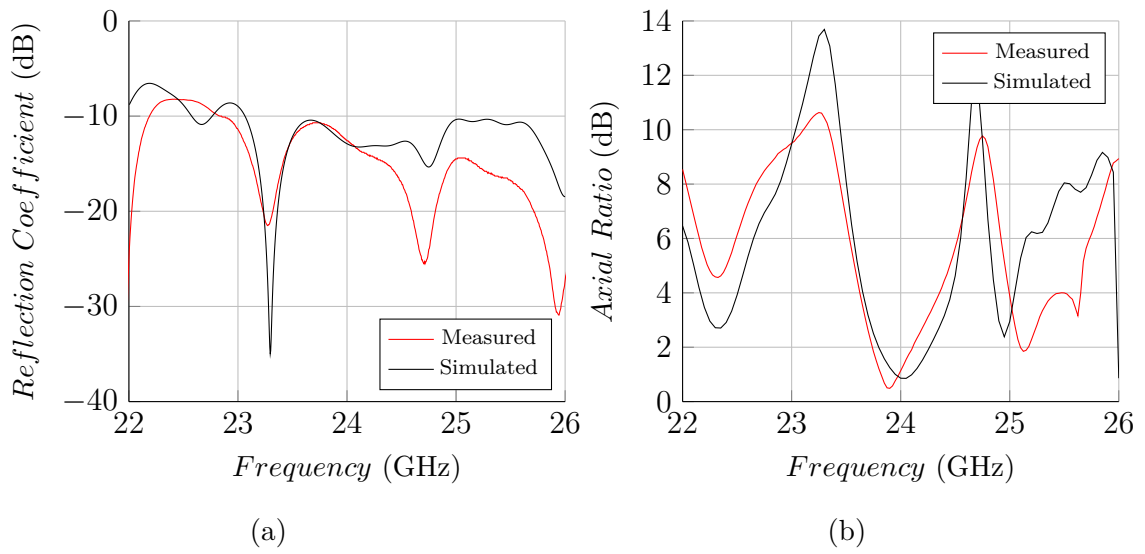
Fig. 5.11: Measured and simulated reflection coefficient (a) and axial ratio (b) of the binary pixelated CP SIW horn antenna.
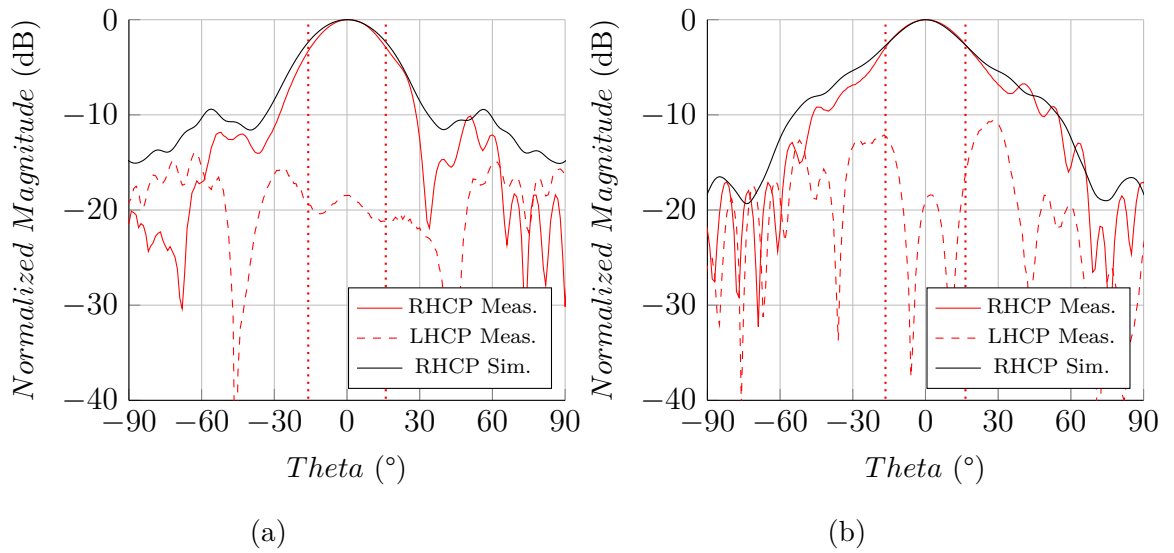
Fig. 5.12: Normalized measured and simulated radiation pattern of the binary pixelated CP SIW horn antenna at 24.125 GHz: (a) yz plane and (b) xy plane. Measured HPBW is indicated by vertical dotted lines.

5.3.2   CP Antenna with Multistate Pixelated Load

The optimization process of the previous antenna resulted in a relatively high number of dummy pixels (Fig. 5.9a). Therefore, during the design of the second CP antenna, the focus was on efficiently defining the optimized matrix. Furthermore, in the optimization of the previous antenna, the gain and axial ratio were evaluated at only one frequency point. As a result, the antenna may be narrowband in terms of these parameters meaning that even a small frequency deviation could lead to a significant degradation of the realized antenna parameters. To address this issue, the fitness function in the second CP antenna's optimization is modified to account for a wider frequency range.

The CP antenna based on multistate pixelization has a topology similar to the previous CP antenna based on binary pixelization. The main difference is obvious: four-state pixelization instead of the binary approach (Fig. 5.13a). The four-state pixelization is achieved by splitting the optimized binary matrix into Most Significant Bit (MSB) and Least Significant Bit (LSB) parts (Fig. 5.13b). Each pixel is then defined by 2 bits and, therefore, can take on 4 states. Every single pixel can be represented as being filled with the substrate material or as a hole with a diameter of 0.6 mm, 1 mm, or 1.6 mm.

The CP antenna based on multistate pixelization is also designed to radiate an RHCP wave with equal HPBW in the principal planes. The observed parameters included the reflection coefficient over the desired frequency band, AR, and the maximum gain at the center of the 24 GHz ISM band. Additionally, the 3 dB AR BW and the min-to-max gain ratio in the vicinity of the operating band are considered. The model for the optimization procedure is depicted in Fig. 5.13a. The size of the optimized binary matrix is 6×26. As in the case of the previous antenna, some bits are allocated to determine parameters $l_1 - l_{13}$ and l_{cone}. These bits are highlighted in blue in Fig. 5.14a. Based on the experience with the optimization of binary pixelated antennas presented in the previous subchapters, the BISO algorithm settings are modified. The parameters for the BISO algorithm are given in Tab. 5.5. The first difference is the number of individuals per generation and the reduction in the proportion of selected elite individuals. In this case, the number of individuals per generation is set to 100 with the number of elite individuals reduced to 10. This allows for greater exploration of subregions in the state space defined by the current probability matrix from which a smaller percentage of elite individuals are selected. As a result, the probability matrix is based on only the top 10% of individuals. Another difference is the definition of $minProbRST$ as 0.1. Thus, during the reset routine, new individuals are not generated completely randomly; instead, information from previous generations is retained to some extent. The intention

is to preserve the approximate shape of the metal plating between generations, so that it would not need to be rediscovered from random structures. Moreover, the parameter $rstCoeff$ is set to 0.07 for multistate antenna optimization. Setting $rstCoeff$ to a higher value helps suppress the effect of dummy pixels that make it more difficult to activate the reset routine.

As mentioned above, the fitness function has been defined to take into account a wider frequency band. The fitness function f is specified as follows:

$$f = \sqrt{f_{S11}{}^2 + f_{HPBW}{}^2 + f_G{}^2 + f_{GR}{}^2 + f_{AR}{}^2 + f_{ARBW}{}^2}. \tag{5.11}$$

The fitness function is again defined as the Euclidean distance from the ideal solu-
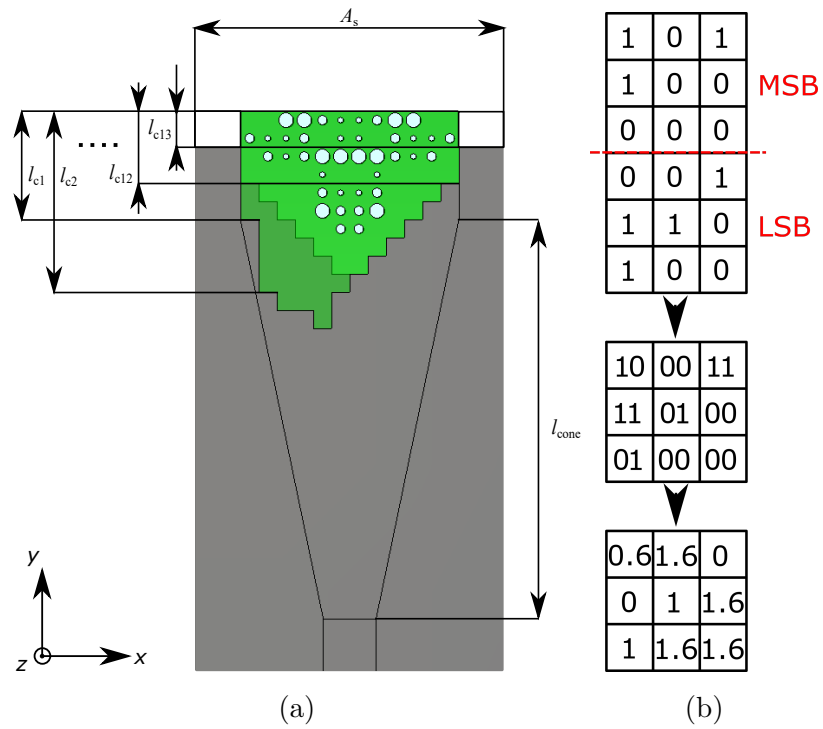
Fig. 5.13: (a) Simplified model of the multistate pixelated CP SIW horn antenna. (b) Process for determining four-state structure from binary matrix.

Parameter	Value	Parameter	Value
$Nelit$	10	$minProb$	0.01
$Niter$	200	$minProbRST$	0.1
$Npop$	100	$sigCoeff$	10
		$rstCoeff$	0.07

Tab. 5.5: Parameter settings for BISO algorithm during multistate pixelated CP SIW horn antenna optimization.
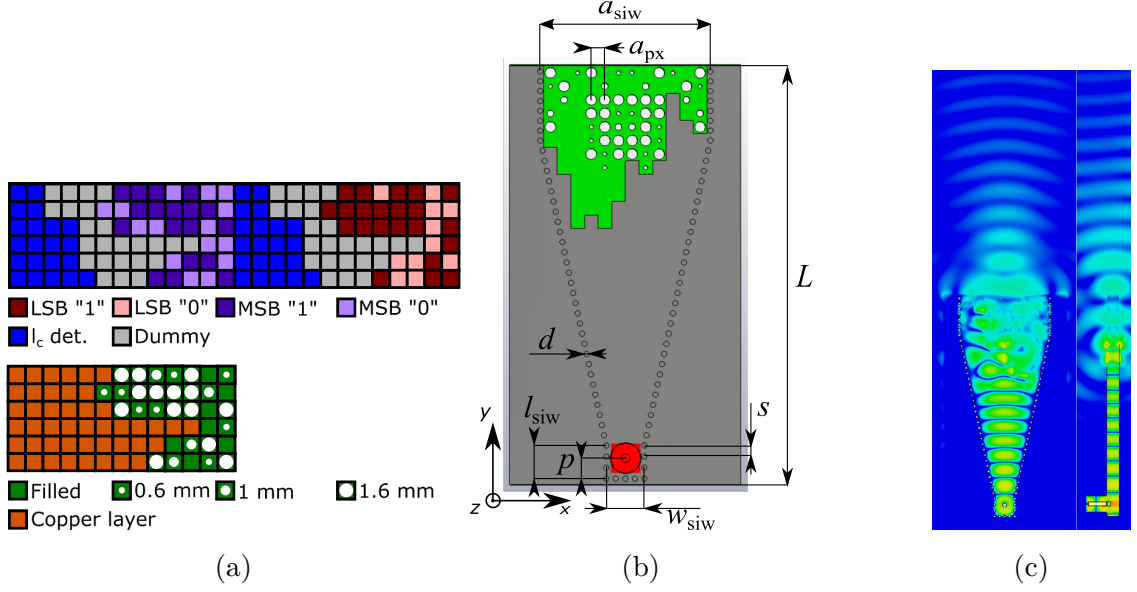
Fig. 5.14: (a) Optimized binary matrix for the multistate pixelated CP SIW horn antenna (top) and resulting pixelated part (bottom). (b) Optimized multistate pixelated circularly polarized antenna with SIW structure and coaxial-SIW transition. (c) Normalized E-field distribution of the multistate pixelated CP SIW horn antenna at 24.125 GHz in xy-plane (left) and yz-plane (right).

tion. The desired -10 BW S11 is 1 GHz. Above this threshold, the f_{S11} is 0, else it is a linear depedency between 0 GHz ($f_{S22} = 1$) and 1 GHz. The normalized component for the S11 BW is defined as:

$$f_{S11} = \begin{cases} 1 - \text{S11BW} & \text{if} \quad \text{S11BW} < 1, \\ 0 & \text{if} \quad \text{S11BW} \geq 1 \end{cases}, \tag{5.12}$$

where $S11BW$ is the -10 dB S11 BW. The component for HPBW is similar to previous cases:

$$f_{HPBW} = \frac{\Delta_{HPBW}}{10}, \tag{5.13}$$

with the only difference being that Δ_{HPBW} represents the average HPBW over the operating band, ensuring that this parameter remains satisfactory across the band. The component f_G is defined as in case of the binary pixelated CP horn antenna:

$$f_G = \begin{cases} 1 & \text{if} \quad \text{G} > 8, \\ -\frac{G}{5} + \frac{13}{5} & \text{if} \quad 8 \leq \text{G} < 13, \\ 0 & \text{if} \quad \text{G} \geq 13 \end{cases}, \tag{5.14}$$

where G is the maximum gain over the 24 GHz ISM band. To ensure stable gain

across the entire frequency band, a component f_{GR} of the form:

$$f_{GR} = \begin{cases} 1 & \text{if} \quad \text{GR} > 4, \\ \frac{GR}{3} - \frac{1}{3} & \text{if} \quad 1 < \text{GR} \leq 4, \\ 0 & \text{if} \quad \text{GR} \leq 1 \end{cases} \quad , \tag{5.15}$$

is defined, where GR is the min-to-max gain ratio over the desired frequency band. When the GR is below 1 dB value of the component is 0. On the other hand, while GR has value 4 dB and worse, it is considered unacceptable and the component takes the value 1. Between these thresholds, the component corresponds to the linear dependence. The last two components are defined to evaluate the antenna in terms of axial ratio. The component:

$$f_{AR} = \begin{cases} 1 & \text{if} \quad \text{AR} > 10, \\ \frac{AR}{10} & \text{if} \quad \text{AR} \leq 10 \end{cases} \tag{5.16}$$

accounted for the AR in the main direction at 24.125 GHz. The component has been modified to has a bigger influence in the context of the fitness function. To account AR BW into the fitness function, the component f_{ARBW} of the form:

$$f_{ARBW} = \begin{cases} 1 - \text{ARBW} & \text{if} \quad \text{ARBW} < 1, \\ 0 & \text{if} \quad \text{ARBW} \geq 1 \end{cases} \quad , \tag{5.17}$$

where $ARBW$ denotes the 3 dB AR BW, is defined. When the AR BW is 1 GHz and greater, the f_{ARBW} is 0, otherwise it grows linearly towards to BW of 0 GHz.

The optimization was performed in the form of four independent runs from which the best design for the physical prototype was selected. Fig. 5.15 shows an example of an optimization run with the above settings. The convergence curve primarily illustrates the influence of the $minProbRST$ parameter where the average fitness values after the reset routine do not reach the same levels as those of the randomly generated population at the beginning of the optimization. Additionally, a higher value of $rstCoeff$ results in more frequent reset routines. The figure presents three selected generations, their best individuals, radiation patterns, and the corresponding probability matrices. During the optimization process, one can observe an initial phase focused on determining the shape of the coating followed by the fine-tuning of the pixel structure configuration. The transition between generations #28 and #29, where generation #29 is the first after the reset routine clearly demonstrates the transfer of the plating trend to subsequent generations. As expected, the probability matrix reveals a slightly increased level of randomness.

The optimized binary matrix and the resulting pixel structure are shown in Fig. 5.14a. The model transformed to the SIW structure is depicted in Fig. 5.14b. The multistate pixelated antenna provides a much more uniform E-field at the aperture (Fig. 5.14c) compared to the binary state pixelated antenna (Fig. 5.9c). The
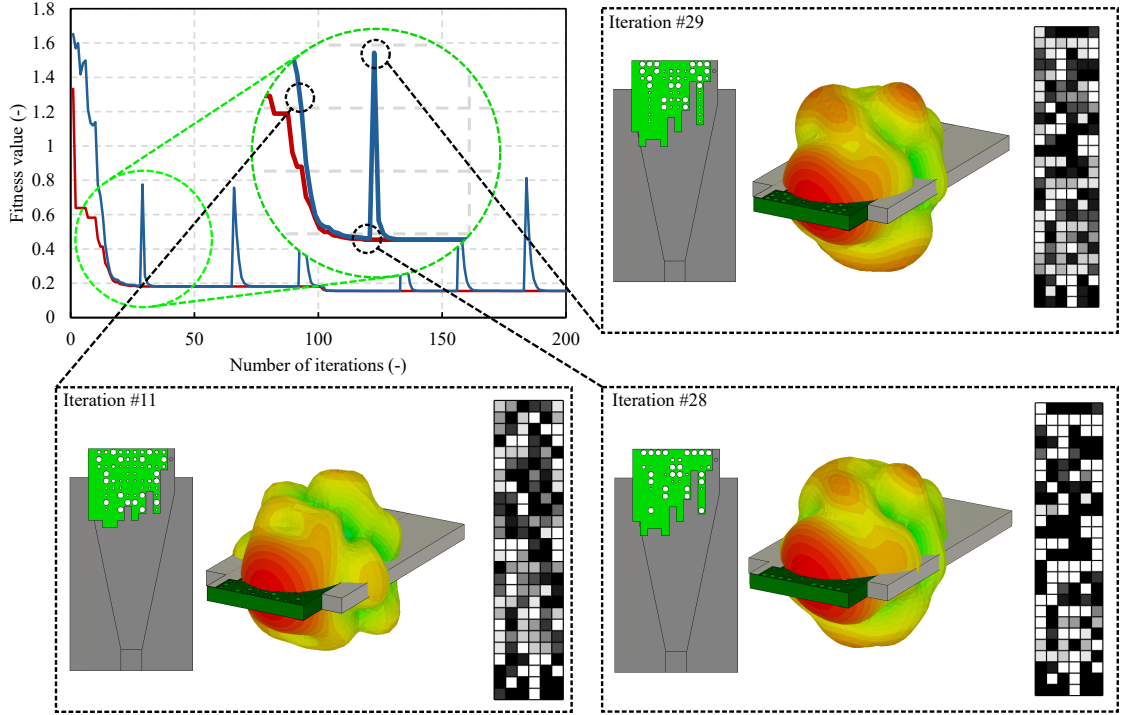
Fig. 5.15: Example of convergence curve from optimization run for CP antenna with a multistate pixelated load. Red line represents fitness function value of the best individual so far while blue line represents mean fitness value of elite group. For three selected generations, best individual and probability matrix used for forming next generation are shown.

Parameter	mm	Parameter	mm
a_{px}	2	lc_8	8-22 (16)
A_s	34	lc_9	4-18 (14)
a_{siw}	24.6	lc_{10}	4-18 (4)
d	0.8	lc_{11}	0-14 (8)
L	66.8	lc_{12}	0-14 (10)
lc_1	12-26 (12)	lc_{12}	0-14 (0)
lc_2	12-26 (16)	l_{cone}	30-44 (44)
lc_3	12-26 (24)	l_{siw}	4.9
lc_4	10-24 (24)	p	3.1
lc_5	10-24 (24)	s	1.5
lc_6	10-24 (20)	w_{siw}	6.4
lc_7	8-22 (14)		

Tab. 5.6: Parameters of the proposed multistate pixelated CP SIW horn antenna.
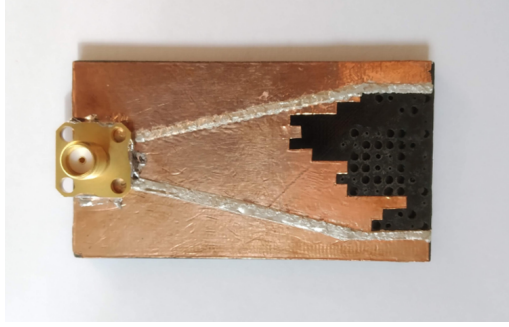
Fig. 5.16: Manufactured prototype of the multistate pixelated CP SIW antenna.

(a)

(b)
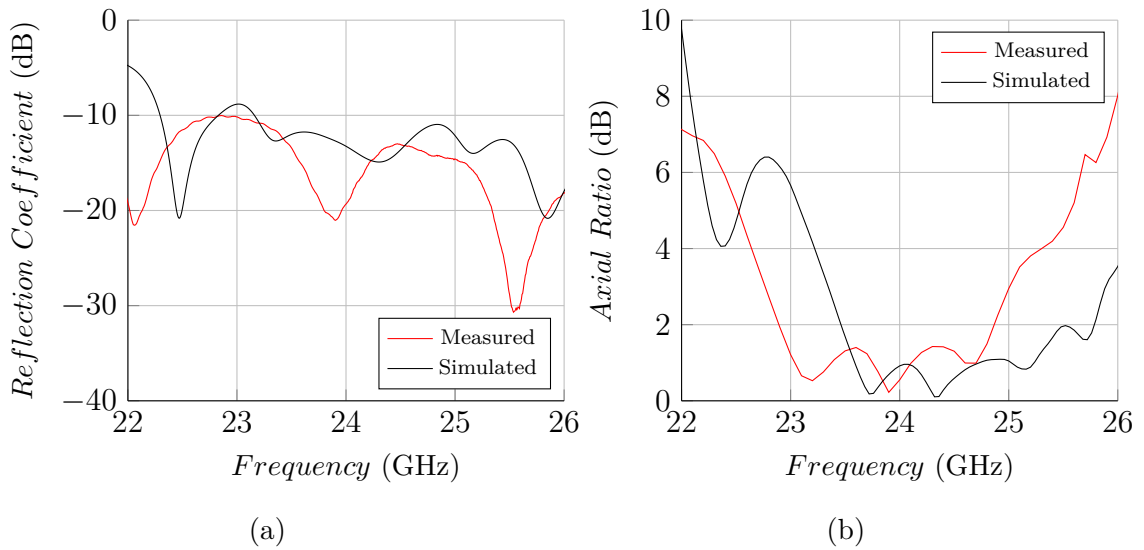
Fig. 5.17: Measured and simulated reflection coefficient (a) and axial ratio (b) of the multistate pixelated CP SIW horn antenna.

dimensions of the optimized model are shown in Tab. 5.6. Values in parentheses are optimized values for parameters $l_1 - l_{cone}$. Note that the distance between centers of pixels is 2 mm.

The manufactured prototype of the antenna is shown in Fig. 5.16. Even this configuration with relatively tiny holes was the Prusa i3 MK3S 3D printer able to manufacture. The antenna was also measured in the anechoic chamber. The simulated and measured results of the reflection coefficient over the frequency band 21-27 GHz are shown in Fig. 5.17a. The measured impedance BW for the reflection coefficient lower than -10 dB is 21.4%. The simulated and also measured AR (Fig. 5.17b) shows that it remains below 3 dB over the whole 24 GHz ISM band. The comparison of the simulated and measured radiation patterns in principal planes (Fig. 5.18) shows good agreement. A nearly equal HPBWs are achieved.
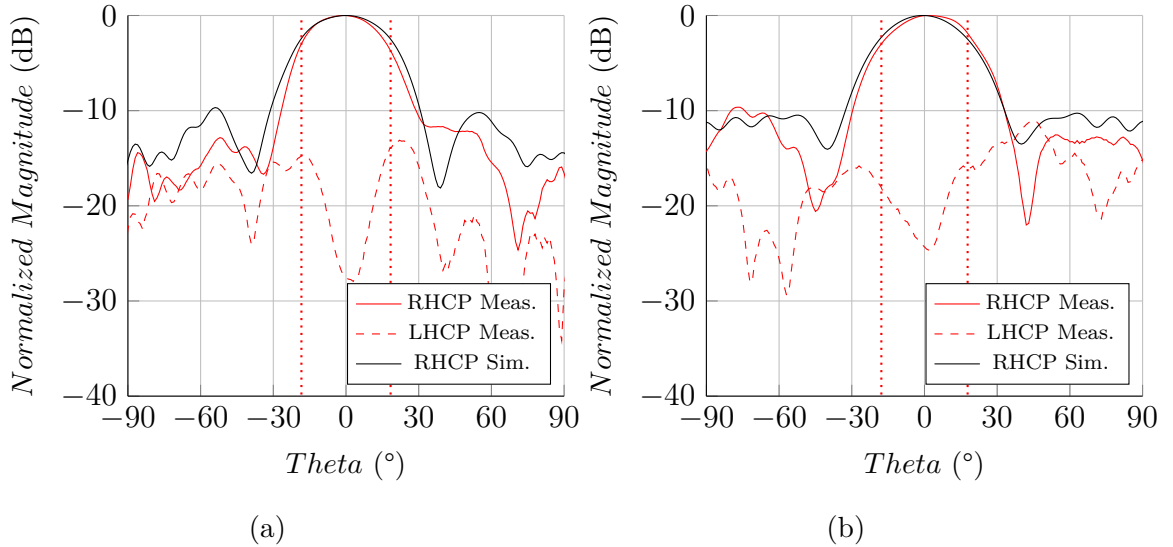
Fig. 5.18: Normalized measured and simulated radiation patterns of the multistate pixelated CP SIW horn antenna at 24.125 GHz: (a) yz plane and (b) xy plane. Measured HPBW is indicated by vertical dotted lines.

Ref	Dimensions (λ_0)	Frequency (GHz)	-10 dB S11 BW (%)	Gain (dBi)	3 dB AR BW (%)	HPBW in principal planes(°)	Note
[74]	(7×4.73×0.12)	25	20	8	8.9	-	multiple antenna elements
[75]	(7.35×3.95×0.12)	24	5	8.5	5.9	22.5/45*	multiple antenna elements
[76]	(2.22×3.23×0.13)	12	7.5	7.5	5	58.4/72*	additional antenna element
[25]	(3.78×2.87×1.23)	28	40	7.8	30	33.5/103.7*	polarizer in front of antenna aperture
[77]	(2.58×1.96×0.22)	24	40	11.2	45	40.3/46.4*	simple single-layer
Binary CP antenna	(7.66×2.4×0.27)	24.125	19**	8.9	2.4	30.6/33.4	simple single-layer
Multi CP antenna	(5.14×2.4×0.27)	24.125	21.4**	9.5	10.8	37.5/38.1	simple single-layer

*Values were determined from published radiation patterns. **Presented -10 dB S11 BW is according to simulated data.

Tab. 5.7: Comparison of the proposed pixelated CP SIW horn antennas with state-of-the-art works.

The comparison of the proposed pixelated CP SIW antennas with state-of-the-art designs is presented in Tab. 5.7. The proposed antennas are based on a simple single-layer structure which is advantageous in terms of manufacturing. However, the parameters of the proposed antennas are roughly comparable to those of the state-of-the-art designs. As illustrated, the four-state pixelated antenna outperforms the binary pixelated antenna in all parameters, even when its length is reduced. Further investigations may identify the optimal design parameters for pixelated CP SIW horn antennas.

5.4 Summary

In this chapter, the procedure for the design of pixelated SIW horn antennas is presented and exploited for the design of three pixelated SIW horn antennas. The main goal was to achieve nearly equal HPBWs in the principal planes of single-layered SIW horn antennas. This goal is successfully achieved, and three antennas were optimized and experimentally verified to demonstrate the process.

The algorithm presented in the previous chapter, BISO, is employed to optimize three pixelated SIW horn antennas designed for the 24 GHz ISM band. One LP and two CP antennas are proposed. All three antennas were manufactured by a low-cost FDM 3D printing technology. The measured data fit very well with the simulated ones.

The method of pixelization appears promising for SIW horn antennas. The fitness function may incorporate the desired features of the proposed antennas, as pixelization has the ability to find unconventional solutions to meet specific requirements.

Future work could focus on exploring different materials for the substrate and examining the limitations of pixelated SIW horn antennas. Additionally, the use of alternative pixel shapes could unlock new possibilities for improving performance. Another potential avenue of research could involve designing a pixelated SIW horn antenna with an integrated RF circuit, fabricated entirely using an all-in-one method with 3D-printed PCBs.

6 Pixelated Waveguide Filters

In this chapter, an automatic design procedure for waveguide filters based on BISO algorithm is proposed. The procedure is exploited for the design of two X-band pixelated waveguide filters. First, a multistate pixelated filter is designed [JZ78]. The filter structure consists of a pixelated metal pattern on the wider walls of the WR-90 waveguide within the given space. The filter was fabricated using SLA 3D printing technology and subsequently metallized. Since the metallization of dielectric materials can be challenging, especially for complex structures such as pixelated ones, an alternative filter design was proposed to eliminate the need for metallization of the pixelated section [JZ79] (submitted). The resulting design is a waveguide filter based on a 3D-printed dielectric insert placed in an evanescent-mode waveguide. The results of this chapter are related to the Objective 3 of this thesis.

6.1 Design Procedure Description

The procedure presented in this chapter is capable of finding a suitable solution within a given waveguide space based solely on the desired filter characteristics. It consists of the following steps:

- **Waveguide Definition**

First, the cross-sectional dimensions and the total length of the waveguide in which the filter will be implemented must be defined. The cross-sectional dimensions are directly determined by the cutoff frequency of the dominant TE_{10} mode which sets the lower bound of the operating frequency band. Mechanical or integration requirements usually constrain the waveguide length. These parameters define the physical space available for placing the filter elements. In the case of a filter based on a waveguide operating in the evanescent mode, the cross-sectional dimensions must be reduced so that the entire operating frequency band lies below the cutoff frequency of the dominant mode.

- **Filter Pixelization Strategy**

In the next step, the form of pixelization is defined. Two different approaches are considered in this thesis. The first approach is a metalized multi-state pixelized structure where the filter is formed by dividing the waveguide into discrete sections (pixels) each described by multiple bits to enable multi-state pixelization [JZ78].

The second approach is an evanescent-mode filter with a binary pixelated dielectric insert [JZ79]. In this case, the waveguide dimensions are such that the cutoff frequency lies above the desired operating band. The inclusion of dielectric materials locally increases the relative permittivity which introduces frequency-selective

behavior and thus the desired filter characteristic is formed.

- **Fitness Function Definition**

The fitness function is directly derived from the desired frequency response. Specific forbidden regions has to be defined for reflection (S11) and transmission (S21) coefficients over the frequency band of interest. These regions represent unacceptable levels of insertion loss or return loss. If the simulated response of a candidate design crosses into any of these regions the fitness function assigns it a non-zero value indicating a deviation from the target behavior.

- **Optimization Process**

During the optimization process, populations of candidate filters are iteratively evaluated using numerical simulation. For efficiency, it is crucial to simplify the electromagnetic model wherever possible. This may involve applying simplified geometry only to the interior space of the filter or symmetry assumptions to reduce computational time while capturing the underlying physical behavior.

- **Filter Finalization**

In the final step, the best-performing pixel configuration is translated into a physical structure ready for fabrication. This may include adjustments to accommodate manufacturing constraints, integration of suitable input/output transitions (such as waveguide flanges or coaxial probes), and possibly fine-tuning of the pixel shapes or materials based on detailed full-wave simulations. These post-optimization refinements help to ensure that the fabricated filter meets both electromagnetic and mechanical requirements.

Each of these steps will be illustrated in the following subchapters through the design and optimization of two example filters using different pixelization strategies.

6.2 Fitness Function Definition

Both filters presented in this chapter are designed to have a BW of 1 GHz, a center frequency of 10 GHz, a passband loss of 0.5 dB, and a reflection coefficient of -15 dB. The fitness function was defined based on forbidden regions (Fig. 6.1) in the S11 and S21 responses of the filter.

The fitness function is expressed as the sum of penalties for each frequency point. If S11 or S21 at a given frequency point falls within a forbidden region the penalty for that point is greater than zero. The fitness function is defined as:

$$F = \sqrt{F_{S11}^2 + F_{S21}^2},$$
(6.1)

where F_{S11} and F_{S21} are sub-fitness functions defined as:

$$F_{S11} = \frac{1}{N} \sum_{n=1}^{N} \begin{cases} \frac{0.941 - S11_n}{0.944} & if & S11_n < 0.944 \ \& \ (f_n \leq 9 \ OR \ f_n \geq 11) \\[2ex] \frac{0.708 - S11_n}{0.708} & if & S11_n < 0.708 \ \& \ (9 < f_n \leq 9.5 \ OR \ 10.5 \leq f_n < 11) \\[2ex] \frac{S11_n - 0.177}{0.823} & if & S11_n < 0.177 \ \& \ (9.6 < f_n < 10.4) \\[2ex] 0 & else \end{cases} \quad (6.2)$$

and

$$F_{S21} = \frac{1}{N} \sum_{n=1}^{N} \begin{cases} \frac{S21_n - 0.1}{0.9} & if & S21_n < 0.1 \ \& \ (f_n \leq 9 \ OR \ f_n \geq 11) \\[2ex] \frac{S21_n - 0.708}{0.292} & if & S21_n < 0.708 \ \& \ (9 < f_n \leq 9.5 \ OR \ 10.5 \leq f_n < 11) \\[2ex] \frac{0.944 - S21_n}{0.944} & if & S21_n < 0.944 \ \& \ (9.6 < f_n < 10.4) \\[2ex] 0 & else \end{cases} \quad (6.3)$$

where N is the number of frequency points, f_n is the frequency at the point in GHz, and $S11_n$ and $S21_n$ are the magnitudes of the reflection and transmission coefficients at the frequency point, respectively.

The filters are modeled in CST Studio Suite to obtain the scattering parameters S11 and S21. These parameters are then used to compute the fitness functions described in equations (6.2) and (6.3) using an in-house Matlab script. The parameters of the BISO algorithm during the optimization were set as shown in Tab. 6.1. The parameters were selected after several test runs of the optimization to achieve an
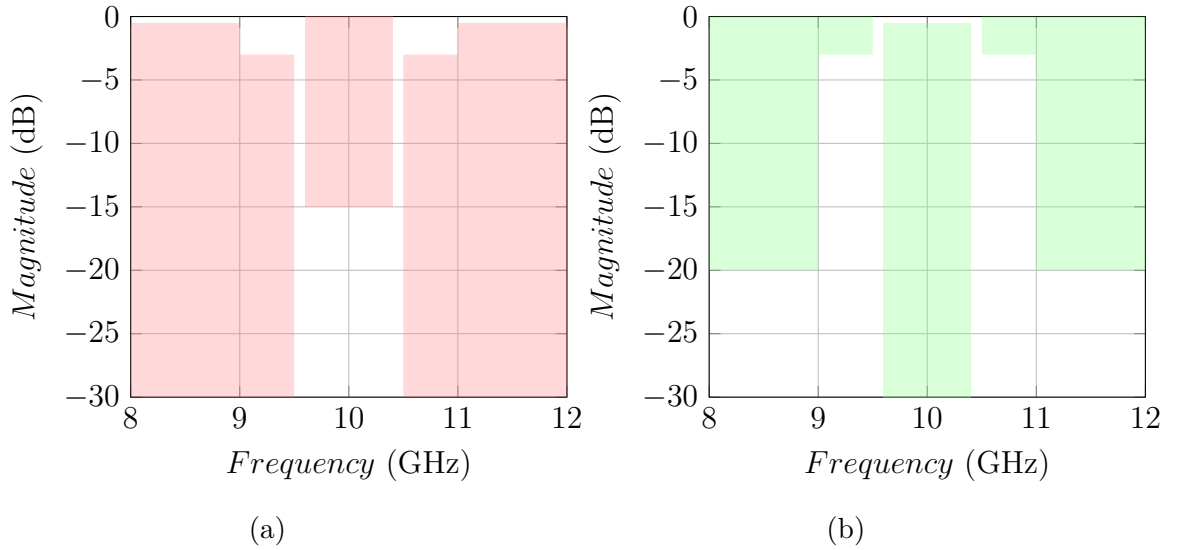
Fig. 6.1: Forbidden regions for S11 (red) and S21 (green) parameters.

optimal balance between the algorithm's ability to explore and exploit the search space for this type of task.

6.3 Multistate Pixelated Waveguide Bandpass Filter

The multistate pixelated bandpass filter can be viewed as a 60 mm long section of a WR-90 waveguide ($a = 22.86$ mm, $b = 10.16$ mm, cutoff frequency of the dominant mode $f_c = 6.557$ GHz) with an internal pixelated structure (Fig. 6.2a). The pixelated structure consists of two identical parts, each containing a 16×40 pixel grid, positioned on the bottom and top walls of the waveguide. Each individual pixel is a block with a square base measuring 1.43 mm per side (1/16 of the width of the WR-90 waveguide) and a height of either 5.08 mm (half the height of the WR-90 waveguide), 3 mm, 2 mm, or 1 mm.

To achieve four states for each pixel, the optimized binary matrix is split into MSB

Parameter	Value	Parameter	Value
$Nelit$	5	$minProb$	0.005
$Niter$	250	$minProbRST$	0.15
$Npop$	50	$sigCoeff$	10
		$rstCoeff$	0.01

Tab. 6.1: Parameter settings for BISO algorithm during filter optimization.
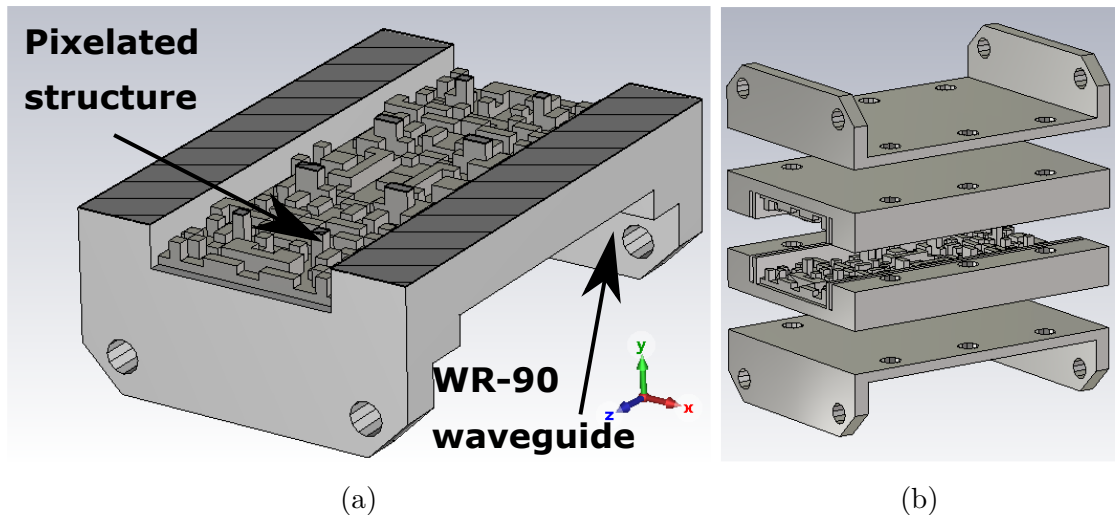
Fig. 6.2: (a) Cross-section of the proposed multistate pixelated waveguide filter. (b) Assembly scheme.

and LSB parts (corresponding to the most and least significant bits). The values in this matrix define the pixel heights according to the following rules: 00 $\rightarrow$ 1 mm, 01 $\rightarrow$ 2 mm, 10 $\rightarrow$ 3 mm, and 11 $\rightarrow$ 5.08 mm. As mentioned earlier, the structure consists of 16×40 pixels; however, due to symmetry along both the X and Z axes, the optimized pixelated matrix contains only 8×20 pixels. Since each pixel is represented by two bits, the total size of the optimized binary matrix is 16×20 bits.

In addition to the optimization setup described above, two additional features are implemented to improve convergence in the initial phase of the optimization. The first is adjusting the probability of a "1" occurring in the initial generation to only 15%. If the probability were set to 50%, most of the generated structures were non-transmissive across the entire observed band. As a result, it took longer for individuals containing passband regions to become dominant which delayed the optimization of the filter response.

The second feature is the automatic discarding of individuals with zero passband regions in the observed band. This is enforced by the condition that if at no frequency point $S21 > S11$ then $F = 1$. This mechanism prevented the retention of individuals with very low transmission coefficients across the band which would otherwise achieve relatively good fitness function values in the early stages.

With the final setup, four independent optimization runs were performed and the best individual was subsequently implemented as a physical prototype. An example of an optimization run is shown in Fig. 6.3. For the three selected generations, the best individual and the probability matrix used to create the next generation are shown. As seen in the figure, the algorithm initially explores a coarse filter structure through randomly generated configurations followed by a steep convergence phase. The probability matrices confirm the low density of ones as discussed earlier. It can be observed that the algorithm initially converges to a two-pole solution; however, after the first reset routine (iteration #40) a third pole emerges.

The optimized binary matrix is shown in Fig. 6.4. The simulated E-field distributions of the proposed filter at 8, 10, and 12 GHz are shown in Fig. 6.5a, clearly illustrating suppression below and above the passband.

The proposed pixelated filter was manufactured using SLA 3D printing technology. The filter was fabricated as four independent parts (Fig. 6.2b) which were assembled using screws. The parts were subsequently electroplated with copper. One side of the manufactured filter is shown in Fig. 6.5b before copper plating and in Fig. 6.5c after copper plating.

The manufactured filter was measured using a VNA Rohde & Schwarz ZVL13 with Through-Reflect-Line (TRL) calibration applied. The measured and simulated results are shown in Fig. 6.6. The measured insertion loss within the passband is

below 0.75 dB, and the reflection coefficient is below -10.4 dB. The measured BW is 1.02 GHz (9.51 – 10.53 GHz). A good agreement between the simulated and measured results can be observed with minor discrepancies attributed to imperfections in the manufacturing process.
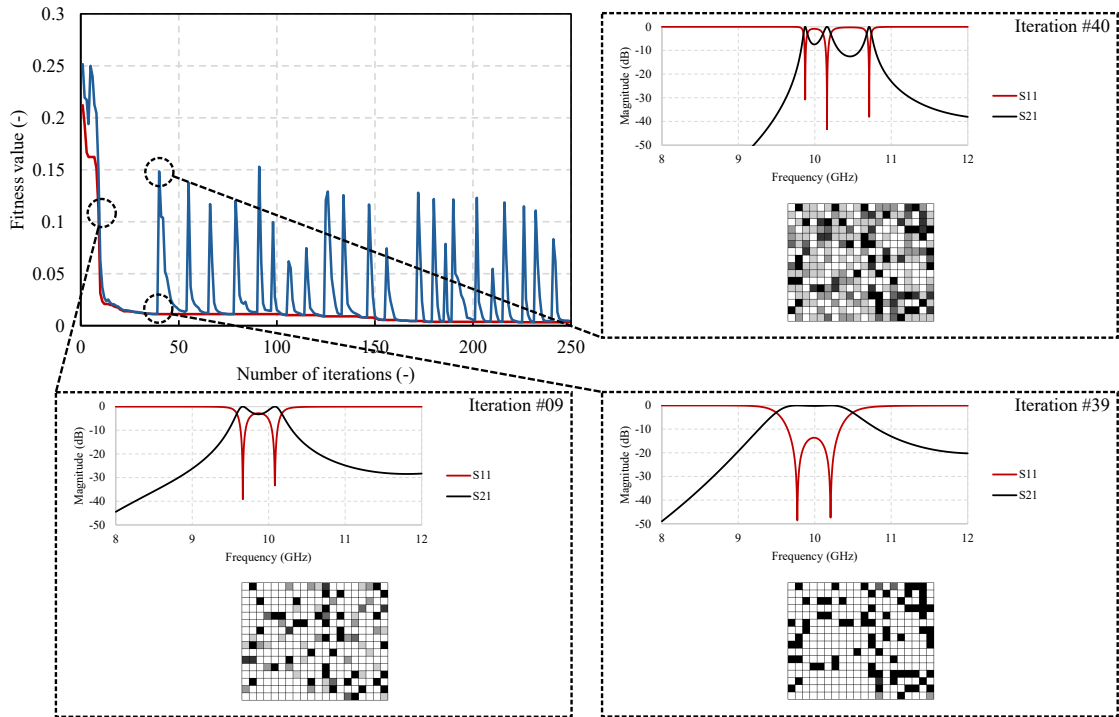
Fig. 6.3: Example of convergence curve from optimization run for multistate pixelated waveguide filter. Red line represents fitness function value of the best individual so far while blue line represents mean fitness value of elite group. For three selected generations, best individual and probability matrix used for forming next generation are shown.
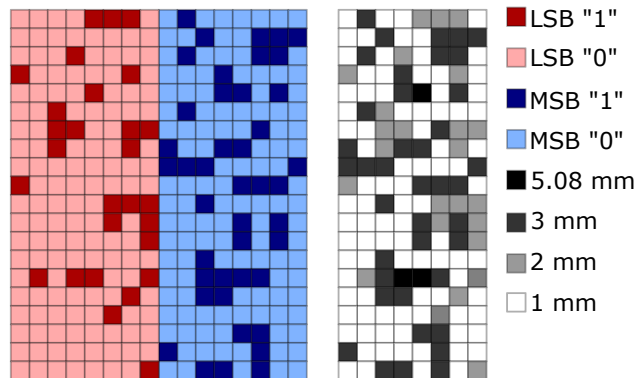
Fig. 6.4: Optimized binary matrix (left) and the resulting pixelated structure (right).

73
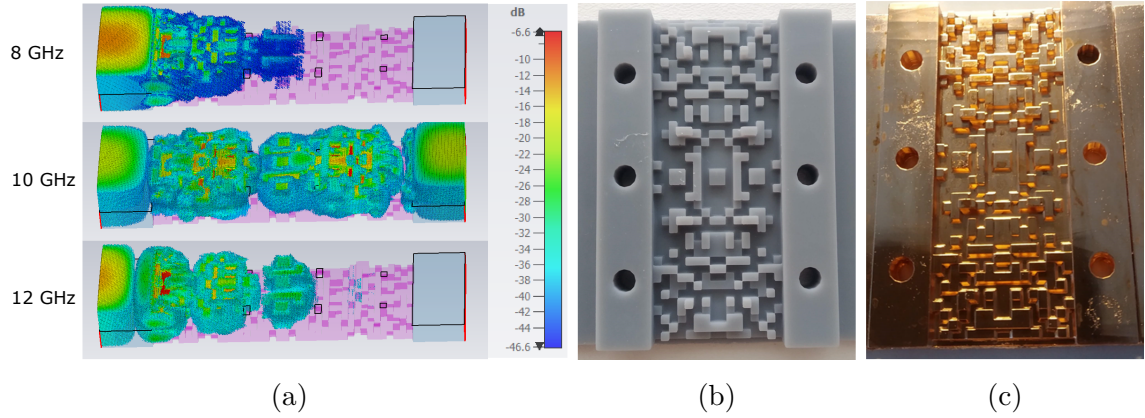
Fig. 6.5: (a) E-field distribution of the proposed filter. 3D-printed parts of the filter (b) before plating and (c) after plating.
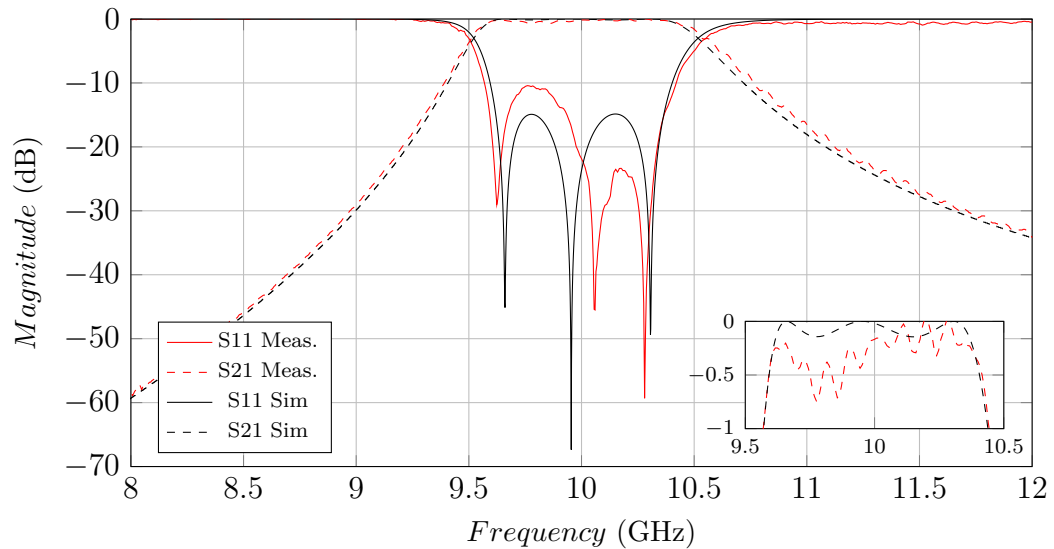
Fig. 6.6: Simulated and measured results of the proposed multistate pixelated filter.

6.4 Evanescent Mode Waveguide Bandpass Filter

The metallization of a pixelated structure can present significant challenges. Therefore, a simplified waveguide filter is introduced from this perspective. The configuration of the proposed filter (depicted in Fig. 6.7) is based on a 100 mm long piece of WR-90 waveguide with a width of $a = 22.86$ mm, a height of $b = 10.16$ mm, and the cutoff frequency $f_c = 6.557$ GHz. This waveguide includes an integrated narrowed section, measuring 12 mm in width, designed to increase the cut-off frequency of the fundamental TE_{10} mode ($f_c = 12.49$ GHz). As a result, the operational frequency band of the filter lies below this cut-off frequency. To achieve the desired filter

response, a 3D-printed pixelated component is inserted into this narrowed section. This component consists of a grid of 6×40 positions where each position can either be filled with material or remain void. Each pixel is a block with a square base of 2×2 mm² and a height of 10.16 mm. Due to the symmetry of the pixelated section, the optimized binary matrix consists of 6×20 bits.

Unlike the multistate filter, in this case the initial generation was created with an equal probability of generating "1" and "0". Due to the operating principle of the filter, the probability of generating a structure without any pass areas across the entire monitored frequency band is very low. Therefore, the condition $S21 > S11$ was also not implemented. Four independent optimization runs were performed and the best result was selected for prototype implementation. An example of an optimization run is shown in Fig. 6.8. The reflection and transmission coefficients of the best individuals, as well as the probability matrix used for generating the next generation, are shown for three selected generations. Compared to the multistate filter optimization, the average fitness value of the elite group after the reset routine is lower and the convergence appears to be more gradual. This can be attributed to the fact that, in the case of the dielectric-insert filter, individual pixels have a less significant impact on the filter characteristics. Even after the reset routine, the influence of the previous generation remains significant which was not as apparent during the optimization of the multistate filter.

The resultant optimized binary matrix is depicted in Fig. 6.9a. The E-field distribution of the proposed evanescent mode filter is shown in Fig. 6.9b. As can be

<center>(a)   (b)</center>
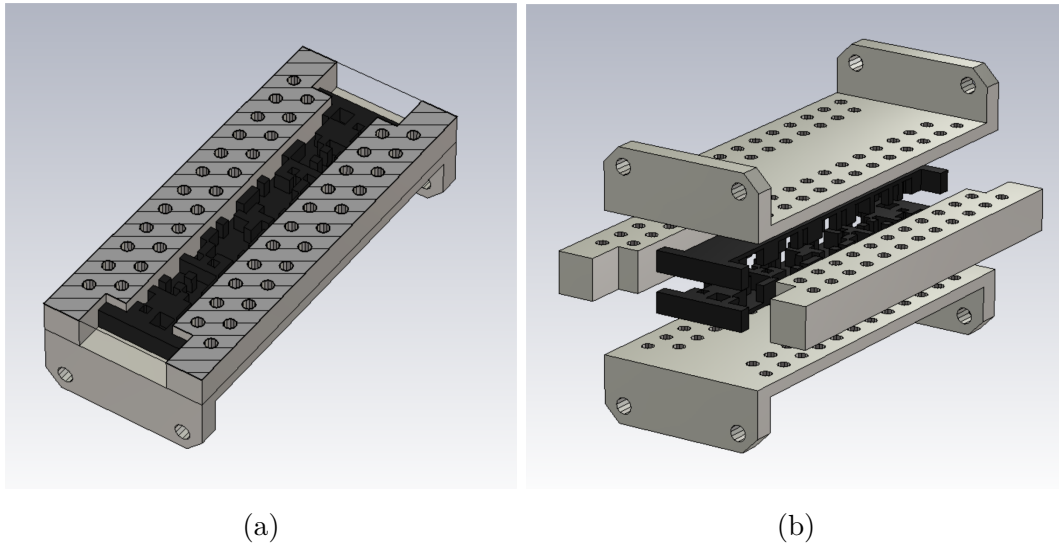
Fig. 6.7: Proposed evanescent mode waveguide filter with pixelated structure. (a) Cross-section of the filter. (b) Assembly scheme.

seen, at frequencies below the operating band, suppression occurs at the interface of the narrowed section due to the frequency being below the critical threshold. At the center of the operating band, the optimized structure acts as a series of transitions. At 12 GHz, the suppression is achieved due to the dielectric insert.

To simplify the manufacturing process, the optimized pixelated component was produced in two parts (Fig. 6.7b). Fabrication was carried out using a low-cost FDM 3D printer, specifically the Prusa MK3 model, with XT copolyester filament from Colorfabb [60]. During the optimization, the dielectric constant was set to 2.9 and the loss tangent to 0.005. To reduce prototype production time, the evanescent mode waveguide was also 3D printed and subsequently coated with a layer of copper foil (Fig. 6.10). Given its relatively simple geometry, this component can alternatively be manufactured using a CNC milling machine. Moreover, a waveguide section with an appropriate cut-off frequency could also serve as a viable substitute.

The manufactured prototype of the proposed filter was measured using a Rohde & Schwarz ZVA67 vector network analyzer with TRL calibration. The comparison between the measured and simulated results is presented in Fig. 6.11. The measured
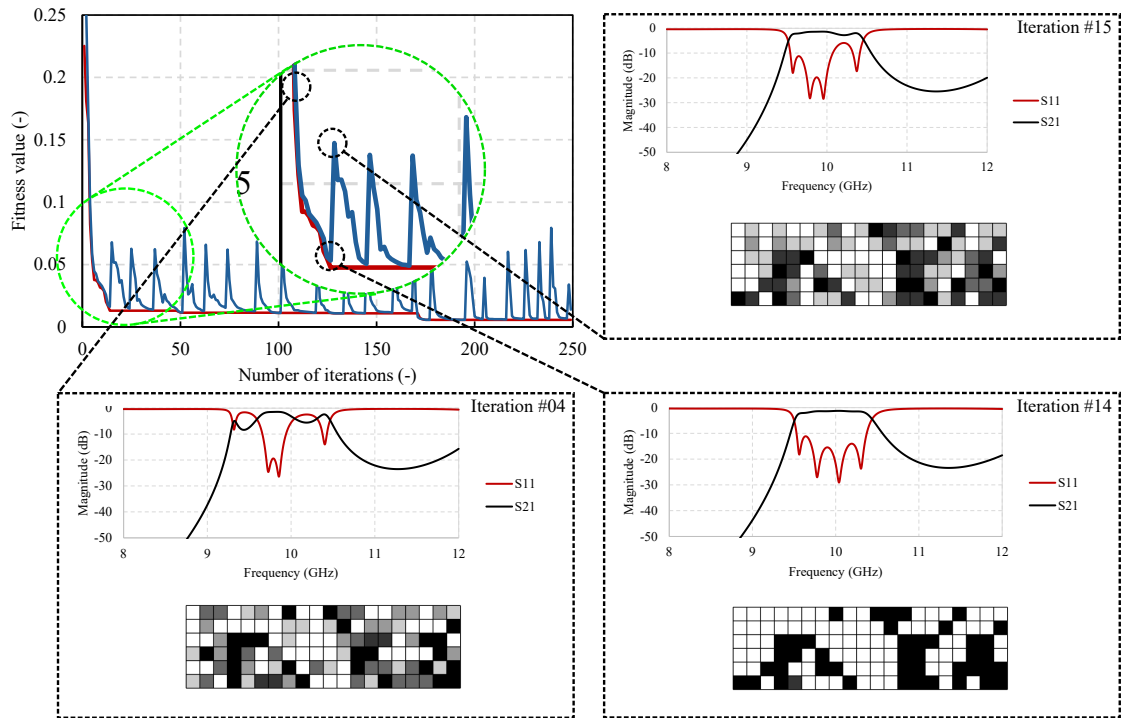
Fig. 6.8: Example of convergence curve from optimization run for pixelated evanescent mode waveguide filter. Red line represents fitness function value of the best individual so far while blue line represents mean fitness value of elite group. For three selected generations, best individual and probability matrix used for forming next generation are shown.

transmission coefficient within the passband is below -1.67 dB, and the measured passband spans 1.03 GHz (from 9.48 GHz to 10.51 GHz). Spurious resonances appearing above 12 GHz could potentially be mitigated through adjustments to the fitness function. Specifically, elevating the desired attenuation at the band edge could help.

As can be seen, this approach suffers from relatively high passband losses. This is attributed to the use of a low-cost thermoplastic material in the fabrication process, which has a somewhat higher loss tangent. However, this limitation can be effectively addressed by utilizing specialized 3D printing filaments designed for RF applications. Tab. 6.2 summarizes the simulated passband transmission coefficients based on varying loss tangents. Notably, the use of XT copolyester with a loss tangent of 0.005 should theoretically yield a transmission coefficient of -1.18 dB. It's

(a) (b)
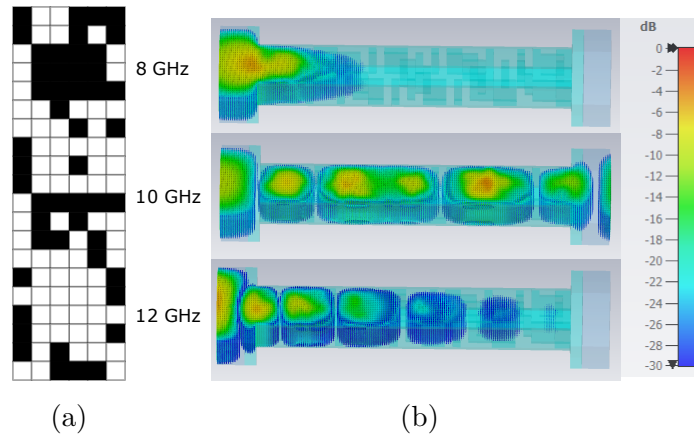
Fig. 6.9: (a) Optimized binary matrix representing one half of the insert inside the filter. (b) E-field distribution of the filter.

(a) (b)
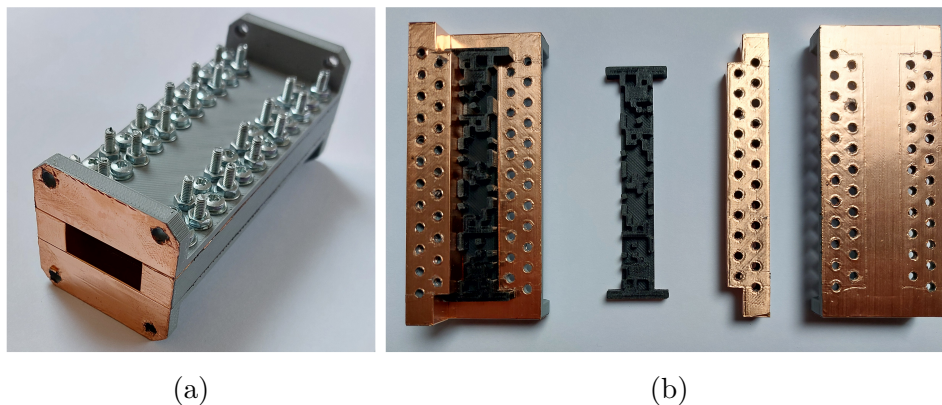
Fig. 6.10: Manufactured prototype of the proposed evanescent mode waveguide filter with pixelated structure. (a) Assembled prototype. (b) Disassembled prototype.
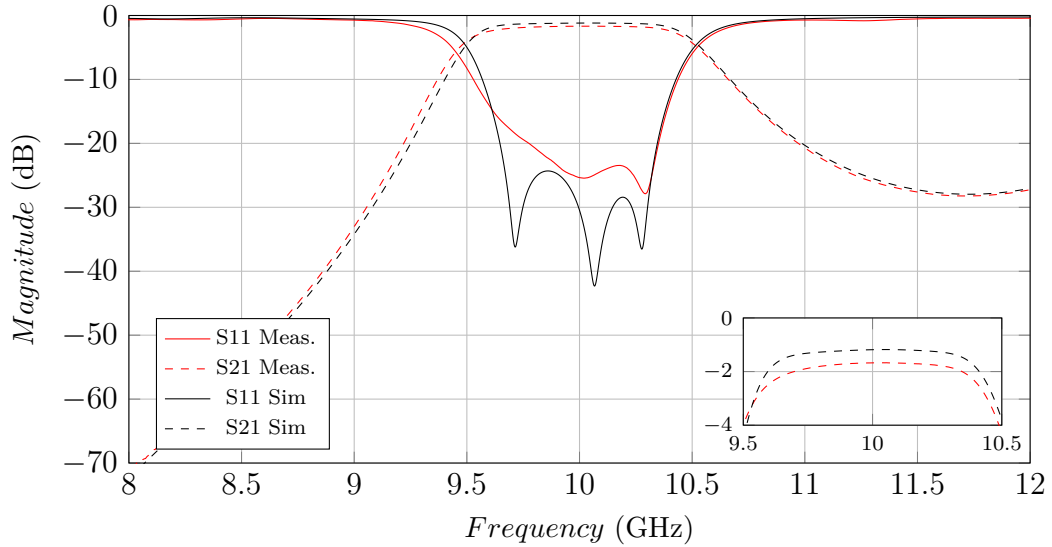
Fig. 6.11: Simulated and measured results of the proposed evanescent mode filter.

Loss tangent [-]	Transmission coefficient [dB]
0	-0.02
0.0025	-0.59
0.005	-1.18
0.0075	-1.77
0.01	-2.36

Tab. 6.2: Simulated transmission coefficient based on loss tangent.

worth mentioning that the additional loss observed might be due to the imperfect realization of the waveguide structure. Alternatively, employing CNC manufacturing for the waveguide, coupled with materials possessing a suitable loss tangent, should make it feasible to achieve a passband transmission coefficient of -0.5 dB.

6.4.1 Sensitivity Analysis

To uncover the discrepancy between the simulated and measured results, additional analysis is carried out. Firstly, extra material is added at the corner junction of two pixels, as depicted in Fig. 6.12a. Due to the printing process, small gaps occur at these junctions. Since different printing profiles may lead to changes in the effective permittivity of the printed material, this is also included in the analysis of the manufacturing process. The printing profile of the filter insert is shown in

Fig. 6.12b. As can be seen, most parts of the pixelated structure consist only of brim traces, which are printed concentrically, while the inner print style (depicted in purple) is rectilinear. It is expected that these parts will have slightly different effective relative permittivity. Another effect of the printing process is the rounding of the corners as illustrated in Fig. 6.12c. Due to the manufacturing of the insert in two pieces, a gap between them may occur. Therefore, this effect is also modeled as well as a possible gap between the insert and the waveguide in the H-plane.

The parameters for the sensitivity analysis are listed below:

- The radius of the corners $r_c \in (0.2, 0.6)$ mm
- The gap between the parts of the insert $gap_{in} \in (0, 0.05)$ mm
- The gap between the insert and the waveguide $gap_{out} \in (0, 0.05)$ mm
- The difference in the effective permittivity $\epsilon_{diff} \in (-3, 3)$ %

The influence of the parameters is shown in Fig. 6.13. The default model param-

(a)   (b)

(c)
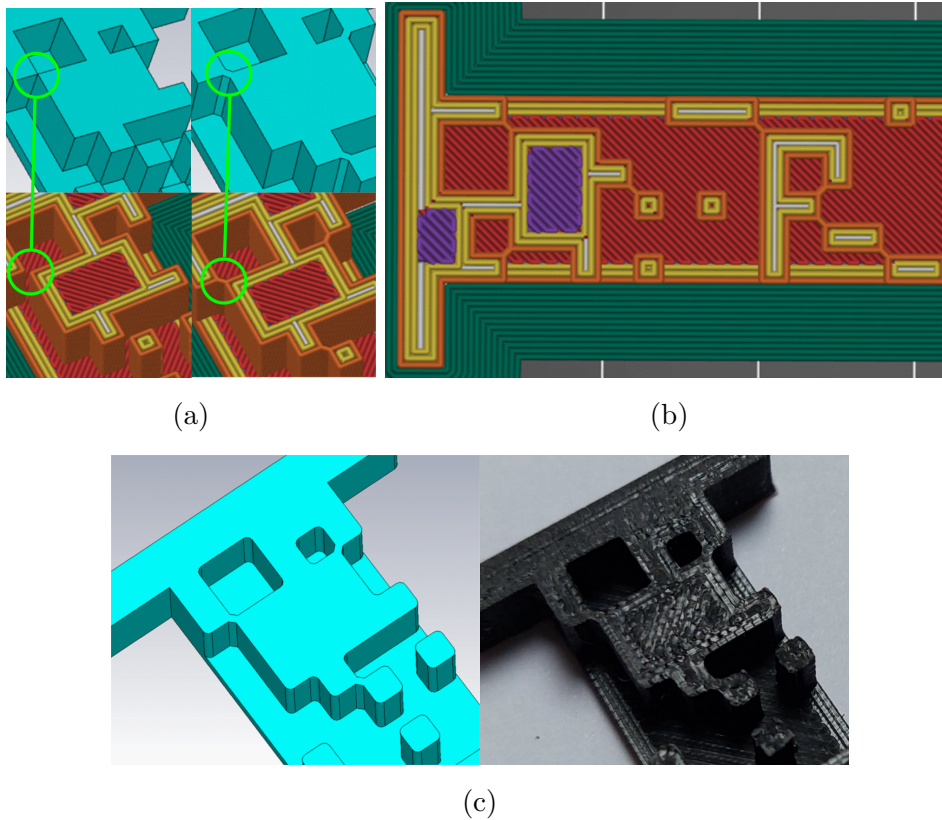
Fig. 6.12: (a) Illustration of added material on corners to ensure their connection. Detail of numerical models in CST (top) compared with prepared data for 3D printing in Prusa Slicer environment (bottom). (b) Printing profile of filter insert showing variations in printing style. (c) Illustration of corner rounding. Detail of numerical model in CST (left) compared with 3D-printed structure (right).
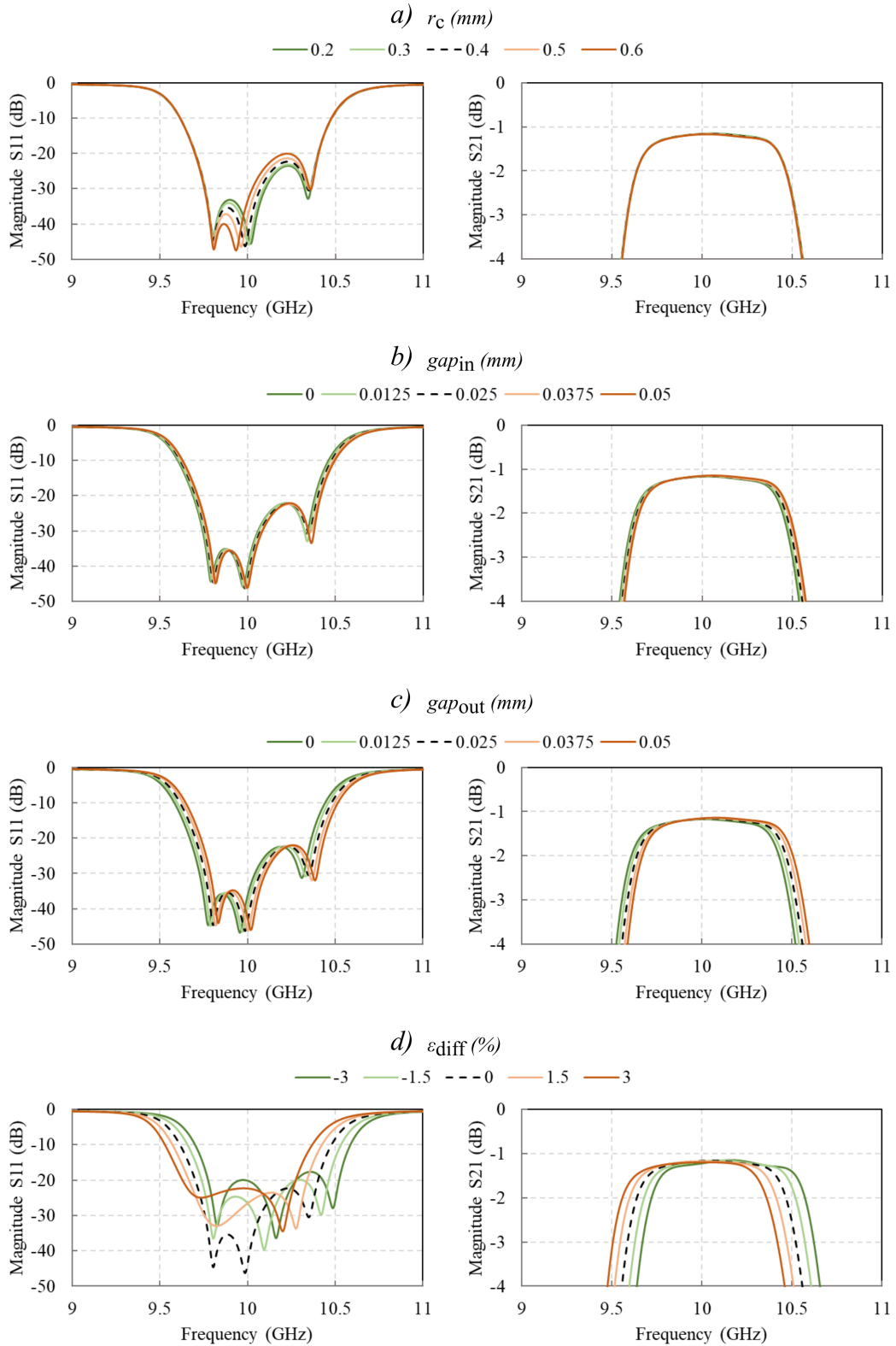
Fig. 6.13: Results of sensitivity analysis. Filter responses for sweep of: a) radius of corners, b) gap between parts of insert, c) gap between insert and waveguide, and d) difference in effective permittivity.

eters are: $r_c = 0.4$ mm, $gap_{in} = 0.025$ mm, $gap_{out} = 0.025$ mm, $\epsilon_{diff} = 0$ %. Based on the results, it is clear that the gaps have a negligible influence on the resulting response as shown in Fig. 6.13b,c. Their effect is limited to a slight frequency shift of the filter response. On the other hand, rounding the corners causes almost no frequency response shift but the effect on the filter poles can be observed Fig. 6.13a. Therefore, the effect of corner rounding is more significant as it cannot be assumed to be linear. The most influential factor on the filter response is the difference in the effective permittivity of segments of the pixelated part as shown in Fig. 6.13d. The sweep of this parameter leads to frequency shifting as well as changes in the poles.

When comparing the measured filter response with the results of the sensitivity analysis, the discrepancies (especially the suppression of the lowest pole of the filter) can be attributed to the combined effects of the corner rounding and the differences in the permittivity of the pixelated part segments.

6.5   Comparison with State of the Art

The proposed filters are compared with similar state-of-the-art filters in Tab. 6.3. Compared to state-of-the-art designs, this approach does not require any predefined filter template or filter order. Notably, in [36], the authors highlight the difficulty of generating a multipole design using non-resonant structures due to optimization's tendency to get stuck in a local minimum with only one pole. In contrast, the procedure presented in this work can autonomously determine the required number of poles to meet the desired filter response. The main issue is the relatively high passband loss in the case of the evanescent mode filter which is mainly caused by the dielectric losses of the material used.

Reference	Frequency (GHz)	Size (λ)	FBW (%)	Passband S_{21} (dB)	Manufacturing technique	Metalization
Multistate filter	10.02	2.00	10.2	<-0.75	SLA	YES
Evanescent mode filter	10	3.33	9.7	<-1.67	FDM	NO
[80]	10.24	2.79	6.8	<-1.05	FDM	YES
[81]	10.05	4.37	5	<-0.11	SLA	YES
[82]	10.26	0.71	5.1	<-2.1	Polyjet	YES
[83]	3.68	3.57	3.26	<-3.7	FDM	NO
[83]	3.68	3.57	3.26	<-4.3	FDM	NO
[84]	32	2.99	1	<-0.56	SLA	YES
[84]	32.01	3.84	5	<-0.58	SLA	YES
[84]	32.17	3.84	5	<-0.43	SLA	YES
[84]	32	3.63	3	<-0.43	SLA	YES
[39]	32	3.52	3.12	<-0.84	SLA	YES

Tab. 6.3: Comparison of the proposed filters with published 3D-printed waveguide filters.

6.6 Summary

In this chapter, a unique design procedure for waveguide filters is presented. The procedure is based on a pixelization strategy with a high degree of automation and is solely driven by the required filter response.

The design procedure is verified through the design of two X-band waveguide filters. First, a multistate pixelated filter is introduced. The filter structure is realized as a pixelated metal structure on the wider walls of the WR-90 waveguide within the available space. The filter was manufactured using SLA 3D printing technology and subsequently metalized. Since metalizing dielectric material can be a challenge, especially when the structure is as complex as the pixelated design, the next filter is proposed to eliminate the need for metalizing the pixelated part. The result is a waveguide filter based on a dielectric 3D-printed insert in an evanescent mode waveguide.

The proposed filters demonstrate the ability and versatility of the procedure for designing microwave structures. However, further exploration of its limits should be the subject of future research. The procedure may also be applicable to other microwave waveguide products, such as power dividers, diplexers, etc.

7 Conclusions

This dissertation successfully addressed the set objectives by developing novel methods for the design and optimization of microwave pixelated structures, as well as investigating the material properties of 3D-printed components. The main contributions of this work are summarized as follows:

Objective 1: Development of an Efficient Optimization Procedure for Pixelated Structures

An optimization algorithm tailored for pixelated structures was developed and validated. Binary Ink Stamp Optimization algorithm demonstrated strong performance in both unimodal and multimodal problems. Based on benchmark results, BISO outperforms other algorithms in most cases. The key feature of the algorithm for the optimization of the binary patterns is that the algorithm reflects the significance of the bits during the optimization process. The robustness of BISO was demonstrated through its application in antenna and filter designs, contributing to significant advancements in the field of microwave optimization. The algorithm was presented in the journal paper [JZ64].

Objective 2: Design Procedure for Pixelated SIW Horn Antennas

A novel design procedure for SIW horn antennas based on pixelated loads was developed and successfully implemented. By using a pixelated dielectric lattice, horn antennas with nearly equal HPBWs in the principal planes were realized, overcoming a key limitation in the design of SIW horn antennas. Three antennas, including one linearly polarized and two circularly polarized designs, were optimized and fabricated using FDM 3D printing technology. The experimental results showed good agreement with simulations, confirming the validity of the design and optimization procedure. This approach demonstrated the potential of pixelation as a powerful tool for designing compact and efficient antennas with unconventional yet effective solutions. The LP pixelated SIW horn antenna and the CP pixelated SIW horn antenna with binary pixelated load were published in the journal paper [JZ64]. The improved design of the CP horn antenna with multistate pixelated load was presented in the conference paper [JZ72].

Objective 3: Automated Design Procedure for Waveguide Microwave Filters Based on Pixelation Strategy

An automated design procedure for waveguide microwave filters based on the pixelation strategy was proposed. This method does not rely on predefined templates

or filter order and autonomously determines the number of poles required to meet the desired filter response. The procedure was successfully applied to the design of two X-band waveguide filters. One was a multistate pixelated filter using metalized 3D-printed structures, while the other was an evanescent mode filter that avoided the challenges of metalization of the pixelated part by using a dielectric insert. While the evanescent mode filter exhibited relatively high passband losses due to dielectric material properties, the overall approach opens new possibilities for the automated design of complex waveguide filters. The pixelated multistate filter was published in the journal letter [JZ78] and the paper with the evanescent mode filter is submitted [JZ79].

Overall Conclusion

The methods and procedures presented in this dissertation contribute to the field of microwave engineering. The development of an efficient optimization algorithm and automated design strategies for pixelated structures enables the creation of highly optimized antennas and filters with minimal human intervention. The results of this work pave the way for further exploration and refinement of pixelated designs with the potential for widespread adoption in future microwave and antenna technologies.

Bibliography

[1] A. Ghadimi, V. Nayyeri, P. Salimi, M. Khanjarian, M. Soleimani, and O. M. Ramahi, "A pixelated resonator for mutual coupling reduction", in *2020 IEEE International Symposium on Antennas and Propagation and North American Radio Science Meeting*, IEEE, 2020, pp. 1925–1926.

[2] J. Lee, W. Jia, B. Sensale-Rodriguez, and J. S. Walling, "Pixelated rf: Random metasurface based electromagnetic filters", in *2023 21st IEEE Interregional NEWCAS Conference (NEWCAS)*, IEEE, 2023, pp. 1–5.

[3] S. Trinh-Van, Y. Yang, K.-Y. Lee, and K. C. Hwang, "A wideband circularly polarized pixelated dielectric resonator antenna", *Sensors*, vol. 16, no. 9, p. 1349, 2016.

[4] V. Gjokaj, J. Doroshewitz, J. Nanzer, and P. Chahal, "A design study of 5g antennas optimized using genetic algorithms", in *2017 IEEE 67th Electronic Components and Technology Conference (ECTC)*, IEEE, 2017, pp. 2086–2091.

[5] Y.-S. Chen, W.-H. Chou, and S.-Y. Chen, "Applications of optimization techniques to designs of ultra-wideband planar monopole antennas", in *2012 Asia Pacific Microwave Conference Proceedings*, IEEE, 2012, pp. 714–716.

[6] Y.-H. Chiu and Y.-S. Chen, "Multi-objective optimization for uwb antennas in impedance matching, gain, and fidelity factor", in *2015 IEEE International Symposium on Antennas and Propagation & USNC/URSI National Radio Science Meeting*, IEEE, 2015, pp. 1940–1941.

[7] R. O. Ouedraogo, E. J. Rothwell, A. Diaz, S.-Y. Chen, A. Temme, and K. Fuchi, "In situ optimization of metamaterial-inspired loop antennas", *IEEE Antennas and Wireless Propagation Letters*, vol. 9, pp. 75–78, 2010.

[8] D. Mair, M. Unterladstaetter, M. Renzler, and T. Ussmueller, "Evolutionary optimized pixelated antennas for 5g iot communication", in *2022 52nd European Microwave Conference (EuMC)*, IEEE, 2022, pp. 548–551.

[9] R. O. Ouedraogo, E. J. Rothwell, A. R. Diaz, K. Fuchi, and J. Tang, "Waveguide band-stop filter design using optimized pixelated inserts", *Microwave and optical technology letters*, vol. 55, no. 1, pp. 141–143, 2013.

[10] G. Liu, H. Zhang, and Z. Li, "Pixelated microwave sensor for angular displacement detection", in *2021 13th International Symposium on Antennas, Propagation and EM Theory (ISAPE)*, IEEE, 2021, pp. 1–3.

[11] D. G. Lee, T. Jeong, and K. C. Hwang, "Design of a wide-beamwidth pixelated dielectric resonator antenna using a modified stepped-impedance filter to suppress harmonics", *Applied Sciences*, vol. 12, no. 15, p. 7765, 2022.

[12] Y.-S. Chen and Y.-H. Chiu, "A parametric study of genetic algorithms for pixelated antenna design", in *2015 Asia-Pacific Symposium on Electromagnetic Compatibility (APEMC)*, IEEE, 2015, pp. 196–199.

[13] Y.-S. Chen, Y.-C. Chan, H.-J. Li, and S.-Y. Chen, "General rules for objective functions in wide-and multi-band pixelized antenna design", in *Proceedings of the 2012 IEEE International Symposium on Antennas and Propagation*, IEEE, 2012, pp. 1–2.

[14] Y.-S. Chen and T.-Y. Ku, "Pixelated design for multiple antennas in mimo handset applications", in *2015 Asia-Pacific Symposium on Electromagnetic Compatibility (APEMC)*, IEEE, 2015, pp. 192–195.

[15] M. Soltani, Y. Azizi, M. Soleimani, and L. Matekovits, "Design of high-gain lens antenna using pixelated phase gradient metasurface", in *2022 International Conference on Electromagnetics in Advanced Applications (ICEAA)*, IEEE, 2022, pp. 052–055.

[16] Y. Li, J. Dong, S. Wang, *et al.*, "An automated approach for pixelated antenna topology design incorporating multi-objective optimization algorithms", in *2019 International Conference on Microwave and Millimeter Wave Technology (ICMMT)*, IEEE, 2019, pp. 1–3.

[17] J. P. Jacobs, "Accurate modeling by convolutional neural-network regression of resonant frequencies of dual-band pixelated microstrip antenna", *IEEE Antennas and Wireless Propagation Letters*, vol. 20, no. 12, pp. 2417–2421, 2021.

[18] Z. Liu, E. A. Karahan, and K. Sengupta, "Deep learning-enabled inverse design of 30–94 ghz p sat, 3db sige pa supporting concurrent multiband operation at multi-gb/s", *IEEE Microwave and Wireless Components Letters*, vol. 32, no. 6, pp. 724–727, 2022.

[19] H. Wang, D.-G. Fang, B. Zhang, and W.-Q. Che, "Dielectric loaded substrate integrated waveguide (siw) h-plane horn antennas", *IEEE Transactions on Antennas and Propagation*, vol. 58, no. 3, pp. 640–647, 2009.

[20] B. Hu, T. Wu, Y. Cai, W. Zhang, and B.-L. Zhang, "A novel metamaterial-based planar integrated luneburg lens antenna with wide bandwidth and high gain", *IEEE Access*, vol. 8, pp. 4708–4713, 2019.

[21] M. Esquius-Morote, B. Fuchs, J.-F. Zürcher, and J. R. Mosig, "Novel thin and compact h-plane siw horn antenna", *IEEE Transactions on Antennas and Propagation*, vol. 61, no. 6, pp. 2911–2920, 2013.

[22] Y. Chen, L. Zhang, Y. He, *et al.*, "Broadband high-gain siw horn antenna loaded with tapered multistrip transition and dielectric slab for mm-wave application", *IEEE Transactions on Antennas and Propagation*, vol. 70, no. 7, pp. 5947–5952, 2022.

[23] Y. Zhang, J.-Y. Deng, D. Sun, J.-Y. Yin, and L.-X. Guo, "Compact slow-wave siw h-plane horn antenna with increased gain for vehicular millimeter wave communication", *IEEE Transactions on Vehicular Technology*, vol. 70, no. 7, pp. 7289–7293, 2021.

[24] L. Gong, Y. Fu, K. Y. Chan, J. A. Nanzer, and R. Ramer, "An siw horn antenna fed by a coupled mode emulating pyramidal horn antennas", *IEEE Transactions on Antennas and Propagation*, vol. 68, no. 1, pp. 33–42, 2019.

[25] S. Choudhury, A. Mohan, P. K. Mishra, and D. Guha, "Wideband pyramidal ridged horn design by siw technology", *IEEE Antennas and Wireless Propagation Letters*, vol. 18, no. 7, pp. 1517–1521, 2019.

[26] S. Moscato, R. Bahr, T. Le, *et al.*, "Additive manufacturing of 3d substrate integrated waveguide components", *Electronics Letters*, vol. 51, no. 18, pp. 1426–1428, 2015.

[27] C. Tomassoni, R. Bahr, M. Tentzeris, M. Bozzi, and L. Perregrini, "3d printed substrate integrated waveguide filters with locally controlled dielectric permittivity", in *2016 46th European Microwave Conference (EuMC)*, IEEE, 2016, pp. 253–256.

[28] Y. Kim and S. Lim, "Low loss substrate-integrated waveguide using 3d-printed non-uniform honeycomb-shaped material", *IEEE Access*, vol. 8, pp. 191 090–191 099, 2020.

[29] G. M. Rocco, M. Bozzi, S. Marconi, G. Alaimo, F. Auricchio, and D. Schreurs, "3d-printed microfluidic sensor in substrate integrated waveguide technology", in *2018 IEEE MTT-S International Microwave Workshop Series on Advanced Materials and Processes for RF and THz Applications (IMWS-AMP)*, IEEE, 2018, pp. 1–3.

[30] A. H. Allah, G. A. Eyebe, and F. Domingue, "Fully 3d-printed microfluidic sensor using substrate integrated waveguide technology for liquid permittivity characterization", *IEEE Sensors Journal*, vol. 22, no. 11, pp. 10 541–10 550, 2022.

[31] M. R. Naeini and D. van der Weide, "3d-printed high-directivity h-plane horn antenna with high front-to-back ratio using soft and hard walls", in *2021 IEEE Radio and Wireless Symposium (RWS)*, IEEE, 2021, pp. 1–3.

[32] D. S. Vorunichev, "Application of additive technology for 3d printing of electronic devices as a way to reduce prototyping time", in *2021 International Conference on Quality Management, Transport and Information Security, Information Technologies (ITQMIS)*, 2021, pp. 480–483. DOI: 10.1109/ITQMIS53292.2021.9642806.

[33] D. M. Pozar, *Microwave engineering.* John wiley & sons, 2011.

[34] Y. Yu, Z. Zhang, Q. S. Cheng, *et al.*, "State-of-the-art: Ai-assisted surrogate modeling and optimization for microwave filters", *IEEE Transactions on Microwave Theory and Techniques*, vol. 70, no. 11, pp. 4635–4651, 2022.

[35] M. Baranowski, Ł. Balewski, A. Lamecki, and M. Mrozowski, "Fast design optimization of waveguide filters applying shape deformation techniques", in *2022 24th International Microwave and Radar Conference (MIKON)*, IEEE, 2022, pp. 1–4.

[36] N. Aage and V. Egede Johansen, "Topology optimization of microwave waveguide filters", *International Journal for Numerical Methods in Engineering*, vol. 112, no. 3, pp. 283–300, 2017.

[37] D. G. Nielsen, S. D. Pedersen, V. Zhurbenko, V. E. Johansen, O. Sigmund, and N. Aage, "Topology optimization and experimental verification of compact e-plane waveguide filters", *Microwave and Optical Technology Letters*, vol. 61, no. 5, pp. 1208–1215, 2019.

[38] P. Vaitukaitis, K. Nai, J. Rao, and J. Hong, "On the development of metal 3d printed bandpass filter with wide stopband based on deformed elliptical cavity resonator with an additional plate", eng, *IEEE access*, vol. 10, pp. 15 427–15 435, 2022, ISSN: 2169-3536.

[39] Y. Zhang, J. Xu, F. Zhang, *et al.*, "A 3-d printed ka-band twisted waveguide filter with filtering and polarization rotation", in *2019 IEEE International Symposium on Antennas and Propagation and USNC-URSI Radio Science Meeting*, 2019, pp. 1701–1702, ISBN: 1728106923.

[40] Y. Zhang, F. Zhang, Y. Gao, J. Xu, C. Guo, and X. Shang, "3d printed waveguide step-twist with bandpass filtering functionality", eng, *Electronics letters*, vol. 56, no. 11, pp. 527–528, 2020, ISSN: 0013-5194.

[41] C. Bartlett, D. Miek, F. Kamrath, D. Bruhn, and M. Höft, "X-band 3d-printed metal-insert twist-component for bandpass filter applications", in *2021 IEEE MTT-S International Microwave Filter Workshop (IMFW)*, 2021, pp. 329–331. DOI: `10.1109/IMFW49589.2021.9642300`.

[42] X. Shang, P. Penchev, C. Guo, *et al.*, "*W* -band waveguide filters fabricated by laser micromachining and 3-d printing", *IEEE Transactions on Microwave Theory and Techniques*, vol. 64, no. 8, pp. 2572–2580, 2016. DOI: `10.1109/TMTT.2016.2574839`.

[43] C. Guo, X. Shang, M. J. Lancaster, and J. Xu, "A 3-d printed lightweight x-band waveguide filter based on spherical resonators", eng, *IEEE microwave and wireless components letters*, vol. 25, no. 7, pp. 442–444, 2015, ISSN: 1531-1309.

[44] R. Dahle, P. Laforge, and J. Kuhling, "3-d printed customizable inserts for waveguide filter design at x-band", *IEEE Microwave and Wireless Components Letters*, vol. 27, no. 12, pp. 1080–1082, 2017.

[45] D. Miek, F. Kamrath, P. Boe, and M. Höft, "Additive manufacturing of e-plane cut extracted pole waveguide filters with frequency-dependent coupling apertures", in *2020 IEEE Asia-Pacific Microwave Conference (APMC)*, 2020, pp. 522–524. DOI: `10.1109/APMC47863.2020.9331599`.

[46] D. Bruhn, D. Miek, K. Braasch, *et al.*, "Effects of cutting planes on filter performance of fdm 3d-printed x-band waveguide filters", in *2021 IEEE MTT-S International Microwave Filter Workshop (IMFW)*, 2021, pp. 236–238. DOI: `10.1109/IMFW49589.2021.9642301`.

[47] M. W. Elsallal, J. Hood, I. McMichael, and T. Busbee, "3d printed material characterization for complex phased arrays and metamaterials", eng, *Microwave journal (International ed.)*, vol. 59, no. 10, pp. 20–34, 2016, ISSN: 0192-6225.

[48] J. M. Felício, C. A. Fernandes, and J. R. Costa, "Complex permittivity and anisotropy measurement of 3d-printed pla at microwaves and millimeter-waves", in *2016 22nd International Conference on Applied Electromagnetics and Communications (ICECOM)*, IEEE, 2016, pp. 1–6.

[49] E. Huber, M. Mirzaee, J. Bjorgaard, M. Hoyack, S. Noghanian, and I. Chang, "Dielectric property measurement of pla", in *2016 IEEE International Conference on Electro Information Technology (EIT)*, IEEE, 2016, pp. 0788–0792.

[50] N. Reyes, F. Casado, V. Tapia, C. Jarufe, R. Finger, and L. Bronfman, "Complex dielectric permittivity of engineering and 3d-printing polymers at q-band", *Journal of Infrared, Millimeter, and Terahertz Waves*, vol. 39, no. 11, pp. 1140–1147, 2018.

[51] B. K. Tehrani, R. A. Bahr, W. Su, B. S. Cook, and M. M. Tentzeris, "E-band characterization of 3d-printed dielectrics for fully-printed millimeter-wave wireless system packaging", in *2017 IEEE MTT-S International Microwave Symposium (IMS)*, IEEE, 2017, pp. 1756–1759.

[52] R. Bahr, T. Le, M. M. Tentzeris, *et al.*, "Rf characterization of 3d printed flexible materials-ninjaflex filaments", in *2015 European microwave conference (EuMC)*, IEEE, 2015, pp. 742–745.

[53] Y. Arbaoui, V. Laur, A. Maalouf, and P. Queffelec, "3d printing for microwave: Materials characterization and application in the field of absorbers", in *2015 IEEE MTT-S international microwave symposium*, IEEE, 2015, pp. 1–3.

[54] R. Kronberger and V. Wienstroer, "3d-printed fss using printing filaments with enclosed metal particles", in *2017 Progress in Electromagnetics Research Symposium-Fall (PIERS-FALL)*, IEEE, 2017, pp. 808–811.

[55] A. M. Nicolson and G. F. Ross, "Measurement of the intrinsic properties of materials by time-domain techniques", *IEEE Transactions on instrumentation and measurement*, vol. 19, no. 4, pp. 377–382, 1970.

[56] J. Baker-Jarvis, M. D. Janezic, J. H. Grosvenor Jr, and R. G. Geyer, "Transmission/reflection and short-circuit line methods for measuring permittivity and permeability", *Nasa Sti/recon Technical Report N*, vol. 93, p. 12 084, 1992.

[57] S. K. Patil, M. Koledintseva, R. W. Schwartz, and W. Huebner, "Prediction of effective permittivity of diphasic dielectrics using an equivalent capacitance model", *Journal of Applied Physics*, vol. 104, no. 7, p. 074 108, 2008.

[58] ColorFabb, *Copperfill*, https://colorfabb.com/copperfill, Accessed: 2024-10-09, 2024.

[59] ColorFabb, *Steelfill*, https://colorfabb.com/steelfill, Accessed: 2024-10-09, 2024.

[60] *Colorfabb; co-polyester filaments; xt-black*, https://colorfabb.com/xt-black, Accessed: August 24, 2024.

[62] J. Baker-Jarvis, E. J. Vanzura, and W. A. Kissick, "Improved technique for determining complex permittivity with the transmission/reflection method", *IEEE Transactions on microwave theory and techniques*, vol. 38, no. 8, pp. 1096–1103, 1990.

[63] E. Massoni, M. Guareschi, M. Bozzi, *et al.*, "3d printing and metalization methodology for high dielectric resonator waveguide microwave filters", in *2017 IEEE MTT-S International Microwave Workshop Series on Advanced Materials and Processes for RF and THz Applications (IMWS-AMP)*, IEEE, 2017, pp. 1–3.

[65] J. Johnson and V. Rahmat-Samii, "Genetic algorithms in engineering electromagnetics", *IEEE Antennas and Propagation Magazine*, vol. 39, no. 4, pp. 7–21, 1997. DOI: 10.1109/74.632992.

[66] S. Mirjalili, S. M. Mirjalili, and X.-S. Yang, "Binary bat algorithm", *Neural Computing and Applications*, vol. 25, no. 3, pp. 663–681, 2014.

[67] S. Mirjalili and A. Lewis, "S-shaped versus v-shaped transfer functions for binary particle swarm optimization", *Swarm and Evolutionary Computation*, vol. 9, pp. 1–14, 2013.

[68] N. Hansen and S. Kern, "Evaluating the cma evolution strategy on multimodal test functions", in *International Conference on Parallel Problem Solving from Nature*, Springer, 2004, pp. 282–291.

[69] M. M. Mafarja, D. Eleyan, I. Jaber, A. Hammouri, and S. Mirjalili, "Binary dragonfly algorithm for feature selection", in *2017 International conference on new trends in computing sciences (ICTCS)*, IEEE, 2017, pp. 12–17.

[70] S. Mirjalili, S. M. Mirjalili, and A. Hatamlou, "Multi-verse optimizer: A nature-inspired algorithm for global optimization", *Neural Computing and Applications*, vol. 27, no. 2, pp. 495–513, 2016.

[71] C. Vanaret, J.-B. Gotteland, N. Durand, and J.-M. Alliot, *Certified global minima for a benchmark of difficult optimization problems (2014)*, 2014.

[73] C. A. Balanis, *Antenna theory : analysis and design*, eng, 3rd ed. Hoboken: Wiley-Interscience, 2005, ISBN: 978-0-471-66782-7.

[74] R. Kazemi and R. Safamanzar, "A single layer siw h-plane horn antenna with nearly equal e-and h-plane beamwidths", *Electromagnetics*, vol. 40, no. 6, pp. 409–423, 2020.

[75] S. Huang, K. Y. Chan, and R. Ramer, "Dielectric-loaded siw h-plane horn antenna with gradient air slots", *IEEE Antennas and Wireless Propagation Letters*, vol. 20, no. 1, pp. 43–47, 2020.

[76] L. Gong, Y. Fu, K. Y. Chan, J. A. Nanzer, and R. Ramer, "An siw horn antenna fed by a coupled mode emulating pyramidal horn antennas", *IEEE Transactions on Antennas and Propagation*, vol. 68, no. 1, pp. 33–42, 2019.

[77] M. Farashahi, E. Zareian-Jahromi, and R. Basiri, "A compact wideband circularly polarized siw horn antenna for k band applications", *AEU-International Journal of Electronics and Communications*, vol. 99, pp. 376–383, 2019.

[80] R. Dahle, P. Laforge, and J. Kuhling, "3-d printed customizable inserts for waveguide filter design at x-band", eng, *IEEE microwave and wireless components letters*, vol. 27, no. 12, pp. 1080–1082, 2017, ISSN: 1531-1309.

[81] C. Guo, X. Shang, M. J. Lancaster, and J. Xu, "A 3-d printed lightweight x-band waveguide filter based on spherical resonators", eng, *IEEE microwave and wireless components letters*, vol. 25, no. 7, pp. 442–444, 2015, ISSN: 1531-1309.

[82] F. Cai, W. T. Khan, and J. Papapolymerou, "A low loss x-band filter using 3-d polyjet technology", 2015 IEEE MTT-S International Microwave Symposium, 2015, pp. 1–4. DOI: 10.1109/MWSYM.2015.7166895.

[83] A. Pons, J. García, F. Quesada, *et al.*, "Evanescent mode filters composed of dielectric parts built using 3d-printing methods", in *2021 IEEE MTT-S International Microwave Filter Workshop (IMFW)*, IEEE, 2021, pp. 14–16.

[84] J. Li, C. Guo, L. Mao, J. Xiang, G.-L. Huang, and T. Yuan, "Monolithically 3-d printed hemispherical resonator waveguide filters with improved out-of-band rejections", *IEEE Access*, vol. 6, pp. 57030–57048, 2018. DOI: 10.1109/ACCESS.2018.2872696.

Author's Bibliography

[JZ61]   J. Zechmeister and J. Lacik, "Complex relative permittivity measurement of selected 3d-printed materials up to 10 ghz", in *2019 Conference on microwave techniques (COMITE)*, IEEE, 2019, pp. 1–4.

[JZ64]   J. Zechmeister, J. Lacik, and P. Kadlec, "The design of pixelated siw horn antennas with nearly equal beamwidths using binary ink stamp optimization", *IEEE Access*, vol. 9, pp. 122 216–122 227, 2021. DOI: 10.1109/ACCESS.2021.3109522.

[JZ72]   J. Zechmeister and J. Lacik, "Pixelated circularly polarized siw horn antenna with nearly equal beamwidths in principal planes", in *2022 24th International Microwave and Radar Conference (MIKON)*, 2022, pp. 1–4. DOI: 10.23919/MIKON54314.2022.9924837.

[JZ78]   J. Zechmeister and J. Lacik, "Automatic design procedure of waveguide filters based on a pixelization strategy", *IEEE Microwave and Wireless Technology Letters*, vol. 33, no. 10, pp. 1423–1425, 2023. DOI: 10.1109/LMWT.2023.3297514.

[JZ79]   J. Zechmeister and J. Lacik, "3d printed x-band evanescent mode waveguide filter based on pixelization strategy", *Microwave and Optical Technology Letters*, 2024, Submitted.

[JZ85]   J. Zechmeister, "A high directivity low profile lens antenna for a 77 ghz car radar", in *Proceedings of IEEE Student Branch Conference Blansko 2018*, 2018, pp. 40–43, ISBN: 978-80-214-5661-7.

[JZ86]   J. Zechmeister, "3d-printed lens for high directional low-profile antenna", in *Proceedings of the 25th Conference STUDENT EEICT 2019*, 2019, pp. 484–488, ISBN: 978-80-214-5735-5.

[JZ87]   J. Zechmeister, "Measurement of electrically small antennas", in *Proceedings of the 26th Conference STUDENT EEICT 2020*, 2020, pp. 1–7, ISBN: 978-80-214-5867-3.

List of Figures

List of Tables

List of abbreviations

ABS Acrylonitrile Butadiene Styrene
AI Artificial Intelligence
AR Axial Ratio
BCMAES Binary Covariance Matrix Adaptation Evolution Strategy
BBA Binary Bat Algorithm
BDA Binary Dragonfly Algorithm
BPSO Binary Particle Swarm Optimization
BISO Binary Ink Stamp Optimization
BW Bandwidth
CP Circularly Polarized
CNN Convolutional Neural Network
DBS Direct Binary Search
DRA Dielectric Resonator Antenna
EBG Electromagnetic Band-Gap
FDM Fused Deposition Modeling
GA Genetic Algorithm
HPBW Half Power Beam Width
IoT Internet of Things
ISM Industrial, Scientific, and Medical
LP Linearly Polarized
LSB Least Significant Bit
MOBPSO Multi-Objective Binary Particle Swarm Optimization
MUT Material Under Test
MVO Multi-Verse Optimization
MSB Most Significant Bit
NRW Nicholson-Ross-Weir
PCB Printed Circuit Board
PHA Polyhydroxyalkanoate
PET Polyethylene Terephthalate
PLA Polylactic Acid
RHCP Right-Handed Circularly Polarized
SIW Substrate Integrated Waveguide
SLA Stereolithography
SLM Selective Laser Melting
SLL Side Lobes Level
TR Transmission-Reflection
TRL Through-Reflect-Line
UV Ultraviolet
VNA Vector Network Analyzer

Appendix – Benchmark Function Results

This appendix contains the results of testing the proposed BISO algorithm on 15 benchmark functions and a comparison with several other optimization algorithms, namely BPSO, GA, BCMAES, BBA, BDA, and MVO. The list of benchmark functions used for evaluation is provided in Table 4.2. The results are presented in the form of average values and standard deviations over 100 independent runs. The data are organized into four tables corresponding to different dimensionalities of the benchmark functions: 30, 120, 300, and 900. This layout allows for a comprehensive evaluation of the performance and robustness of each algorithm across various problem sizes.

$Ndim = 30$	BISO	BPSO	GA	BCMAES	BBA	BDA	MVO
f_1	**0**	**0**	**0**	1.31	**0**	**0**	5.20E-01
	(0)	**(0)**	**(0)**	(2.96)	**(0)**	**(0)**	(7.03E-01)
f_2	**0**	**0**	**0**	1.94	**0**	**0**	6.12E-03
	(0)	**(0)**	**(0)**	(2.63)	**(0)**	**(0)**	(1.43E-02)
f_3	**0**	1.23E-05	**0**	5.84E+02	**0**	4.10E-06	6.38E-02
	(0)	(1.19E-04)	**(0)**	(1.01E+03)	**(0)**	(3.04E-05)	(3.20E-01)
f_4	**0**	6.71E-04	**0**	1.32E+01	**0**	3.66E-04	7.61E-02
	(0)	(5.05E-03)	**(0)**	(1.69E+01)	**(0)**	(1.46E-03)	(1.39E-01)
f_5	**3.51E-03**	1.80E-01	5.96E-01	1.63E+04	2.26	7.56E-02	3.90
	(4.92E-03)	(1.08)	(1.76)	(7.00E+04)	(4.75)	(2.74E-01)	(5.22)
f_6	**3.01E-06**	4.23E-04	3.01E-04	2.20E+02	6.70E-05	2.98E-04	2.23E-02
	(8.43E-06)	(1.86E-03)	(1.87E-03)	(3.86E+02)	(1.58E-04)	(1.33E-03)	(4.03E-02)
f_7	**0**	**0**	**0**	1.68E-02	**0**	**0**	3.83E-11
	(0)	**(0)**	**(0)**	(4.76E-02)	**(0)**	**(0)**	(1.93E-10)
f_8	**-8.38E+02**	**-8.38E+02**	-8.37E+02	-6.49E+02	**-8.38E+02**	**-8.38E+02**	-8.25E+02
	(6.85E-03)	**(8.35E-02)**	(1.18E+01)	(1.50E+02)	**(7.87E-02)**	**(7.39E-02)**	(3.30E+01)
f_9	5.89E-03	3.92E-02	1.59E-01	7	2.85E-01	0	7.46E-01
	(3.98E-02)	(2.13E-01)	(3.93E-01)	(6.08)	(6.77E-01)	(0)	(8.32E-01)
f_{10}	**8.88E-16**	**8.88E-16**	5.16E-02	2.86	**8.88E-16**	**8.88E-16**	1.93E-01
	(0)	**(0)**	(3.63E-01)	(3.92)	**(0)**	**(0)**	(5.66E-01)
f_{11}	**3.34E-03**	1.08E-02	1.40E-02	2.87	1.37E-02	1.47E-02	6.48E-02
	(3.77E-03)	(9.33E-03)	(1.31E-02)	(4.88)	(9.53E-03)	(1.15E-02)	(8.01E-02)
f_{12}	**-1.8**	-1.8	-1.8	-1.29	-1.8	-1.8	-1.79
	(6.19E-08)	(1.35E-04)	(1.86E-04)	(4.84E-01)	(3.25E-02)	(1.35E-04)	(4.58E-02)
f_{13}	-9.33E-01	-9.80E-01	-8.80E-01	-3.87E-02	-6.70E-01	**-1**	-7.35E-01
	(6.05E-02)	(1.41E-01)	(3.27E-01)	(2.41E-01)	(4.73E-01)	**(0)**	(4.38E-01)
f_{b1}	7.45E-02	**5.93E-02**	7.87E-02	2.34	4.38E-01	2.07E-01	9.58E-01
	(6.34E-03)	**(3.31E-02)**	(2.45E-02)	(2.04)	(5.39E-01)	(3.04E-01)	(6.20E-01)
f_{b2}	**0**	**0**	**0**	1.05E+03	**0**	**0**	3.21E+01
	(0)	**(0)**	**(0)**	(1.05E+03)	**(0)**	**(0)**	(5.66E+01)

Tab. 1: Results for benchmark functions for $Ndim = 30$.

$Ndim = 120$	BISO	BPSO	GA	BCMAES	BBA	BDA	MVO
f_1	**0**	4.21	**0**	5.70E-01	7.70E-01	3.42	1.53E+01
	(0)	(1.49)	**(0)**	(5.7)	(7.50E-01)	(1.69)	(2.91)
f_2	**0**	1.12E-01	**0**	2.14E+03	5.74E-04	7.83E-02	1.87
	(0)	(6.70E-02)	**(0)**	(1.02E+04)	(7.35E-04)	(7.39E-02)	(9.15E-01)
f_3	1.01E+01	4.42E+01	3.61E+02	9.28E+03	**2.51**	7.10E+01	9.46E+02
	(1.64E+01)	(6.33E+01)	(3.87E+02)	(6.61E+03)	**(8.77)**	(1.11E+02)	(7.24E+02)
f_4	**1.46E-03**	2.17	2.29E-02	4.55E+01	9.11E-02	1.1	1.47E+01
	(3.02E-03)	(1.34)	(2.81E-02)	(2.43E+01)	(4.05E-02)	(1.03)	(6.88)
f_5	**1.10E+01**	1.46E+02	5.35E+01	3.88E+06	3.38E+01	7.11E+01	1.06E+04
	(1.79E+01)	(1.76E+02)	(9.71E+01)	(6.45E+06)	(5.01E+01)	(9.84E+01)	(3.23E+04)
f_6	**3.27E-02**	1.22	7.57E-02	2.62E+03	3.58E-02	5.02E-01	1.57E+02
	(2.07E-02)	(1.54)	(7.74E-02)	(3.05E+03)	(3.91E-02)	(1.04)	(1.70E+02)
f_7	**8.12E-17**	6.29E-07	0	1.35	3.39E-15	1.03E-06	5.09E-03
	(1.86E-16)	(2.26E-06)	(0)	(2.78)	(1.07E-14)	(8.32E-06)	(1.91E-02)
f_8	-3.26E+03	-3.11E+03	-3.17E+03	-2.24E+03	**-3.33E+03**	-3.14E+03	-2.74E+03
	(6.79E+01)	(1.26E+02)	(1.18E+02)	(5.23E+02)	**(4.38E+01)**	(1.50E+02)	(2.41E+02)
f_9	**3.34**	8.5	5.78	4.28E+01	4.42	9.15	2.19E+01
	(1.14)	(5.01)	(2.92)	(2.03E+01)	(3.73)	(4.19)	(8.79)
f_{10}	**2.79E-05**	1.53	5.69E-01	2.92	3.15E-02	6.60E-01	5.95
	(2.79E-04)	(8.31E-01)	(1)	(4.75)	(1.85E-01)	(6.85E-01)	(2)
f_{11}	**1.38E-02**	5.21E-01	2.32E-01	2.39E+01	1.05E-01	2.67E-01	2.07
	(2.17E-02)	(2.04E-01)	(1.57E-01)	(2.77E+01)	(7.26E-02)	(1.23E-01)	(1.42)
f_{12}	**-7.34**	-7.05	-7.34	-4.98	-7.2	-7.09	-6.34
	(1.32E-01)	(3.06E-01)	(2.00E-01)	(1.44)	(2.00E-01)	(3.15E-01)	(5.70E-01)
f_{13}	**1.69E-05**	1.41E-04	2.72E-05	1.39E-02	6.32E-05	6.13E-05	4.79E-04
	(5.08E-05)	(1.70E-04)	(6.30E-05)	(1.88E-02)	(1.57E-04)	(1.09E-04)	(2.99E-04)
f_{b1}	1.45E+01	1.51E+01	2.73E+01	8.76E+01	**4.98**	1.48E+01	9.14E+01
	(1.18E+01)	(1.19E+01)	(1.85E+01)	(3.23E+01)	**(7.53)**	(1.03E+01)	(2.34E+01)
f_{b2}	1.81	5.69E+03	**0**	6.48E+04	9.52E+01	5.19E+03	4.42E+04
	(4.02)	(3.13E+03)	**(0)**	(5.41E+04)	(1.32E+02)	(3.66E+03)	(1.19E+04)

Tab. 2: Results for benchmark functions for $Ndim = 120$.

$Ndim = 300$	BISO	BPSO	GA	BCMAES	BBA	BDA	MVO
f_1	5.10E-01	4.42E+01	**0**	8.71	3.93E+01	3.47E+01	6.67E+01
	(5.02E-01)	(4.05)	**(0)**	(1.12E+01)	(3.06)	(4.26)	(5.15)
f_2	1.02E-01	4.21	**3.24E-03**	1.29E+10	1.2	2.94	2.27E+01
	(1.85E-02)	(1.19)	**(2.58E-03)**	(6.77E+10)	(2.62E-01)	(1.08)	(7.73)
f_3	2.59E+03	6.63E+03	6.88E+03	4.07E+04	**2.44E+03**	4.87E+03	1.41E+04
	(1.42E+03)	(2.52E+03)	(2.29E+03)	(2.70E+04)	**(1.30E+03)**	(2.23E+03)	(4.75E+03)
f_4	**9.16E-01**	2.02E+01	7.61	7.76E+01	6.15	1.90E+01	4.90E+01
	(1.92E-01)	(4.64)	(3.93)	(1.54E+01)	(1.02)	(6.27)	(8.22)
f_5	**9.11E+01**	4.85E+04	2.00E+02	1.14E+07	6.56E+02	1.90E+04	2.91E+06
	(6.44E+01)	(6.68E+04)	(2.34E+02)	(1.82E+07)	(4.47E+02)	(3.31E+04)	(3.25E+06)
f_6	7.10E-01	3.23E+02	**2.78E-01**	4.32E+03	1.65E+01	1.90E+02	3.51E+03
	(1.73E-01)	(1.49E+02)	**(1.10E-01)**	(5.03E+03)	(6.93)	(1.25E+02)	(1.59E+03)
f_7	9.22E-08	1.22E-02	**2.43E-10**	5.76	2.15E-05	7.49E-03	9.66E-01
	(4.79E-08)	(1.11E-02)	**(4.64E-10)**	(8.01)	(1.72E-05)	(1.50E-02)	(7.72E-01)
f_8	**-7.66E+03**	-6.21E+03	-7.32E+03	-5.37E+03	-7.14E+03	-6.65E+03	-5.39E+03
	(2.41E+02)	(4.19E+02)	(3.33E+02)	(9.72E+02)	(3.23E+02)	(3.77E+02)	(4.82E+02)
f_9	**1.60E+01**	6.66E+01	3.54E+01	1.13E+02	4.27E+01	5.30E+01	1.01E+02
	(4.57)	(1.52E+01)	(1.19E+01)	(4.26E+01)	(9.12)	(1.46E+01)	(1.86E+01)
f_{10}	**2.08E-01**	6.11	1.53	1.03E+01	2.68	4.83	1.27E+01
	(4.39E-02)	(9.46E-01)	(1.01)	(7.17)	(3.62E-01)	(1.13)	(1.68)
f_{11}	8.06E-01	3.90	**8.72E-02**	4.76E+01	1.14	2.85	3.45E+01
	(9.33E-02)	(1.52)	**(1.14E-01)**	(4.17E+01)	(6.63E-02)	(1.33)	(1.49E+01)
f_{12}	**-1.76E+01**	-1.47E+01	-1.76E+01	-1.25E+01	-1.60E+01	-1.54E+01	-1.25E+01
	(4.55E-01)	(8.94E-01)	(5.61E-01)	(2.92)	(6.69E-01)	(9.55E-01)	(1.15)
f_{13}	8.54E-09	1.85E-08	**6.99E-09**	4.94E-04	9.81E-09	1.43E-08	5.60E-08
	(1.74E-09)	(6.71E-09)	**(2.23E-09)**	(1.13E-03)	(2.11E-09)	(5.69E-09)	(4.00E-08)
f_{b1}	1.11E+01	7.63	8.67	7.00E+01	2.93	**2.26**	1.30E+01
	(5.12)	(7.22)	(6.71)	(3.29E+01)	(2.95)	**(2.51)**	(5.04)
f_{b2}	1.71E+04	7.41E+05	**1.73E+02**	1.12E+06	5.24E+05	5.73E+05	1.51E+06
	(4.44E+03)	(9.77E+04)	**(2.88E+02)**	(7.77E+05)	(5.83E+04)	(1.24E+05)	(1.59E+05)

Tab. 3: Results for benchmark functions for $Ndim = 300$.

$Ndim = 900$	BISO	BPSO	GA	BCMAES	BBA	BDA	MVO
f_1	**2.41E+01**	2.51E+02	1.02E+02	3.75E+02	2.46E+02	2.27E+02	2.89E+02
	(1.83)	(8.95)	(6.25)	(1.22E+01)	(6.26)	(8.92)	(1.04E+01)
f_2	**6.91**	7.66E+01	7.03	2.07E+34	5.31E+01	5.77E+01	1.46E+02
	(5.39E-01)	(9.82)	(1.42)	(1.89E+35)	(4.81)	(9.87)	(1.85E+01)
f_3	**6.11E+04**	1.21E+05	6.54E+04	2.44E+05	6.93E+04	7.48E+04	1.25E+05
	(8.98E+03)	(1.97E+04)	(1.09E+04)	(1.39E+05)	(1.15E+04)	(1.39E+04)	(2.42E+04)
f_4	**2.45E+01**	6.58E+01	5.82E+01	9.40E+01	4.28E+01	5.91E+01	7.77E+01
	(2.28)	(4.03)	(5.13)	(6.15)	(2.81)	(4.81)	(4.72)
f_5	1.21E+05	1.72E+07	**4.44E+04**	9.71E+07	3.77E+06	1.12E+07	8.97E+07
	(2.45E+04)	(6.87E+06)	**(2.24E+04)**	(4.26E+07)	(1.11E+06)	(5.72E+06)	(2.86E+07)
f_6	6.17E+02	1.53E+04	**3.46E+02**	4.95E+04	8.35E+03	1.08E+04	4.08E+04
	(8.79E+01)	(2.33E+03)	**(9.87E+01)**	(1.54E+04)	(1.23E+03)	(2.48E+03)	(7.49E+03)
f_7	9.18E-02	1.53E+01	**3.02E-02**	1.01E+02	2.84	9.2	7.85E+01
	(2.06E-02)	(5)	**(1.63E-02)**	(5.59E+01)	(8.25E-01)	(5.27)	(2.50E+01)
f_8	**-2.13E+04**	-1.27E+04	-2.01E+04	-1.20E+04	-1.37E+04	-1.47E+04	-1.17E+04
	(5.59E+02)	(8.79E+02)	(7.23E+02)	(1.50E+03)	(7.39E+02)	(8.86E+02)	(9.88E+02)
f_9	**9.54E+01**	4.17E+02	1.88E+02	5.19E+02	4.03E+02	3.30E+02	4.92E+02
	(1.16E+01)	(4.10E+01)	(3.15E+01)	(6.32E+01)	(2.90E+01)	(4.11E+01)	(4.95E+01)
f_{10}	5.26	1.47E+01	**4.3**	2.02E+01	1.25E+01	1.31E+01	1.78E+01
	(2.36E-01)	(8.23E-01)	**(4.40E-01)**	(6.49E-01)	(5.70E-01)	(1.09)	(6.42E-01)
f_{11}	6.73	1.35E+02	**4.16**	4.79E+02	7.73E+01	9.74E+01	3.61E+02
	(6.98E-01)	(2.83E+01)	**(9.24E-01)**	(1.49E+02)	(1.19E+01)	(2.43E+01)	(6.38E+01)
f_{12}	-4.82E+01	-2.80E+01	**-4.93E+01**	-2.53E+01	-2.81E+01	-3.28E+01	-2.63E+01
	(9.13E-01)	(2.23)	**(1.35)**	(4.14)	(1.4)	(1.7)	(1.75)
f_{13}	**2.95E-25**	2.09E-22	8.42E-25	9.33E-11	3.21E-23	1.99E-23	1.54E-20
	3.13E-26	4.38E-22	6.94E-25	9.22E-10	3.69E-23	2.33E-23	4.89E-20
f_{b1}	2.68E+01	6.06E+01	5.78E+01	2.10E+02	1.59E+01	**9.55**	3.67E+01
	(4.59E+01)	(2.29E+01)	(6.85E+01)	(2.59E+01)	(1.65E+01)	**(2.3)**	(1.10E+01)
f_{b2}	**5.70E+06**	5.24E+07	1.36E+07	8.42E+07	5.00E+07	4.57E+07	6.73E+07
	(3.79E+05)	(2.46E+06)	(1.19E+06)	(7.79E+06)	(1.94E+06)	(3.01E+06)	(4.03E+06)

Tab. 4: Results for benchmark functions for $Ndim = 900$.

Curriculum Vitae

Jaroslav Zechmeister

Born 3.8.1993 in Hustopeče
Kobylí 288, 69110 Kobylí, Czech Republic
jaroslav.zechmeister@gmail.com | +420 602 242 673

Education

Doctoral Degree – Electronics and Communications Engineering
Brno University of Technology
09/2018–present
Dissertation: *3D Printed Microwave Structures*

Master's Degree – Electronics and Communications Engineering
Brno University of Technology
09/2016–06/2018
Master's Thesis: *Antenna System for Car Radar* (Dean's Award for Master's Thesis)

Bachelor's Degree – Electronics and Communications Engineering
Brno University of Technology
09/2013–06/2016
Bachelor's Thesis: *Circularly Polarized Dielectric Resonator Antenna*

Stays & Courses

TU Wien – Institute of Electrodynamics, Microwave and Circuit Engineering, Vienna, Austria
12/2019
Topic: *EM Characterization of Composite 3D-Printed Materials*

Université Côte d'Azur, Nice, France
European School of Antennas course
11/2019
Topic: *Antennas and Rectennas for IoT Applications*

Work Experience

HF Electronics Specialist
TechSoft Engineering spol. s.r.o., Prague
01/2023–present
High-frequency electronics simulations using Ansys tools, product support, technical sales support

Antenna Designer (Part-Time)
Senzoor Czech s.r.o., Brno
02/2018–12/2022
Design and measurement of antennas for IoT applications

Repair Technician (Part-Time)
Sanmina-SCI Czech Republic s.r.o., Brno
09/2017–12/2017
Diagnosis of communication unit faults, replacement of defective components, functionality testing

Skills

- Design of antennas and microwave structures
- Wireless and RF systems
- PCB power and signal integrity analysis
- EMC analysis
- PCB thermal management analysis
- Software: Ansys HFSS, Ansys SIwave, Ansys Icepak, CST MWS, MATLAB, Python, MS Office
- Languages: Czech (native), English (B2)